

QATAR UNIVERSITY

COLLEGE OF ARTS AND SCIENCES

THE USE OF NOVEL IONIC LIQUID AND CELLULOSE NANOCRYSTALS

MODIFIED DATE PITS AS ADSORBENTS FOR GROUNDWATER TREATMENT

BY

SARA MOHIDDIN ABDALLAH WAHIB

A Thesis Submitted to
the College of Arts and Sciences
in Partial Fulfillment of the Requirements for the Degree of
Masters of Science in Master of Science in Environmental Sciences

June 2021

© 2021. Sara Mohiddin Abdallah Wahib. All Rights Reserved.

COMMITTEE PAGE

The members of the Committee approve the Thesis of
Sara Mohiddin Abdallah Wahib defended on 25/04/2021.

Prof. Mohammad A. Alghouti
Thesis/Dissertation Supervisor

Prof. Nabil Zouari
Committee Member

Prof. Yousef Hijji
Committee Member

Approved:

Ibrahim AlKaabi, Dean, College of Arts and Sciences

ABSTRACT

WAHIB, SARA, M., Masters : June : Master of Science in Environmental Sciences

Title: The use of novel ionic liquid and cellulose nanocrystals modified date pits as adsorbents for groundwater treatment

Supervisor of Thesis: Mohammad A. Al-Ghouti .

This study aims to investigate the remediation of Li^{1+} , Mo^{6+} , and B^{3+} from groundwater using an innovative low-cost adsorbent. Agriculturally abundant date pits were modified to be successfully used as an adsorbent. Chemical modifications were performed to functionalize raw date pits (RDP) by using cellulose nanocrystals (CNC) and ionic liquid (IL), and the modified adsorbent are named IL-CNC@DP. Results demonstrated that the maximum adsorption capacity of all metals was at pH 6 and the highest uptake capacity order was $\text{Li}^{1+} > \text{B}^{3+} > \text{Mo}^{6+}$. Moreover, thermodynamics constants for all metals of the adsorption process showed that the modified adsorbent (IL-CNC@DP) was exothermic, does not favor a high level of disorder, and is spontaneous in nature. Langmuir, Freundlich, Dubinin–Radushkevich, and Temkin isotherm models were used to find the best-fit model for each metal. Lastly, the characterizations of the novel adsorbents were performed by scanning electron microscope (SEM), Transmission electron microscopy (TEM), Fourier-transform infrared spectroscopy (FTIR), and Brunauer-Emmett-Teller (BET) surface area analysis. In this current study, the modified adsorbent (IL-CNC@DP) in comparison to the unmodified adsorbent (RDP) confirmed exceptional results proving that the modification enhanced the remediation of the Li^{1+} , Mo^{6+} , and B^{3+} from water.

DEDICATION

This thesis is dedicated to my parents, who have been my main support system throughout this entire journey. To my siblings and friends, thank you for encouraging and pushing me to do my best. I also want to thank my soulmate for his advice and motivation. Lastly, this thesis is dedicated to the generations of women, who are passionate, ambitious, and driven by the world of science.

May we all find our passion in life.

ACKNOWLEDGMENTS

Many thanks to my supervisor Prof. Mohammad Al-Ghouti for his constant guidance and supervision that helped me complete my work. Also, special thanks to my committee members Prof. Nabil Zouari and Prof. Yousef Hijji for their valuable feedback. I would like to thank my colleagues and the new friends that I made throughout my study, especially Dana Adel and Rana Al- Absi. Also, many thanks to the CLU unit at Qatar University for their help in analyzing my samples, and many thanks to all the lab technicians in the Department of Biological and Environmental Sciences.

TABLE OF CONTENTS

DEDICATION.....	iv
ACKNOWLEDGMENTS	v
LIST OF TABLES	ix
LIST OF FIGURES.....	xi
Chapter 1: INTRODUCTION.....	1
1.1 Introduction	1
1.1.1 Research rationale	5
1.1.2 Research hypothesis.....	6
1.1.3 Research objectives.....	6
Chapter 2: LITERATURE REVIEW.....	8
2.1 Groundwater in Qatar.....	8
2.1.1 Metal Contamination in Qatar’s Groundwater.....	10
2.1.2 Physical and chemical properties of groundwater samples in Qatar.....	13
2.1.3 Causes of groundwater deterioration.....	15
2.2 Cellulose overview.....	17
2.2.1 Extraction of cellulose nanocrystals (CNC).....	19
2.3 The application of Ionic liquids (IL)	23
2.4 Adsorption mechanisms and its application in water treatment.....	28
Chapter 3: MATERIALS AND METHODOLOGY	33

3.1 Materials.....	33
3.2 Preparation of starting material.....	33
3.3 Extraction of cellulose from date pits	33
3.4 Method 1-Mechanical stirrer.....	34
3.5 Method 2- Soxhlet apparatus	35
3.6 Preparation of cellulose nanocrystals (CNCs).....	35
3.7 Characterization of the prepared CNC and Intermediate Products	36
3.7.1 Chemical composition measurement of the lignocellulosic materials of the raw date pits (RDP).....	36
3.7.2 Determination of physical properties of the isolated CNCs from method 1 & 2.....	36
3.7.3 Characterization adsorbents (IL-CNC@DP & RDP), CNC, & intermediate products.....	37
3.8 Preparation of ionic liquid-nanocellulose composite (IL-CNC).....	38
3.9 Functionalization of raw date pits (RDP) with the prepared IL-CNC.....	39
3.10 Preparation of Li^+ , Mo^{6+} , & B^{3+} stock solution.....	39
3.11 Batch adsorption of Li^+ , Mo^{6+} , & B^{3+}	39
3.12 Adsorption isotherms of Li^+ , Mo^{6+} , & B^{3+}	40
3.13 Thermodynamic studies of Li^+ , Mo^{6+} , & B^{3+} adsorption.....	42
3.14 Desorption studies of Li^+ , Mo^{6+} , & B^{3+}	42
3.15 Statistical analysis	43

3.16 Application of RDP and IL-CNC@RDP to a real groundwater sample	43
Chapter 4: RESULTS AND DISCUSSION	44
4.1 Characterization	44
4.1.1 Chemical Components	44
4.1.2 Physicochemical properties of CNC ₁ & CNC ₂	46
4.1.3 Scanning electron microscopy (SEM) analysis	47
4.1.4 Transmission electron microscopy (TEM) analysis	57
4.1.5 Fourier transform infrared (FTIR) analysis	59
4.1.6 X-ray powder diffraction (XRD) analysis	67
4.2 Mechanisms of adsorption onto IL-CNC@DP modified adsorbent	70
4.3 Effect of pH value on Li ¹⁺ , Mo ⁶⁺ , and B ⁺ ions adsorption	79
4.4 Effect of initial Li ¹⁺ , Mo ⁶⁺ , & B ³⁺ concentration on the adsorption process	91
4.5 Effect of temperature on adsorption of Li ¹⁺ , Mo ⁶⁺ , & B ⁺ and thermodynamics.	100
4.6 Adsorption isotherms of Li ¹⁺ & Mo ⁶⁺ removal onto IL-CNC@RDP and RDP	114
4.7 Desorption studies of Li ¹⁺ , Mo ⁶⁺ , & B ³⁺	135
4.8 Application of RDP and IL-CNC@RDP to a real groundwater sample	138
CHAPTER 5: CONCLUSION	142
References	144

LIST OF TABLES

Table 1. Summarizes the advantages and disadvantages treatment for low quality groundwater.	3
Table 2. Different types of adsorbents materials used for wastewater treatment.	5
Table 3. Summary of the physicochemical characteristics of the groundwater samples. Modified from Ahmad et al. (2020).	14
Table 4. Summary of some groundwater studies for lithium, molybdenum, and boron.	16
Table 5. Summarizes the commonly used ionic liquid of cations and anions.	26
Table 6. Isotherm models used in this study.	41
Table 7. Chemical composition of cellulose nanocrystals from different sources. *N ₁ DP & N ₂ DP (treated by NaOH), B ₁ DP & B ₂ DP (after bleaching).	44
Table 8. Physicochemical properties of isolated CNCs.	47
Table 9. Crystallinity value of cellulose nanocrystals (CNC) obtained from different	69
Table 10. Physicochemical characteristics of Li ¹⁺ , Mo ⁶⁺ , & B ³⁺ ions.	75
Table 11. Thermodynamic parameters for Li ¹⁺ adsorption onto IL-CNC@DP & RDP.	104
Table 12. Thermodynamic parameters for Mo ⁶⁺ adsorption onto IL-CNC@DP & RDP.	109
Table 13. Thermodynamic parameters for B ³⁺ adsorption onto IL-CNC@DP & RDP.	113

Table 14. The parameters of the two isotherms models for lithium adsorption onto IL-CNC@RDP and RDP at 25 °C, 35 °C, and 45 °C.....	118
Table 15. The parameters of the two isotherms models for molybdenum adsorption onto IL-CNC@RDP and RDP at 25 °C, 35 °C, and 45 °C.	125
Table 16. The parameters of the two isotherms models for boron adsorption onto IL-CNC@RDP and RDP at 25 °C, 35 °C, and 45 °C.....	132
Table 17. Effect of different eluant concentrations on Li ¹⁺ desorption efficiency (%) onto IL-CNC@DP and RDP.....	137
Table 18. Effect of different eluant concentrations on Mo ⁶⁺ desorption efficiency (%) onto IL-CNC@DP and RDP.....	137
Table 19. Effect of different eluant concentrations on B ³⁺ desorption efficiency (%) onto IL-CNC@DP and RDP.....	137

LIST OF FIGURES

Figure 1. Schematic illustration of acid hydrolysis process of the scission of glucosidic bonds (Jonoobi et al., 2015).	23
Figure 2. Demonstration of the adsorption mechanism between the adsorbent and adsorbate (Bushra et al., 2016).	29
Figure 3. Schematic illustration summarizing the used extraction methods for cellulose nanocrystals (CNC) from raw date pits (RDP).	34
Figure 4. A-J Schematic illustration of SEM surface morphology of A) RDP at 5000x, B) RDP at 2500x, C) N ₁ .DP, D) N ₂ .DP, E) B ₁ .DP, F) B ₂ .DP, G) CNC ₁ at 10,000x, H) CNC ₁ at 2500x, I) CNC ₂ at 10,000x, J) CNC ₂ at 2500x.	49
Figure 5. SEM images of the IL-CNC@DP before and after adsorption. (A) Before the treatment under 25 °C. (B) After Li ¹⁺ adsorption at 100 ppm with pH 6 under 45 °C. (C) After Mo ⁶⁺ adsorption at 100 ppm with pH 6 under 45 °C. (D) After B ³⁺ adsorption at 100 ppm with pH 6 under 45 °C.	54
Figure 6. SEM images of the RDP before and after adsorption. (A) Before the treatment under 25 °C. (B) After Li ¹⁺ adsorption at 100 ppm with pH 6 under 45 °C. (C) After Mo ⁶⁺ adsorption at 100 ppm with pH 6 under 45 °C. (D) After B ³⁺ adsorption at 100 ppm with pH 6 under 45 °C.	56
Figure 7. TEM image of A) CNC ₁ at high magnification, B) CNC ₁ at low magnification, C) CNC ₂ at high magnification, D) CNC ₂ at low magnification.	58
Figure 8. FTIR spectrum of CNC ₁ and CNC ₂	59
Figure 9. FTIR spectrum of the unmodified RDP and the modified IL-CNC@DP adsorbents.	61
Figure 10. FTIR spectra of the IL-CNC@DP and RDP before and after Li ¹⁺ , Mo ⁶⁺ , B ³⁺	

ions adsorption. (A) IL-CNC@DP and (B) RDP.....	64
Figure 11. XRD patterns of CNC ₁ and CNC ₂	69
Figure 12. Schematic representation of the formation of the modified IL-CNC@DP adsorbent.	76
Figure 13. Proposes the different mechanisms of adsorption onto the adsorbent by the pollutants through monodentate, bidentate, or polydentate ligands.	77
Figure 14. Schematic representation of the modified adsorbent IL-CNC@DP.....	77
Figure 15. Adsorption onto the surface of CNC and its pores, modified from Al-Ghouti et al. (2014).....	78
Figure 16. Percentage removal of Li ¹⁺ from solution by IL-CNC@DP & RDP at different pH values.	83
Figure 17. Percentage removal of Mo ⁶⁺ from solution by IL-CNC@DP & RDP at different pH values.	87
Figure 18. Percentage removal of B ³⁺ from solution by IL-CNC@DP & RDP at different pH values.	90
Figure 19. Effect of initial concentration on the IL-CNC@DP & RDP at different concentrations on Li ¹⁺ adsorption.....	94
Figure 20. Effect of initial concentration on the IL-CNC@DP & RDP at different concentrations on Mo ⁶⁺ adsorption.....	97
Figure 21. Effect of initial concentration on the IL-CNC@DP & RDP at different concentrations on B ³⁺ adsorption.	99
Figure 22. Effect of temperature on the IL-CNC@DP (A) & RDP (B) at different concentrations on Li ¹⁺ adsorption.....	103
Figure 23. Effect of temperature on the IL-CNC@DP (A) & RDP (B) at different	

concentrations on Mo ⁶⁺ adsorption.....	108
Figure 24. Effect of temperature on the IL-CNC@DP (A) & RDP (B) at different concentrations on B ³⁺ adsorption.....	112
Figure 25. Adsorption isotherm models used in the current study of the adsorption of Li ¹⁺ metal ions onto IL-CNC@DP.....	119
Figure 26. Plot for the calculation of the thermodynamic parameters ΔS° and ΔH° of Lithium adsorption onto IL-CNC@RDP.....	119
Figure 27. Adsorption isotherm models used in the current study of the adsorption of Li ¹⁺ metal ions onto RDP.....	120
Figure 28. Plot for the calculation of the thermodynamic parameters ΔS° and ΔH° of Lithium adsorption onto RDP.....	120
Figure 29. Adsorption isotherm models used in the current study of the adsorption of Mo ⁶⁺ metal ions onto IL-CNC@DP.....	126
Figure 30. Plot for the calculation of the thermodynamic parameters ΔS° and ΔH° of Molybdenum adsorption onto IL-CNC@DP.....	126
Figure 31. Adsorption isotherm models used in the current study of the adsorption of Mo ⁶⁺ metal ions onto RDP.....	127
Figure 32. Plot for the calculation of the thermodynamic parameters ΔS° and ΔH° of Molybdenum adsorption onto RDP.....	127
Figure 33. Adsorption isotherm models used in the current study of the adsorption of B ³⁺ metal ions onto IL-CNC@DP.....	133
Figure 34. Plot for the calculation of the thermodynamic parameters ΔS° and ΔH° of Boron adsorption onto IL-CNC@DP.....	133
Figure 35. Adsorption isotherm models used in the current study of the adsorption of	

B ³⁺ metal ions onto RDP.....	134
Figure 36. Plot for the calculation of the thermodynamic parameters ΔS° and ΔH° of Boron adsorption onto RDP.....	134
Figure 37. Groundwater concentration comparison for IL-CNC@DP and RDP for Li ¹⁺ , Mo ⁶⁺ , & B ³⁺ in the presence of other available ions.	140
Figure 38. Multi-element analysis for groundwater sample before and after adsorption by IL-CNC@DP and RDP.....	141

CHAPTER 1: INTRODUCTION

1.1 Introduction

Natural life on this planet is sustained and nurtured by water resources that have benefited individuals for many years. The services that are provided by water resources are numerous; however, they are not able to meet basic water and sanitation needs (Loucks & van Beek, 2017). Moreover, the problem arises when water demand surpasses available natural water resources leading to water scarcity (Ritchie & Roser, 2020). Additionally, other factors such as hydroclimatic and socioeconomic changes, along with an increase in the population led to the consumption of the global water that was readily available, which will ultimately contribute to water scarcity (Veldkamp et al., 2015). Therefore, this significantly impacts agricultural and industrial activities, since those two sectors consume the highest amount of water (Sorlini et al., 2015). Keeping in mind that different sources of water such as brackish water, surface water, groundwater, and other water reservoirs are used to provide potable water, which makes water treatment differ depending on its purity (Sorlini et al., 2015). However, in Qatar, two types of natural renewable resources exist groundwater and rainfall. Yet, the challenge will arise when such resources begin depleting each year (Darwish & Mohtar, 2013). Moreover, the country is moving towards prosperity in terms of economic and industrial activities with the increase in resource consumption and population, hence water challenges are expected to occur. As a result, Qatar will become unsustainable as the demand for water will increase and this will lead to a national water crisis in the region (Hussein & Lambert, 2020). Lack of rainfall is not enough to solve the issue with water demand; therefore, Qatar can rely on groundwater aquifers as the sole source of renewable water resources (Baalousha & Ouda, 2017; Ismail, 2015). This will lead to overexploitation of the groundwater that can decrease and deteriorate the quality of

the water, which will be discussed further. Numerous pollutants are being introduced in the water systems that exceed acceptable limits. Boron (B), lithium (Li), and molybdenum (Mo) were found to be 1.88 mg/L, 0.120 mg/L, and 0.053 mg/L, respectively in Qatar's groundwater aquifers (Ahmad et al., 2020). Moreover, since groundwater in Qatar is used for agricultural purposes, then this will greatly impact human consumption (Hussein & Lambert, 2020). As a result, the development of low-cost treatment technology that is able to treat and reuse groundwater for food production is the main purpose of this study. Treatment of groundwater can be performed using basic treatment methods or through advanced treatment methods. For example, basic treatment methods involve the addition of chlorine. This only works if the groundwater source is highly contaminated. On the other hand, advanced treatment methods are used to lessen the levels of MCLs (Maximum Contaminant Levels). These methods include using aeration, lime softening, ion exchange, electrodialysis reversal, or reverse osmosis. Even though such treatments have advantages, yet they are problematic due to their numerous drawbacks as demonstrated in Table 1 (Crini and Lichtfous, 2019; Gelvin & Novak, 2001).

Table 1. Summarizes the advantages and disadvantages of treatment for low-quality groundwater.

Treatment process	Advantages	Disadvantages
Aeration	Eliminates dissolved gasses such as volatile compounds	May require more energy and cost
Lime softening	Eliminates hardness and some of the metallic MCLs	Creates waste disposal problems Expensive
Iron exchange	Eliminates nitrogen compounds and arsenic pollutants at low cost and easy operation	Long production cycle Difficult to obtain a suitable resin
Electrodialysis reversal	High recovery Few to no pre-treatment required	Eliminates only ions and not organics and colloids
Reverse osmosis	High separation efficiency	Biofouling and scaling

(Crini and Lichtfous, 2019; Gelvin & Novak, 2001).

Regardless of the mentioned treatment processes, adsorption is considered a widely promising remediation technique used to treat wastewaters as a way to overcome the challenges that are associated with conventional and advanced water treatment methods. Because of its feasible, cheap, eco-friendly, and simple operation, adsorption is employed tremendously (Al-Ghouti & Al-Absi, 2020). Due to its excellent characteristics, adsorption methods were used on trace metals, dyes, and other pollutants. In particular, metals found in marine environments are a growing fear since they are considered to be toxic and carcinogenic (Wallace & Djordjevic, 2020). Therefore, one of the most adapted metal remediation techniques is adsorption. The adsorption method is undeniably the most prominent process used to remediate pollutants such as heavy metals from aquatic environments. Factors like the effect of pH, initial concentration, temperature, and adsorption mechanisms tend to have an influence on the degree of remediation (Hawari et al., 2014).

There are countless different types of adsorbents, which are used to treat and remediate water from dyes, pigments, and other contaminants, as shown in Table 2. However, nowadays, the most frequently used adsorbent for various water treatment methods is activated carbon (Bhatnagar et al., 2013). Activated carbon and other adsorbents are usually expensive, and therefore, the focus of recent research is to move towards low-cost and ecofriendly green adsorbents. A commonly used adsorbent is modified date pits that are relatively cost-effective (Al-Ghouti et al., 2017; 2013; 2010). The source of these green adsorbents is generally based on locally available resources (Pyrzynska et al., 2019). In this study, a cost-effective technique will be developed using date pits as a locally available solid waste. Furthermore, nanomaterials possess high surface area, which can be utilized to enhance adsorption capacity or removal efficiency. Hence, this study relies on conventional and well-tested acid hydrolysis technique to convert extracted cellulose from date pits to cellulose nanocrystals (CNC) (Yongvanich, 2015; Lu et al., 2013; Morais et al., 2013). The IL-CNC composite will be functionalized with RDP to create a modified adsorbent named IL-CNC@DP.

Table 2. Different types of adsorbent materials used for wastewater treatment.

Source of adsorbent	Types of adsorbents	Advantages	Disadvantages
Natural adsorbents	Clay, ore, zeolite, soil, sediment, siliceous material	Locally available adsorbent materials	pH-dependent
Agricultural Wastes	Activate carbon solid wastes (pine wood, bagasse, rice husk..)	High efficiency	Ionic competition
Industrial wastes	Activate carbon solid wastes (sewage sludge) By-products (Fly ash, alum waste, metal hydroxide sludge..)	High metal-binding capabilities Cost-effective	Weak selectivity Regeneration is required
Biomass	Yeast, seaweed, algae, fungi	Water can be recycled and reused	Deterioration may occur the number of cycles increases
Nanoadsorbents	Carbon-based nanomaterials, Nobel metal-based nanomaterials, metal oxide-based nanomaterials	Easy post-treatment after adsorption	Spent adsorbent may be hazardous waste

(Razi et al., 2017; Srivastava et al., 2016; Singh et al., 2013)

1.1.1 Research rationale

To the best of our knowledge, the adsorbent (IL-CNC@DP) is new and has not been investigated before. Yet, it is efficient and cost-effective in removing toxic elements such as Li, Mo, & B from aqueous solutions. In the future, such adsorbent can be used to treat groundwater on a larger scale as a promising technique for various elements. This can help with enhancing and improving the quality of groundwater, which in turn provides a better advantage to the agricultural sector. The outcomes of this research play an important role in key issues of Qatar, which have been highlighted in Qatar

National Vision 2030 and Qatar National Development Strategy (2018-2022) i.e. diversifying the economy by introducing new ways of extracting valuable materials from wastes, developing low-cost materials, water resource management, and preserving the quality and quantity of groundwater resources of Qatar.

1.1.2 Research hypothesis

Hypothesis 1: Cellulose extracted from date pits produces cellulose nanocrystals (CNC), as a novel biomaterial available in Qatar.

Hypothesis 2: Ionic liquid (IL) can be effectively used to create a composite with cellulose nanocrystals (CNC).

Hypothesis 3: Newly developed IL-CNC@DP will be effective for the adsorption of toxic elements (B, Li, and Mo).

Hypothesis 4: IL-CNC@DP can be used on real groundwater samples in Qatar to test the selectivity of the adsorbent towards B, Li, and Mo.

1.1.3 Research objectives

The goal of this study is to prepare a low-cost and environmentally friendly adsorbent by using date pits that are commonly found as an agricultural waste in Qatar based on the following experiments:

- i. Extraction and preparation of cellulose nanocrystals (CNCs) from locally available date pits.
- ii. Preparation of ionic liquid/cellulose nanocrystals (IL-CNC).
- iii. Functionalization of date pits (DP) with the prepared IL-CNC (IL-CNC@DP).
- iv. Application of the modified IL-CNC@DP and unmodified RDP for the removal of toxic elements (Li, Mo, & B) through adsorptive batch studies from aqueous solutions.
- v. Testing of real groundwater samples isolated from Qatar for the selectivity of

the adsorbents.

- vi. Desorption studies of Li, Mo, & B from the modified and unmodified adsorbent.
- vii. Characterization of the prepared adsorbents and intermediate products by FTIR, SEM, XRD, TEM, BET.

CHAPTER 2: LITERATURE REVIEW

2.1 Groundwater in Qatar

Groundwater composes around 98% of all the usable freshwater found on earth and it is around 60 times as abundant as the freshwater found in lakes and streams (Mullen, 2021). In general, a variety of different elements is dissolved in groundwater. Comparing surface water with groundwater, groundwater has high concentrations of elements. Moreover, it is also due to the interactions of the soil, atmosphere, and the surficial environment. Major dissolved components such as bicarbonate, chloride, sulphate (anions), and sodium, calcium, magnesium, potassium (cations) are found in groundwater. Other types of dissolved constituents such as trace elements are also found depending upon the aquifer (Merkel et al., 2005). In most cases, groundwater is not noticeable when bearing in mind the total amount of water found on earth, however, water that exists beneath the surface is a significant valuable resource (Mullen, 2021). Therefore, protection from pollutants and contaminants will guarantee the groundwater's future since it has a vital role in the environment. Nonetheless, the water crisis around the world has been a major issue for many decades. This is due to the fact that population, urbanization, and industrial activities are increasing tremendously each year (Biswas & Tortajada, 2019). Arid regions, such as Qatar, depend widely on seawater desalination processes to provide the water need for the nation, while groundwater supplies industrial and agricultural sectors. It has been estimated that in 2018, water-scarce areas accounted for 36% of the global population as reported by the World Bank and the United Nations (Biswas & Tortajada, 2019). The World Resources Institute (WRI) has listed Qatar as one of the most water-scarce countries as the demand for water is increasing (Biswas & Tortajada, 2019). Moreover, groundwater extraction

is estimated to be 220.2 Mm³ in 2004-2005 for Qatar (Darwish & Mohtar, 2013). Therefore, the exploitation in Qatar's groundwater is increasing, therefore a significant decrease in the levels of existing aquifers. According to water statistics (2015), the removal rate from groundwater systems is higher than the amount of recharge rates by 30 times. Therefore, this has led to a decrease in the level of groundwater in Qatar. Therefore this will result in a rise in salinity levels. Irrigation using groundwater is causing saline levels in soils to increase and desertification in some regions (Darwish & Mohtar, 2013). According to Elsaid (2017), groundwater in Qatar has total dissolved solids (TDS) that range from 1000 mg/L to 7500 mg/L. Therefore, these results can rise reverse osmosis (RO) membrane scaling which needs further maintenance that makes it expensive to maintain (Colburn et al., 2016). Since Qatar is considered an arid region, therefore the management of its water resources is not an easy task because of the inadequate source of water and its accessibility in the region. Moreover, climatic changes tend to play a huge role in such cases (Rajmohan et al., 2019). In general, groundwater systems are highly impacted by two factors: natural and anthropogenic activities. Therefore, this water will not be suitable for either irrigation or domestic use (Mallick et al., 2018). Taking into consideration several factors such as high evaporation rates, weathering of minerals, salinity, metals levels, sea-level rise, which can also impact the quality of groundwater (Alfy et al., 2017). In Qatar, all the fresh groundwater comes from rainfall excluding the water in Abu Samara. The reason is that it receives its inflow from the West of Saudi Arabia making it slightly saline (Ahmad et al., 2020). The classification of groundwater basins in Qatar is named as Abu Samara, Doha, North, and South groundwater basins (Ahmad et al., 2020). The wells or basins in the North and South compromise 70% and 28%, respectively, of the total wells found in Qatar (SWS, 2009).

2.1.1 Metal Contamination in Qatar's Groundwater

Groundwater quality deteriorates because it contains several contaminants. Metalloids and toxic metals can become a concern when they exceed the acceptable limits. Boron (B), lithium (Li), and molybdenum (Mo) were found in Qatar's groundwater to be 1.88 mg/L, 0.120 mg/L, and 0.053 mg/L, respectively (Ahmad et al., 2020). The fact that they are toxic to agricultural products makes them a major concern that needs to be addressed to avoid their toxicity (Shi et al., 2018). Other studies discuss the availability of pathogenic microbes and other toxic chemicals that tend to pose serious risks when reused (Al-Maadheed et al., 2019). According to Tesoriero et al. (2004), contamination of groundwater shallow aquifers can easily occur due to the transportations of the contaminants to the water table and the hydrogeological surroundings.

Contamination of groundwater with trace elements is directly related to industrial, agricultural, and anthropogenic activities (Wu et al., 2016; Güler et al., 2012). For example, cobalt, lead, and nickel are common heavy metals that endanger humans and the environment. Heavy metals are toxic elements that are characterized by their high density and low concentration levels (Jarup, 2003). These heavy metals are considered trace elements due to the fact that they exist in low concentrations (He et al., 2005). Moreover, water discharges by industrial processes and atmospheric pathways are two principal sources where metals can persist in the environment (Repo et al., 2011).

Molybdenum could be found in drinking water and certain types of foods like legumes and grains, but high levels of molybdenum can cause health issues (WHO, 2003). In the United States, molybdenum concentration levels from 2 µg/L to 1500 µg/L present in 32.7% of 15 major river samples (Kopp & Kroner, 1967). On the other hand, molybdenum present in Qatar's groundwater, when compared to other countries,

demonstrates high levels, thus this creates an issue for Qatar's inhabitants when it comes to drinking water. Kuiper et al. (2014) investigated urinary molybdenum levels in farmworkers in Qatar due to their ingestion of groundwater or the consumption of irrigated crops. The results present urinary molybdenum levels ranging from 9.59 µg/L to 737 µg/L, which were considered extremely high when compared to other similar studies. Moreover, molybdenum found in groundwater can be influenced by four factors, as reported by Smedley et al. (2014). The molybdenum in the aquifer is reducing; the aquifer contains multiple iron oxides and sulfides minerals, the groundwater pH ranges from neutral to alkaline, and lastly an increase in the residence time of the groundwater. Besides, it has been reported that an increase in molybdenum concentration is linked with salinity levels found in groundwater, especially in arid regions, where soils are saline (Leybourne and Cameron, 2008). Hence, Qatar is tremendously susceptible to have high levels of molybdenum. Another study by Kuiper et al. (2015) proved that Qatar's groundwater has extremely high levels of molybdenum when compared to many countries. The samples were collected from many regions in Qatar, especially from the northern groundwater basin. Qatar had a mean value of 26.9 µg/L, which is considered the highest, in comparison to global means. This research further proves that molybdenum levels present in groundwater can be high even though other trace elements investigated are below the WHO guidelines.

Moreover, lithium (Li) is another type of metal that is commonly found in soil and water environments. It is mainly used in commercial and industrial sectors for the production of batteries, glass, ceramics, and as a catalyst for chemical reactors (Moore et al., 1997). Most of the studies performed were done on lithium in potable water and the correlation it has with suicide mortality rates (Helbich et al., 2015; Blüml et al., 2013; Helbich et al., 2012; Kapusta et al., 2011). However, other studies focused on

extracting lithium from seawater by relying on the adsorption method using manganese oxide as an adsorbent (Liu et al. 2015; Park et al. 2015; Wajima et al. 2012). Since lithium is considered a very rare metal and the increasing demand for it in the coming years will keep on rising, developing various methods for the recovery of lithium is essential. As stated by Murodjon et al. (2020), recovering lithium from seawater, brine, or geothermal water by precipitation, extraction, membrane separation, and adsorption are the commonly listed methods for recovery. The most promising method is proved to be the adsorption method because of its eco-friendly nature and cheapness.

Another pollutant such as boron (B) has an increasing demand to obtain clean water for drinking purposes. This metalloid can be found in most natural resources and the typical boron concentrations in seawater in the Arabian Gulf territories ranges from 4.5 mg/L to 5.0 mg/L and sometimes can surpass this range up to 7 mg/L (Repo et al., 2003). Even though boron is an important trace element for vegetation, it is considered a limiting factor because having it in excess can cause detrimental impacts on plants and crops (Repo et al., 2003). For instance, an increase in boron concentrations was observed in Eilat city after farmers saw noticeable crop poisoning. This caused further post-treatment methods for water by using seawater reverse osmosis (SWRO) plant and the results proved to remove boron efficiently (Fritzmann et al., 2007). According to Li et al. (2011), the elimination of boron from synthetic seawater was successful by using fabricated boron adsorbent. This adsorbent demonstrated a high chemical affinity and adsorption capacity. Other studies removed boron from landfill leachate wastewater by electro-dialytic method (Turek et al., 2007), ceramic industry wastewater by adsorption/flocculation (Chong et al, 2009), synthetic wastewater by ion exchange (Yılmaz et al., 2005), and landfill leachate by adsorption/co-precipitation (Turek et al., 2007). However, according to a review, the most reliable and appropriate technology

for boron removal is reverse osmosis (Kabay et al., 2010).

2.1.2 Physical and chemical properties of groundwater samples in Qatar

It has been reported that the temperatures of the water from the aquifers range from 17.3 °C to 31.7 °C, averaging at 27.7 °C. The reason for these differences amongst all the collected samples was explained due to the recharge rates that occur because of rainfall. Furthermore, it is important to note that the groundwater found at the bottom of the aquifers has relatively high temperatures than the ones found on the surface of the aquifers (Ahmad et al., 2020). This new study presented another parameter, where they studied the pH values of different locations of groundwater basins. It was found that the pH measurement ranged from 6.8 to 7.9, averaging at 7.3 (Ahmad et al., 2020). By comparing these results to the WHO standards, it can be concluded that they are within their reported standards of 6.5-8.5 (WHO, 2017). It is worth mentioning that at ordinary conditions the groundwater itself does not demonstrate high metal concentrations (Shomar, 2015). Another parameter that was discussed was the total hardness of the groundwater, where it ranged from 275 mg CaCO₃/L -5393 mg CaCO₃/L, averaging at 2120 mg CaCO₃/L. Therefore, it is classified as generally being very hard. In the study, the electrical conductivity (EC) proved that the groundwater samples were close to freshwater samples and few samples were highly saline due to the high aridity of Qatar's location because of low rainfall and high evaporation rates. On the other hand, total dissolved solids (TDS), was found to be 5038 mg/L. Moreover, groundwater can consist of multiple chemicals that can be generally found at different levels. For example, Na⁺, K⁺, Ca²⁺, Mg²⁺, and other ions are present and that could be due to the lithology of the rocks that are found in basins along with anthropogenic sources (Ahmad et al., 2020; Abdel-Satar et al., 2017). Some of the physicochemical characteristics of the groundwater samples are listed in Table 3, where they were

collected from 41 sites throughout Qatar post-winter season. Furthermore, many other elements (not shown) were also detected in the groundwater samples.

Table 3. Summary of the physicochemical characteristics of the groundwater samples. Modified from Ahmad et al. (2020).

Parameter	Number of Samples	Minimum	Maximum	Mean
pH	41	6.89	7.94	7.30
Conductivity ($\mu\text{S}/\text{cm}$)	41	0.92	22.33	7.29
TDS (mg/L)	41	598.87	15633	5038.1
TOC (mg/L)	41	1.27	35.50	14.62
SAR	41	1.55	33.27	12.781
Hardness	41	275.16	5393.0	2120.2
Lithium ($\mu\text{g}/\text{L}$)	41	23.34	236.7	120.6
Boron ($\mu\text{g}/\text{L}$)	41	388.0	3819	1885
Molybdenum ($\mu\text{g}/\text{L}$)	41	7.830	294.0	53.88

Therefore, this study was performed specifically on three pollutants: boron (B), lithium (Li), and molybdenum (Mo) based on the recent study carried out by Ahmad et al. (2020). The study concludes that lithium levels in 39 samples surpassed the GCC Standardization Organization (GSO) and Qatar (KAHRAMAA) requirements, molybdenum levels in 9 samples surpassed the World Health Organization (WHO), GSO, Qatar drinking water guidelines, and other 23 samples surpassed the United States Environmental Protection Agency (US-EPA) lifetime health advisory. As for boron, it surpassed the WHO, GSO, and Qatar drinking water guidelines for 8 samples.

2.1.3 Causes of groundwater deterioration

As previously mentioned, climate change plays a major role in Qatar due to the decrease in rainfall and increase in evapotranspiration levels that tends to decrease the recharge rates of groundwater basins. In addition, sandy storms and erosion of soils may be the main lead of the prominent changes that occur in the topsoil characteristics (Shomar, 2015). Moreover, an increase in salinity levels due to the over-exploitation of the groundwater by extraction activities, which results in bringing more salty water from nearby bodies of water (Suursoo et al., 2017). Hence, the dissolved solids might increase above the normal levels. Another reason could be due to the soils that contain high levels of metals that are highly mobile. This means that these metals can easily move from the soils and increase the levels of metal in groundwater (Shomar, 2015). Keeping in mind that the usage of fertilizers, pesticides, herbicides, and other threatening contaminants are considered the sources of anthropogenic causes of groundwater deterioration (Seyedmohammadi et al., 2016). Oil and gas industries contribute to the production of "produced water". This water has residues of organic and inorganic contaminants mixed, where they are sometimes discarded and disposed of into the sea or deep wells without treatment (Shomar, 2015). In a study by Galitskaya et al. (2013), the hydrogeochemical changes of carboniferous aquifers are not only induced naturally but also by humans themselves. They listed the reasons as mainly being the exploitation of the groundwater basin. Other than the mentioned factors above, the interaction of rocks within the aquifer and the soils can be another indication of why the quality of groundwater is reduced (Ahmad et al., 2020).

Shallow and surface coastal aquifers are known to be the most vulnerable because of the small distance the aquifers have from the surface soils. (Shomar, 2015; Kuiper et al., 2015). Anthropogenic contamination from wastewater or polluted effluents could

penetrate and infiltrate into the aquifers and spread over an entire area of an aquifer (Baalousha, 2016). For example, coastal and northern Qatari aquifers are considered shallow aquifers that have high hydraulic conductivity that is extremely vulnerable because of the depression areas. On the other hand, southern Qatari aquifers are considered the least vulnerable because of the thick formations of clay layers that work great in blocking the infiltration of contaminants (Baalousha, 2016). Therefore, groundwater quality can be impacted and deteriorated by natural and anthropogenic sources, as mentioned above. Hence, understanding the groundwater system in Qatar is crucial due to its usefulness since it is the only source for agricultural purposes. Moreover, developing sustainable management plans that focus on an integration assessment method of hydrogeochemical systems can be a way to move forward (Ahmad et al., 2020). Nonetheless, other than integration methods, finding a way to remove, remediate, or decontaminate the groundwater from pollutants, such as metals, can be part of enhancing the groundwater quality.

There are other studies performed in several regions around the world that present the different concentrations of lithium, molybdenum, and boron in groundwater as shown in Table 4. Comparing these results to the study investigated in Qatar, it is evident that the findings differ from one country to another. This is due to the natural and anthropogenic contamination of the groundwater resources, as discussed previously.

Table 4. Summary of some groundwater studies for lithium, molybdenum, and boron.

Element	Concentration	Country	Reference
Lithium	<1-396 µg/L (public supply wells)	United States	Lindsey et al., 2021

	<1-1700 µg/L (domestic supply wells)		
	0.120 mg/L	Qatar	Ahmad et al., 2020
	4.76 mg/L	Tunis	Souid et al., 2018
	0.16 - 3.82 mg/L	Rajasthan, India	Das, 2014
	0.053 mg/L	Qatar	Ahmad et al., 2020
Molybdenum	0.13-4.9 µg/L	United States	Ayotte et al., 2011
	<0.5–6.8 µg/L	Hungary/Romania	Rowland et al., 2011
	<0.1–13.2 µg/L	Portugal	de Melo & da Silva, 2008
	<0.1–8.3 µg/L	Belgium	Coetsiers & Walraevens, 2008
	1.88 mg/l	Qatar	Ahmad et al., 2020
Boron	> 0.5 mg/l & > 1.0 mg/l (from 7.8% and 1.2% of the samples respectively)	Andhra Pradesh And Telangana States, India	Sankar et al., 2018
	4.91 mg/L	Rio Secco - Italy	Pennisi et al., 2006
	2.1 mg/L	Bangladesh	Ravenscroft &
	6.1 mg/L	Ingham County, Michigan	McArthur, 2004

2.2 Cellulose overview

Cellulose is a linear polysaccharide that consists of chains of β -1,4 linked D-glucose. This biopolymer is the utmost plentiful renewable organic polymer on earth. Over the years, the usage of crystalline celluloses in material production has spiked an interest amongst research fields. Such organic polymers can be used as a strengthening material with other polymers because of their unique characteristics (Dharmalingam et al., 2019; Medina et al., 2019; Ferreira et al., 2018; Khalil et al., 2018). There are different kinds

of cellulose particles that can be isolated from several cellulose materials such as cellulose nanocrystals (Khan et al., 2020; Kian et al., 2019; Wang et al., 2019; Zheng et al., 2019) or cellulose nanowhiskers (Araki & Miyayama, 2020; Jafari et al., 2020; Khattab et al., 2020), microcrystalline cellulose (Abu-Thabit et al. 2020; Alavi, 2019), and microfibrillated cellulose (Silva et al., 2020; Li et al., 2018). The source of cellulose material and the extraction methods are important factors that determine the crystallinity, crystal structure, aspect ratio, and morphology of the extracted cellulose particles (Trache et al., 2016; Deepa et al., 2015). Previous researches have shown the possibility of cellulose and nanocellulose isolation from various sources, such as wood paste (Dong, 2016), banana stalk (Muller et al., 2014), pistachio hull (Marett et al., 2017), pine and corn bark (Ditzel et al., 2017), wood (Rajinipriya et al., 2018), cotton (Morais et al., 2013), ramie (Syafri et al., 2018), bagasse (Li et al., 2012), bamboo (Brito et al., 2012), sisal (Morán et al., 2008), and many others. Moreover, locally available solid wastes such as using date pits are an excellent source for extracting cellulose since they contain as much as 42% cellulose (Ogungbenro et al., 2018).

Scientists and researchers are trying to come up with a way to use raw materials, which are economically and environmentally friendly. Therefore, the usage of cellulose, as a biopolymer and a sustainable raw material, is the most appropriate choice because of its abundance found on earth (Abu-Thabit et al., 2020; Etale et al., 2020). The process of obtaining cellulose on the nanoscale can be performed mechanically or chemically by modifying the type of polymer used (Börjesson & Westman, 2015). This nanofiber possesses a biodegradable property with low density and an impressive firmness material (Phanthong et al., 2018). Comparing cellulose to nanocellulose, nanocellulose polymers have great characteristics like high hydrophilicity, surface area, and crystallinity (Zheng et al., 2019). Such characteristic makes the usage of nanocellulose

relatively appealing because of the various applications where nanocellulose is utilized in. Moreover, those cellulose nanomaterials hold great potential in water treatment after already demonstrating their application in paper and packaging, textile industries, and other fields (Carpenter et al., 2015). Nanocelluloses are employed in a variety of applications whether it is on a large or small scale. For example, the improvement of mechanical and barrier properties of interior panels in automotive is one of the types of large-scale applications of nanocellulose (Lyne, 2013). Other types of large-scale can include the use of nanocellulose in cement or concrete construction as it tends to increase the rigidity and toughness of fragile materials (Ardanuy Raso et al., 2012). Moreover, paper and packaging industries rely on nano-based products to replace polystyrene-based foams and to reduce the production of cost, which reduces energy consumption (Börjesson & Westman, 2015). As for small-scale applications, nanocellulose can be used in aerogels production, as they are efficient in absorbing oil from water (Cervin et al., 2012). Furthermore, industrial activities make use of nano-products since they are used as viscosity modifiers that can reduce oil thinning as temperature increases. Also, they are used in water purification by the adsorption process (Dufresne, 2017). In construction processes, they tend to make use of nanocellulose since they provide an excellent wallboard-facing material that resists mold growth while being water-resistant (Sundqvist-Andberg, 2013). Lastly, an emerging field of applications in electronics like organic light-emitting diodes (OLEDs) enables huge applications in optoelectronics (Hu et al., 2013).

2.2.1 Extraction of cellulose nanocrystals (CNC)

As previously mentioned, the cellulose source and extraction process determines the properties of the cellulose polymer; likewise, nanocellulose depends upon the same

factors (Deepa et al., 2015; Sacui et al., 2014). Therefore, such factors can help determine the different classifications of nanocellulose. In general, nanocellulose can be classified into three types of materials; nanocrystalline cellulose (NCC) or cellulose nanocrystals (CNCs), nanofibrillated cellulose (NFC), and bacterial nanocellulose ones (BNC) (Kian et al., 2019; Kontturi et al., 2018; Jawaid et al., 2017; García et al., 2016). Even though such materials are the same regarding their chemical structure, they differ in their morphologies and treatment methods. According to numerous researchers, there are various methods for the production of CNC such as mechanical method, ionic liquid method, enzymatic method, TEMPO oxidative method, combination method (oxidative or enzymatic and mechanical), and acid hydrolysis by different acids such as sulfuric acid, phosphoric acid, hydrochloric acid (Guo et al., 2020; Ribeiro et al., 2020; Ribeiro et al., 2019; Peretz et al., 2019). Among all these methods, acid hydrolysis by sulfuric acid has been known as the most widely used method for CNCs extraction due to its simplicity as well as resulting in the nanoparticle of 100 to 1000 nm with high crystallinity and stiffness (Wulandari et al., 2016; Börjesson & Westman, 2015; Shanmugarajah et al., 2015; Lani et al., 2014). Several papers optimized the usage of sulfuric acid to produce CNC by using the acid at an adjusted percentage and under optimum temperature and time (Khan et al., 2020; Guo et al., 2020; Zheng et al., 2019; Shanmugarajah et al., 2015; Hamad et al., 2010; Beck-Candanedo et al., 2005). This method includes using the acid at 64% under 45 °C for approximately an hour. Then, the acid hydrolysis reaction is stopped with deionized water. In the end, the suspension is centrifuged and dialyzed to obtain neutral pH. The final step is to sonicate to attain separate cellulose nanocrystals. Researchers reported using sulfuric acid under different reaction times demonstrated different polydisperse length distribution and sulfur content. For example, employing 64% sulfuric acid at 45°C for two different reaction

times, 25 and 45 mins, proved that certainly, the effect of hydrolysis conditions impacts the length and polydispersity of the cellulose depending upon the acid to pulp ratio. This means that the longer the reaction time, the less the polydispersity and the more the sulfur content in comparison to the shorter reaction time (Hamad et al., 2010; Beck-Candanedo et al., 2005). Hamad and his coworkers used different sulfuric acid concentrations that demonstrated different degrees of polymerization, crystallinity, size, and yield of crystals (Hamad et al., 2010). The experiment was based on using 16%, 40%, and 64% of sulfuric acid concentrations under 45 °C, 65 °C, and 85 °C of different temperatures at 25 min of total reaction time. The results show that the higher the acid concentration and the higher the reaction temperature, the lower the degree of polymerization. Also, samples that were hydrolyzed with the highest sulfuric acid concentration (64%) demonstrated a yield drop in all the temperatures (45 °C, 65 °C, and 85 °C) that were examined. Moreover, a decrease in the polymerization degree during the acid hydrolysis process will cause an increase in the crystallinity of the cellulose, which will in turn cause smaller crystals. Another older study analyzed the impact of preparation conditions has on the formation of cellulose crystals (Dong et al., 1998). The study used 64% sulfuric acid under a variety of temperatures for 15 min up to 18 hrs. The lowest temperature required the reaction time to be the longest, which is 18 hrs for the suspension to form properly. However, at the highest temperature, the reaction proved to be difficult to manage and the suspension turned to black indicating another side reaction that took place such as dehydration. It is reported that the best scenario would be to subject the treatment under 45°C for 1 hr. They also mentioned the association between the reaction time and the crystallinity size, where the reaction at first is fast but gradually started to slow down. The decrease in the reaction was because of the acid that diffused in the amorphous regions of the cellulose and

hydrolyzed the glycosidic bonds. This means that the harder it is for the glycosidic bonds to be hydrolyzed, the slower the reaction would occur. Moreover, after the first hour of the reaction that took place at 45°C, the size of the crystals became more stable. The main reason for the employment of CNCs in many applications is due to their fascinating properties. They have rod-shaped morphologies with a large surface area that ranges from 150-250 m²/g with low density at 1.566 g/cm³ and a high aspect ratio of 10 – 85 (Shafizah et al., 2018). Furthermore, they possess nano sectional fibers with nano dimensional cross-sectional morphologies (Isogai et al., 2011). There are several sources as mentioned where cellulose can be obtained from, either from crops, industrial residues, or animal residues. The biomass extracted has three main components: cellulose, hemicellulose, and lignin (Díez et al., 2020; Jung et al., 2015; Isik et al., 2014). Cellulose is a linear polysaccharide, while hemicellulose is a highly branched random structure polymer, which is made of many types of saccharides that are mostly amorphous. In addition, lignins are also amorphous polymers composed of phenyl-propane units that mainly entail aromatic units like guaiacyl and syringyl (Morán et al., 2008). Each cellulose fibril is made up of a crystalline and amorphous (non-crystalline) region (Song et al., 2014). To obtain the crystalline region to produce CNCs, the amorphous region of cellulose fibers needs to be separated (Brinchi et al., 2013). Therefore, the extraction of CNC normally consists of two processes, chemical purification, and acid hydrolysis. The chemical purification process is carried out for the elimination of the amorphous region to produce chemically purified cellulose through various steps, namely dewaxing, bleaching, and alkali treatment. This results in a black solution that consists mostly of lignin materials and the cellulose are obtained as a residue after. The next process involves bleaching that oxidizes the soluble basic materials. Furthermore, after sulfuric acid hydrolysis, stable CNC suspension is

obtained. Figure 1 represents a schematic illustration of the acid hydrolysis process. Moreover, since environmental conservation is a growing concern, it encouraged researchers to develop decomposable resources from natural sources for various applications. Different studies focused on utilizing agricultural wastes to attain more precious materials, which can be applied in several applications such as a sustainable alternative. Using residual biomass gives an added value to the waste products as well as giving new renewable materials.

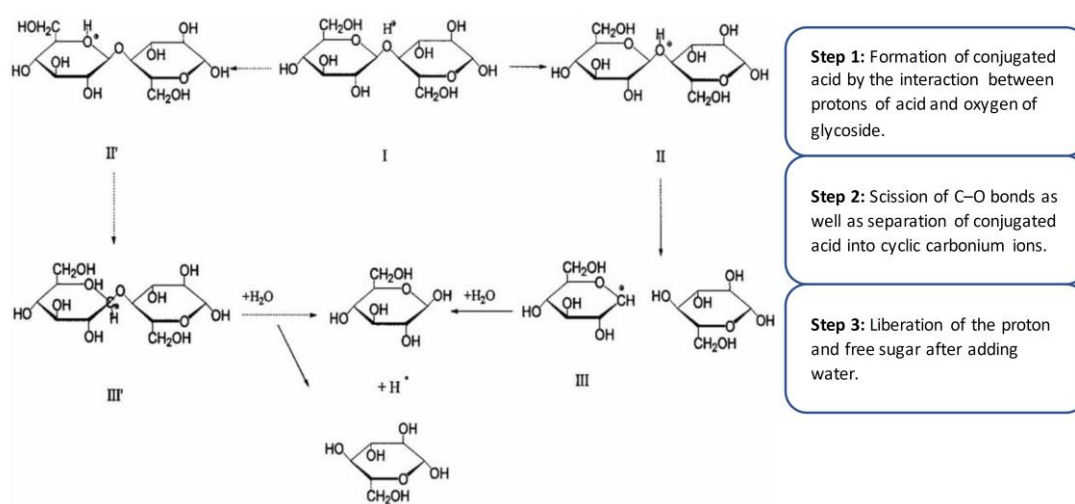


Figure 1. Schematic illustration of acid hydrolysis process of the scission of glucosidic bonds (Jonoobi et al., 2015).

2.3 The application of Ionic liquids (IL)

A novel adsorbent containing CNC and IL can be used to impregnate ground date pits to investigate their interaction with the elements and microorganisms and their removal

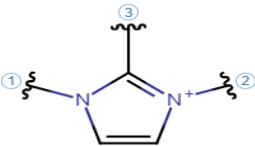
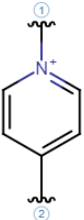
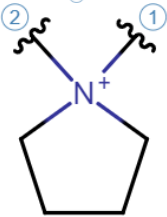
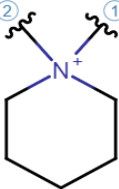
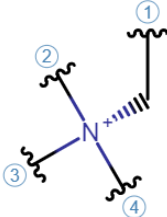
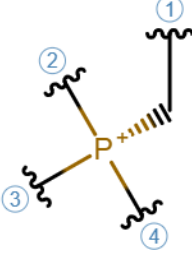
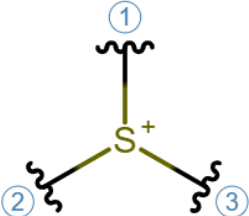
efficiency. Ionic liquids (IL) are salts that have melting points below 100 °C (Verma et al., 2019). In the past, ionic liquids started to gain attention when they were used as electrolytes for batteries in the 1960s. The mixture of 1-butylpyridinium chloride ([BPy]Cl) and aluminum chloride (AlCl₃) was the first generation of IL used. Such mixtures had limitations due to their sensitivity in air and electrochemical reduction. Nevertheless, the second generation of IL overcomes those obstacles by developing air and water solutions. Some organic cations of ionic liquids are alkyl imidazolium [R₁R₂IM]⁺, tetra-alkyl ammonium [NR₄]⁺, alkyl pyridinium [RPy]⁺, and tetraalkyl phosphonium [PR₄]⁺. Other anions include nitrate [NO₃⁻], tetra-fluoroborate [BF₄⁻], methanesulfonate [CH₃SO₃⁻] and hexafluorophosphate [PF₆⁻]. Therefore, 10¹² different combinations of IL tend to exist (Pinkert et al., 2009). ILs are applied in many fields such as environmental sciences, chemistry (e.g. solvents, catalysts, reagents), chemical engineering (e.g. lubricants, liquid membranes, surfactants), biology and pharmacy (e.g. biocides, drugs), electrochemistry (e.g. batteries, sensors), and other applications (e.g. polysaccharides, liquid crystals) (Verma et al., 2019). In addition, ILs possess unique properties in which they have high thermal stability, low vapor pressure, inflammability, and melting temperature, and viscosity that depends on the nature of anions. Even though they are reported as "green solvents" (Holbrey et al., 2003), however, if they are released into the environment, they can become toxic and nonbiodegradable (Deetlefs & Seddon, 2010).

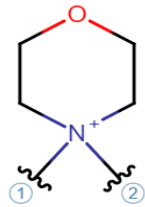
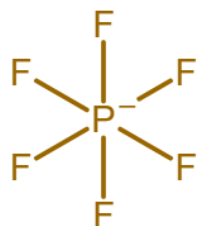
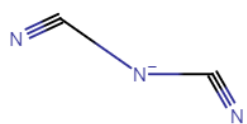
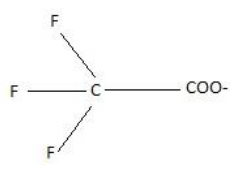
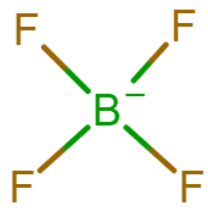
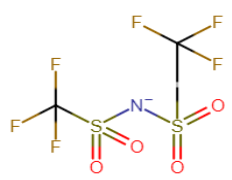
Zante et al. (2019) successfully demonstrated the use of supported ionic liquid membranes (SLMs) to extract lithium. The SLMs were used to separate lithium cations from a mixture of an aqueous solution by impregnating mixtures of hydrophobic ionic liquid. Impregnation of membranes shows that the mass uptake of ionic liquids is affiliated with the density of the organic phase. Moreover, the stability of the membrane

is associated with the solubility of the organic stage. As a result, due to the several useful features of ILs, they have been shown to combine with nanomaterials for combined functionalities and their use has been demonstrated in catalysis and separations. Another study reported that ILs could be applied to dissolve cellulose to fabricate cellulose nanofiber with gold nanoparticles as a hybrid. This hybrid could be later on used for the application of cellulose/gold nanoparticle sensors or the production of low-temperature catalysts (Li & Taubert, 2009). Adsorption of ILs is also applicable by using an adsorbent such as activated carbon. Hydrophobic ILs found in water streams can be adsorbed by modifying the surface of the adsorbent and the size of the cation and anion IL (Palomar et al., 2009). Hence, ionic liquids can be applied for better thermal stability, ionic conductivity, and good solubility for cellulose to give rise to ionic liquid-cellulose nanocrystals composites (IL-CNC).

Ionic liquids at room temperature are sometimes deemed as RTILs. They are also considered molten electrolytes with a melting temperature of less than 373 kelvin. They are made up of ions, where the anions are inorganic, and the cations are asymmetric organics. This allows the researcher to have several ways in designing the ionic couples due to the variation in the chain length, ring substituents, and the different combinations of cation and ions together (Freemantle, 2010; Fei et al., 2006; Rogers & Seddon, 2003). ILs exhibit many structures that can be attached with several other alkyl groups. Table 5 provides an idea about the commonly used ILs in scientific research.

Table 5. Summarizes the commonly used ionic liquid of cations and anions.

Cation	Molecular Formula	Structure
Imidazolium	$C_3H_5N_2^+$	
Pyridinium	$C_5H_6N^+$ / $HC_5H_5N^+$	
Pyrrolidinium	$C_4H_{10}N^+$	
Piperidinium	$C_5H_{12}N^+$	
Ammonium	NH_4^+	
Phosphonium	PH_4^+	
Sulfonium	H_3S^+	

Morpholinium	$C_4H_{10}NO^+$	
Anion	Molecular Formula	Structure
Hexafluorophosphate	F_6P^-	
Dicyanamide	C_2N_3	
Chloride	Cl^-	Cl^-
Bromide	Br^-	Br^-
Trifluoromethanesulfonate	$CF_3O_3S^-$	
Tetrafluoroborate	BF_4^-	
Bis(trifluoromethylsulfonyl)imide	$C_8H_{15}N_2$ $C_2F_6NO_4S_2$	

2.4 Adsorption mechanisms and their application in water treatment

The mechanisms of adsorption occur on a surface of a sorbent and the adsorbed substance on the surface is called sorbate (Bushra et al., 2016), as shown in Figure 2. There are many treatment methods, which can be considered to remove pollutants from wastewater. However, adsorption is the most appropriate since it is simple, cost-effective, sustainable, and insensitive to toxic pollutants (Sharma et al., 2011). The adsorption process can be physical or chemical depending on the adsorbent and adsorbate attraction forces (Kandasamy et al., 2006). In an aqueous environment, the uptake of inorganic and organic materials can be performed by various adsorption mechanisms (Al-Ghouti et al et al., 2010). Moreover, CNCs can be applied in wastewater treatment as an adsorbent since they are considered to be nontoxic and have relatively large surface areas. One of the first studies that demonstrated the usage of CNCs proved that those nanoparticles adsorbed methylene blue at a high capacity of 101 mg/g according to the Langmuir isotherm model (He et al., 2013). Another study demonstrated the use of cellulose nanocrystals-alginate (CNC-ALG) hydrogel beds to remove methylene blue dye. The composite material of the CNC and the hydrogel beds aided with the adsorption of the dyes in fixed-bed columns (Mohammed et al., 2016). Yang et al. (2014) specified that the CNCs could be impregnated into aerogels that can form a cross-linkage between CNC and aerogels. This method enhanced the adsorption surface area by increasing and improving its mechanical properties.

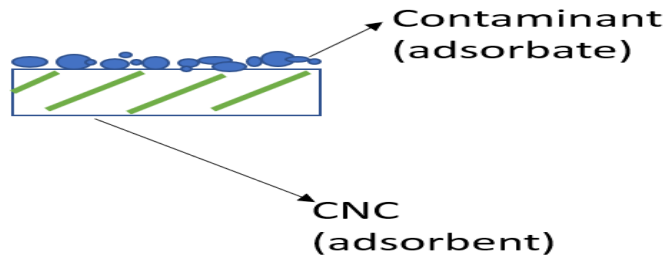


Figure 2. Demonstration of the adsorption mechanism between the adsorbent and adsorbate (Bushra et al., 2016).

Ionic liquids can be used to synthesize nanocomposites as selective adsorbents. For example, desulphurization of gasoline was possible due to the significant properties of graphene-modified with ionic liquids according to PourSaber (2014). The magnetic composite (LI-MGO) provided high adsorption capacity to construct a new nanocomposite for the removal of sulfur from gasoline. The results showed that in 20 minutes, 58% of thiophene was removed under ideal conditions. This novel magnetic composite presents adsorption that conforms to the Langmuir model, where the adsorption capacity of the nanocomposite is found to be 113 mg/g for thiophene (PourSaber, 2014). Other studies relied on ionic liquid-coated magnetic graphene oxide for the extraction of protein. The removal of protein by adsorption was enhanced by using nanocomposites from real biological samples (Wen et al., 2016). One of the most recent studies also used magnetic oxide nanoparticles modified with ionic liquids (LI-MGO) for phenol removal from aqueous solutions (Gholami-Bonabi et al., 2020). This study focused on how important experiential factors such as pH and dosage of adsorbent are, along with modification performed with ionic liquid. The findings showed that the optimal removal of phenol was observed at pH 3 with a nanocomposite

concentration of 0.04 g/L. This provides a way to obtain an enhanced quality of water due to the high removal rate and cost-effective technique by relying on magnetic oxide nanoparticles modified with ionic liquids.

For example, defluoridation can be removed by several methods that are considered to be costly and require high consumption of energy (Pillai et al., 2019). Therefore, according to Ekka et al. (2017) phosphonium and imidazolium-based ionic liquids (IL) are used to remove fluoride from water. In this case, the ionic liquid can work as a promising adsorbent when the ionic liquid is modified with iron oxide. The removal of fluoride occurs because of interactions between iron oxide and ions of fluoride that are existing in water, where they found the maximum adsorption of fluoride to be 67.9 mg/g based on the Freundlich isotherm model (Pillai et al., 2020). The idea behind the interaction of fluoride ions and ionic liquid metal oxides is supported by literature studies that stated that the interaction of fluoride ions and ionic liquid metal oxides could be due to electrostatic, hydrogen bonding, and cations π bond (Lee et al., 2013). Another successful study demonstrated the usage of ionic liquid-alumina as a novel adsorbent to remove fluoride (Ekka et al., 2017). The maximum adsorption of fluoride is found to be 25.0 mg/g based on the Langmuir adsorption isotherm model. Therefore, alumina-modified ionic liquid proved to have an affinity towards fluoride in contaminated water. Both studies provide an important insight on promising adsorbents using ionic liquids for fluoride removal.

Moreover, previous researches have shown the adsorption characteristics of modified date pits for trace metals, dyes, and other pollutants are very effective (Al-Ghouti et al., 2017; 2013; 2010). Around 755 thousand tons of date pits (DP) as wastes are generated worldwide, which can be used as a source of cellulose (Maheswari et al., 2012). One particular research was done by Al-Ghouti et al. (2010), where agricultural raw date

pits were used as an adsorbent, for example, methylene blue, copper ion, and cadmium were effectively removed. In addition, the adsorption mechanisms in this study proved that not only the physical properties of the adsorbent are considered, but also dispersion forces, electrostatic interaction, and hydrogen bonding should be regarded. In order to describe the adsorption capacity equilibrium, adsorption isotherm models demonstrate the best-fit linear equation (Igwe & Abia, 2007). The different isotherm models for the adsorption process include Langmuir, Freundlich, Dubinin-Radushkevich, and Temkin isotherm models (Al-Ghouti et al., 2019). Several studies investigated the adsorption capacity by using date pits as an adsorbent with isotherm models (Hassan et al., 2020; Al-Ghouti et al., 2019; Aldawsari et al., 2017; Hilal et al., 2012). Moreover, adsorption isotherm is dependent on the type of adsorbed substances, adsorbent, adsorbate, pH, temperature, and ionic strength of adsorbents (Yan et al., 2017). It is worth mentioning that low-cost, nature-based; eco-friendly adsorbents have been gaining attention in the research fields. Generally, the source of such green adsorbents is preferred to be locally available; however, some modification is sometimes needed to meet the required sorption capacity (Pyrzynska et al., 2019). Many researchers such as (Igwegbe et al., 2015; Abdolali et al., 2016; Dutta et al., 2016; Deshmukh et al., 2017) have successfully prepared green adsorbents from plant sources such as grape stalks, coffee grounds, banana peels, and others.

As it has been mentioned, activated carbon is amongst the most relatively expensive adsorbents, therefore, the focus of this research is moving towards low-cost, ecofriendly green adsorbents. The source of these green adsorbents is generally based on locally available resources, which can be modified to enhance sorption capacity (Pyrzynska et al., 2019). Some examples of green adsorbents extracted from plant source include grape stalks (Abdolali et al., 2016), coffee grounds and wheat straw (Dutta et al., 2016),

banana peels (Deshmukh et al., 2017), *Carica papaya* (Igwegbe et al., 2015) and many others. Similarly, cellulose nanocrystals (CNCs) are another type of green adsorbents that have been prepared from cellulose from wood or plant fibers (Bai et al., 2019; Carpenter et al., 2015). As previously mentioned, CNCs have high hydrophilicity, aspect ratio (length/width), specific surface, and variety of functional groups, and these properties may vary from source to source (Oliveira et al., 2019). Hence, due to the high local availability of date pits as agricultural waste, extraction, and reuse of cellulose for environmental, energy storage, and biomedical applications can help to diversify Qatar's economy, thereby, reducing the waste production.

CHAPTER 3: MATERIALS AND METHODOLOGY

3.1 Materials

Deionized distilled water was used in all the experiments to prepare the solutions and suspensions. Qatari date, *Phoenix dactylifera* L. were collected from local stores in Qatar. The hard pit was ground by a microphyte disintegrator. Sodium hydroxide, sodium hypochlorite, n-hexane, and sulfuric acid. Dialysis bags were provided by Carolina Biological Supply Company. 3-formyl-1-methyl pyridinium iodide was the ionic liquid used in the experiments and it solubilized in dimethyl sulphoxide. Li, Mo, B stock solutions were prepared from LiCl, Na₂MoO₄.H₂O, and H₃BO₃, respectively. The pH was adjusted using 1 M HCl and 1 M NaOH.

3.2 Preparation of starting material

The raw date pits (RDP) samples were cleaned with distilled water to remove any dirt and impurities. The samples were left overnight to air dry. Microphyte disintegrator was used to grind the date pits to achieve small fine particles. The particle size range used in all the experiments is 0.125 mm - 0.250 mm. The samples were stored at room temperature for future use.

3.3 Extraction of cellulose from date pits

Figure 3 shows the schematic illustration summarizing the used extraction methods for cellulose nanocrystals (CNC) from raw date pits (RDP).

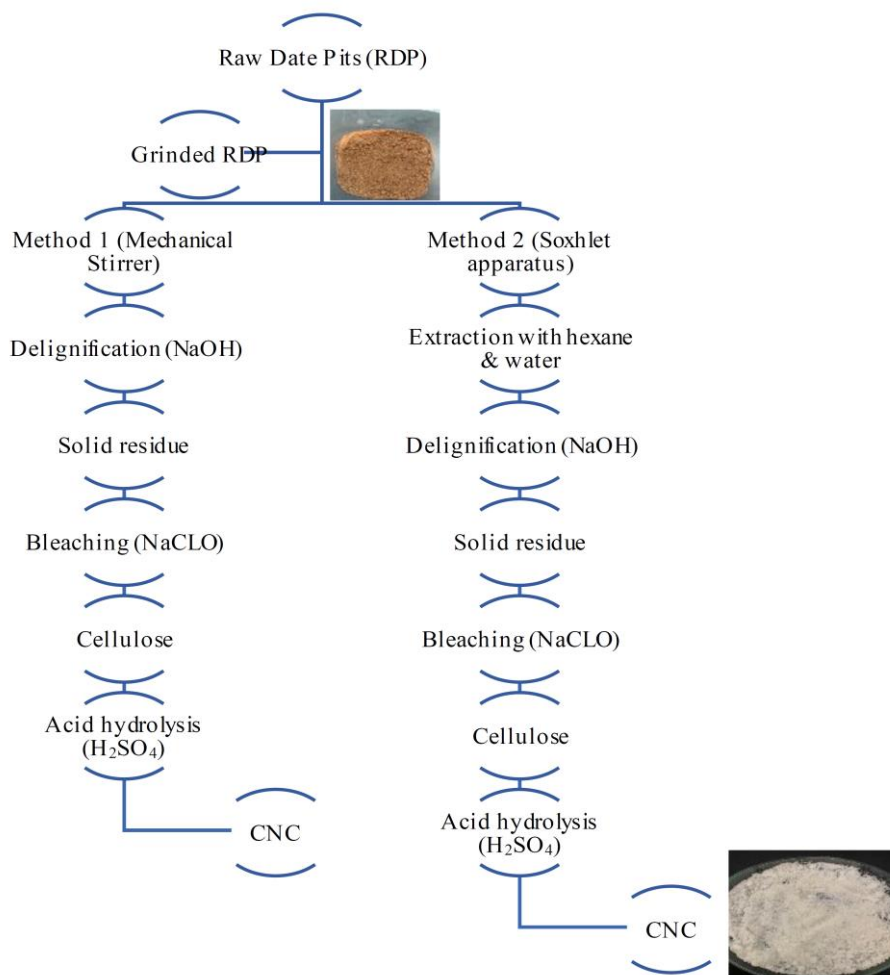


Figure 3. Schematic illustration summarizing the used extraction methods for cellulose nanocrystals (CNC) from raw date pits (RDP).

3.4 Method 1-Mechanical stirrer

Five hundred milliliters of 6.0 % sodium hydroxide (NaOH) were prepared in an Erlenmeyer flask with 50 g of ground date pits to delignify the samples. This mixture was heated at 70°C and stirred for 4 hrs using the mechanical stirrer. The black lignin waste was filtered off and the solid part undergone constant washing with distilled water to achieve neutral pH. The mixture was left to air dry overnight and the product attained after the NaOH treatment is denoted as N₁-DP. Furthermore, the neutralized mixture

was undergone bleaching by the addition of 300 mL of 6.0% sodium hypochlorite solution (NaClO). The mixture was stirred for 2 hrs at 70°C using the mechanical stirrer and the solid part was filtered off from the liquid. Then, the product was further bleached six times, consecutively, before washing the product exhaustively with distilled water to afford neutral cellulose. After that, it was separated by filtration, and the obtained solid product was cellulose. Finally, the pure cellulose was left to air dry overnight for further use and the product attained after the NaClO treatment is denoted as B₁-DP.

3.5 Method 2-Soxhlet apparatus

In this method, 50 g of ground date pits were dewaxed in a Soxhlet apparatus using 500 mL of 96% n-hexane in several cycles for 8 hrs. The black concentrated hexane extract of this step was left to evaporate under reduced pressure. Then, it was followed by further washing by 500 mL of distilled water for 8 hrs in several cycles in the Soxhlet extractor. Afterward, the dewaxed fibers of the date pits were left to air-dry overnight. To delignify the date pits, 500 mL of 2.0% sodium hydroxide (NaOH) were added in the Soxhlet extractor with the dewaxed date pits for the alkaline extraction step for 3 hrs. The product was then consecutively washed with distilled water to afford neutral delignified cellulose and was left to air dry overnight and the product is denoted as N₂-DP. The final step is bleaching by 1.7% of NaClO in the Soxhlet extractor for 3 hrs. The solid product was washed with distilled water to afford neutral cellulose and was left to air dry overnight and the product is denoted as B₂-DP.

3.6 Preparation of cellulose nanocrystals (CNCs)

The purified cellulose of both methods (1 & 2) was subjected to the treatment with 500 mL of 64% sulfuric acid (H₂SO₄) for 1 hr under 25°C. The reaction ended by adding cold distilled water that is 10 times the volume of the reaction. Then, sulfuric acid was washed repeatedly by distilled water until neutral pH was achieved. After that, the

CNCs were separated by centrifuging the sample at 5,000 rpm for 0.5 hr. Finally, CNCs were soaked in pure distilled water by using a dialysis membrane for 48 hrs to remove excess sulfate ions. Lastly, the dialyzed suspension of the CNCs was dispersed by ultrasonication at 600 w for 15 mins. The obtained CNCs were dried using an oven at 70°C overnight. The CNCs obtained by method 1 will be denoted as CNC₁ and by method 2 as CNC₂.

3.7 Characterization of the prepared CNC and Intermediate Products

3.7.1 Chemical composition measurement of the lignocellulosic materials of the raw date pits (RDP)

The chemically-treated RDP was analyzed by a standard (TAPPI) for the chemical composition of each intermediate product of each method (N₁-DP, B₁-DP, N₂-DP, B₂-DP). Two samples from each method were tested and the average values were obtained in the end. The holocellulose content, which comprises cellulose and hemicellulose, was performed as mentioned by standard (TAPPI T19m-54). To determine the α -cellulose content, treatment by NaOH of the fiber was done to remove the hemicellulose. Furthermore, the difference between the holocellulose and α -cellulose values gives the hemicellulose content. Lastly, the lignin content was also analyzed by using sulfuric acid (TAPPI-T222 cm-99). The obtained values are then compared to the original content of RDP as mentioned by Al-Ghouti et al., (2019).

3.7.2 Determination of physical properties of the isolated CNCs from method 1 & 2

True density, moisture content, and pH were determined for CNCs from both methodologies. The true density was analyzed by using the liquid displacement method that has been previously described by Abu-Thabit et al. (2020). Immersion liquid xylene was used, and the true density (D_T) was calculated by the equation (1):

$$D_T = \frac{w}{[(a+w)-b]} \times SG \quad (1)$$

Where w is the mass of the CNC sample, SG is the specific gravity of xylene, a is the total mass of the (pycnometer bottle + solution), and b is the sum of the mass of the (pycnometer bottle + solution + sample). The results were based on two duplicates and their average is reported. The experiment was done for both methodologies. Furthermore, moisture content was analyzed following the procedure of Tarchoun et al., (2019). The moisture content (MC) was calculated as per equation (2).

$$MC (\%) = \left[\frac{w_i - w_f}{w_i} \right] \times 100 \quad (2)$$

Where w_i is before drying the sample and w_f is after drying the samples. The results were based on two duplicates and their average is reported. The experiment was done for both methodologies. Lastly, the pH was determined relying on the method by Kambli et al., (2017). The CNC sample was immersed in 500 ml of distilled water. Then the suspension was placed on the shaker for 30 min at 25°C. A portable digital pH meter (Model: ST 300 OHAUS) was used to determine the suspension pH for both methodologies.

3.7.3 Characterization adsorbents (IL-CNC@DP & RDP), CNC, & intermediate products

Generally, in any adsorption system, the adsorbent's characterization offers the necessary knowledge of the involved process and the mechanisms. Consequently, the characteristics of the adsorbents (IL-CNC@DP & RDP) were determined prior to the adsorption process. Therefore, a scanning electron microscope (SEM) was used to evaluate the morphological characteristics of the adsorbent's surface using the JEOL model JSM-6390LV. Fourier transform infrared (FTIR) spectra were recorded using the R Spirit-T model. The FTIR analysis was conducted to interpret the functional groups present in the adsorbents. The FTIR measurements were performed over 4000–500 cm^{-1} . Moreover, adsorbent samples were removed from the solution to further

characterize using FTIR & SEM. Furthermore, transmission electron microscopy (TEM) was used to determine the size distributions of the two adsorbents in which they were imaged using an H-7650 Hitachi. Furthermore, the surface areas of the prepared materials were characterized using the Brunauer, Emmett, and Teller (BET) equation (Aim Sizer-AM301). The results were obtained by nitrogen adsorption measurements that are made at liquid nitrogen temperature, 77 K.

FTIR, SEM, TEM of CNC₁ & CNC₂ were also analyzed to study if there are any significant differences between the two methods. Moreover, X-ray diffraction (XRD) analysis was performed on CNC₁ & CNC₂ of the chemically treated cellulose fibers using a diffractometer. The diffraction intensities were recorded between 5° and 60° (2θ angle range) at a scan rate of 5°/min. The crystallinity index (CrI, %) was measured according to using the Segal method (Aguayo et al., 2018). The equation of the crystallinity index was calculated as per equation (3).

$$CrI = \left[\frac{I_{200} - I_{am}}{I_{200}} \right] \times 100 \quad (3)$$

Where I_{200} is the maximum intensity of the diffraction at peak of 200 ($2\theta = 22.6^\circ$) and I_{am} is the intensity of the diffraction at $2\theta = 18^\circ$.

Lastly, the intermediate products (N₁-DP, B₁-DP, N₂-DP, B₂-DP) were solely studied by SEM for further characterization.

3.8 Preparation of ionic liquid-nanocellulose composite (IL-CNC)

In order to modify the RDP, the IL-CNC composite was used by using the IL and the already isolated CNC. Ionic liquid (3-formyl-1-methyl pyridinium iodide) was obtained from the Department of Chemistry at Qatar University and solubilized in DMSO (dimethyl sulphoxide) at 65°C with constant mixing until the solution is homogenized. Then, the already extracted CNC are added to the mixture and left for an hour to allow time for the IL and CNC to bind and form a composite. A 1:1 ratio was used for IL and

CNC.

3.9 Functionalization of raw date pits (RDP) with the prepared IL-CNC

The IL-CNC composite that was prepared is used to functionalize and improve the sorption capacity of date pits. Therefore, 5 g of ground raw date pit powder was mixed with the suspension of the prepared IL-CNC. Until homogenization is achieved, the resultant IL-CNC@DP is dried in the oven for few hours at 60°C. The newly prepared adsorbent will be characterized to investigate the effect of composites on RDP characteristics.

3.10 Preparation of Li⁺, Mo⁶⁺, & B³⁺ stock solution

A lithium stock of 100 ppm was prepared by adding 0.611 g of LiCl in a 1 L volumetric flask, then adding distilled water until the mark slowly while making sure the compound is completely solubilized. As for the molybdenum stock solution of 100 ppm, it was prepared by adding 0.252 g of Na₂MoO₄.H₂O in a 1 L volumetric flask. Finally, the last stock was prepared by adding 0.572 g of H₃BO₃ in a 1 L volumetric flask to obtain a boron stock solution of 100 ppm.

3.11 Batch adsorption of Li⁺, Mo⁶⁺, & B³⁺

Different parameters were investigated under 5 pH values (2, 4, 6, 8, and 10), 10 initial concentrations of B³⁺, Li⁺, and Mo⁶⁺ (5, 10, 15, 20, 25, 30, 35, 50, 70, and 100 ppm), & three temperatures (25, 35 and 45 °C). The adsorptive batch studies were conducted in 100 mL glass bottles where 0.05 g of the required adsorbent is added to 50 mL of the appropriate initial concentrations making sure the ratio of the adsorbent mass and the volume of the solution are 1:1 (g/mL). The bottle samples were capped and placed in the shaker for 24 h at 165 rpm. To study the pH of the adsorption system, the adjustment to its appropriate value will be done by adding 1 M NaOH or 1 M HCl. Moreover, the effect of different concentrations was prepared by dilutions with the best pH chosen, and then samples are placed in a shaker for 24 h at 25 °C at 165 rpm. Finally, the last

parameter investigates the effect of temperature on the adsorption process. Several concentrations of (Li^+ , Mo^{6+} , & B^{3+}) were also prepared; however, the samples are subjected to different temperatures at 35 °C and 45 °C in the shaker incubator for 24 h day at 165 rpm. After each test, the spent adsorbents were filtered through a 0.2 μm syringe filter and were air-dried for further analysis using SEM & FTIR. Duplicates and blanks were used in each experiment.

The initial and equilibrium Li^+ , Mo^{6+} , & B^{3+} concentrations were analyzed by using ICP-OES (an IRIS Intrepid by ThermoFisher Scientific). The percentage of solute removal according to Anantha et al. (2020) was calculated as per equation (4).

$$\text{Removal (\%)} = \left[\frac{C_0 - C_e}{C_0} \right] \times 100 \quad (4)$$

Where C_0 and C_e are the initial and equilibrium solute concentrations (mg/L), respectively.

Moreover, adsorption capacity was calculated as per equation (5).

$$qe = [C_0 - C_e] X \frac{V}{M} \quad (5)$$

Where C_0 and C_e are the initial and equilibrium solute concentrations (mg/L), respectively, V is the volume (L), and M is the weight of the adsorbent (g).

3.12 Adsorption isotherms of Li^+ , Mo^{6+} , & B^{3+}

Four isotherm models were used in this study to determine the best-fit model for the adsorption process: Langmuir, Freundlich, Dubinin– Radushkevich, and Temkin isotherm models. Table 6 presents the linear forms of the four adsorption isotherm models, in addition to their constants and adsorption parameters (Al-Ghouti & Da'ana, 2020; Zango et al., 2020).

Table 6. Isotherm models used in this study.

Model	Equation	Parameters
Langmuir adsorption isotherm	$\frac{C_e}{q_e}$ $= \frac{1}{b \cdot Q_0} + \frac{C_e}{Q_0}$	<p>-q_e is the amount of adsorbate in the adsorbent measured at equilibrium (mg/g) or the amount of metal adsorbed per gram of adsorption.</p> <p>-Q_0 is the maximum monolayer adsorption capacity (mg/g).</p> <p>-b is the Langmuir isotherm constant (L/mg).</p> <p>-C_e is the equilibrium concentration of adsorbate (mg/L).</p> <p>The favorability of Li, Mo, B adsorption on the adsorbents based on the Langmuir isotherm is represented by the following equation:</p> $RL = \frac{1}{1 + b \cdot (C_e)}$ <p>Where R_L describes the probability of the adsorption process. If $R_L > 1$, then the adsorption process would be unfavorable, and if $0 < R_L < 1$ then this corresponds to an energetically favorable adsorption process. Lastly, if $R_L = 0$ the adsorption process can be irreversible.</p>
Freundlich adsorption isotherm	$\ln q_e = \ln K_F + \frac{1}{n} \ln C_e$	<p>-q_e is the amount of adsorbate in the adsorbent measured at equilibrium (mg/g) or the amount of metal adsorbed per gram of adsorption.</p> <p>-K_F is the Freundlich adsorption constant (mg/g).</p> <p>-C_e is the equilibrium concentration of adsorbate (mg/L).</p> <p>-n corresponds to the type of isotherm. If $\frac{1}{n}$ is greater than zero and less than 1</p> <p>If $\frac{1}{n} > 1$, then the adsorption process would be unfavorable and if $0 < \frac{1}{n} < 1$ then this corresponds to an energetically favorable adsorption process. Lastly, if $\frac{1}{n} = 1$ the adsorption process can be irreversible.</p>
Dubinin–Radushkevich adsorption isotherm	$q_e = q_s \cdot (-B_D [R. T. \ln (1 + \frac{1}{C_e})]^2)$	<p>-q_e is the amount of adsorbate in the adsorbent measured at equilibrium (mg/g) or the amount of metal adsorbed per gram of adsorption.</p> <p>-q_s is the theoretical isotherm saturation capacity (mg/g).</p> <p>- B_D is the adsorption energy constant ($\text{mol}^2 / \text{kJ}^2$).</p>
Temkin Adsorption Isotherm	$q_e = B \cdot \ln A_T + B \cdot \ln C_e$	<p>-q_e is the amount of adsorbate in the adsorbent measured at equilibrium (mg/g) or the amount of metal adsorbed per gram of adsorption.</p> <p>-C_e is the equilibrium concentration of adsorbate (mg/L).</p> <p>-A_T Temkin Adsorption Isotherm equilibrium binding constant (L/g).</p> <p>- B is the constant that is related to the heat of adsorption (J/mol). B can be calculated by</p>

$$B = \frac{RT}{bT}$$

Where R is the universal gas constant (8.314J/mol K), T is the absolute temperature (K), b_T is the Temkin isotherm constant.

3.13 Thermodynamic studies of Li^+ , Mo^{6+} , & B^{3+} adsorption

Thermodynamic studies are very important for any adsorption process since they determine the spontaneity of the adsorption mechanism. One important measure of spontaneity is determined by Gibb's free energy change (ΔG°). The spontaneous reaction occurs if ΔG° , at a specific temperature, possesses a negative value. The changes in enthalpy (ΔH°) and the changes in entropy (ΔS°) are also two important thermodynamic measures. The three thermodynamic parameters (ΔG° , ΔH° , and ΔS°) were calculated according to Al-Ghouti & Al-Absi (2020), as per equations (6) and (7).

$$\Delta G^\circ = -RT \ln K_L \quad (6)$$

Where R is the universal constant 8.314 J/mol.K, T corresponds to the temperature measured in Kelvin, and K_L represents the Langmuir isotherm constant. Temperature is used to express the standard enthalpy and entropy changes of adsorption.

$$\ln K_L = -\frac{\Delta H^\circ}{RT} + \frac{\Delta S^\circ}{R} \quad (7)$$

Where ΔH° and ΔS° are determined from the slope and intercept of the equation of the line that is evaluated from the plot of $\ln K_L$ Vs. $1/T$.

3.14 Desorption studies of Li^+ , Mo^{6+} , & B^{3+}

This study was analyzed by using a total of 0.05 g of spent IL-CNC@DP & RDP of all initial concentrations. The spent adsorbents were tested under two different solutions:

0.5 M HCl, and 1 M HCl. A total volume of 50 mL of each solution was used in 100 mL glass bottles. The mixture was then shaken with the required adsorbent for 24 h at 165 rpm. The spent adsorbents are filtered through a 0.2 µm syringe filter and the solution is analyzed by ICP-OES (an IRIS Intrepid by ThermoFisher Scientific). Duplicates and blanks were used in each experiment. The desorption percentage was calculated according to equation (8) according to Al-Ghouti & Al-Absi (2020).

$$\text{Desorption (\%)} = \left[\frac{C_0 - C_e}{C_0} \right] \times 100 \quad (8)$$

Where C_0 and C_e are the average adsorption and desorption concentration (mg/L), respectively.

3.15 Statistical analysis

In this study, since the experimental design of the experiments was completely random then a completely randomized design (CRD) and factorial tests are conducted. Analysis of variance (ANOVA) for two factors with replication by using Microsoft excel. Moreover, a single factor was used for the desorption study test.

3.16 Application of RDP and IL-CNC@RDP to a real groundwater sample

Groundwater obtained from the north wells after a rainy season in May 2019 was used to study the effectiveness and selectivity of the adsorbents. 50 mL of groundwater were added to glass bottles containing 0.05 g of each adsorbent. They were placed on a shaker for 24 h at 165 rpm. The spent adsorbents are filtered through a 0.2 µm syringe filter and the solution is tested for the selectivity of metals towards the adsorbent by ICP-OES. Another sample of groundwater was analyzed for multi-element analysis without the addition of any adsorbents. Duplicates and blanks were used in each experiment.

CHAPTER 4: RESULTS AND DISCUSSION

4.1 Characterization

4.1.1 Chemical Components

Table 7 demonstrates the chemical compositions of N₁-DP, B₁-DP, N₂-DP, B₂-DP, and RDP (Al-Ghouti et al., 2019). The chemical compositions of the intermediate products of the two methods were found to be significantly different.

Table 7. Chemical composition of cellulose nanocrystals from different sources. *N₁DP & N₂DP (treated by NaOH), B₁DP & B₂DP (after bleaching).

Sample	% α -Cellulose	% Hemicellulose	% Lignin	Reference
RDP				
Raw	21.2	28.1	19.9	
Alkali treated (N ₁ DP)*	63.1	7.95	7.02	
Alkali treated (N ₂ DP)	51.5	6.7	3.21	This study
Bleached (B ₁ DP)	84	2.6	0.51	
Bleached (B ₂ DP)	72.5	1.5	0.14	
Mengkuang leaves				
Raw	37.3	34.4	24	
Alkali treated	56.5	15.5	22.6	Sheltami et al., 2012
Bleached	81.6	15.9	0.8	
Rice husk				
Raw	35	33	23	
Alkali treated	57	12	21	Johar et al., 2012
Bleached	96	-	-	
Banana (pseudostem)				
Raw	69.9	19.6	5.7	Abraham et al., 2011
Bleached	96.8	0.2	0.2	
Pineapple leaf				
Raw	75.3	13.3	9.8	Abraham et al., 2011
Bleached	97.3	0.2	-	
Jute (stem)				
Raw	68.3	15.4	10.7	Abraham et al., 2011
Bleached	97.3	-	-	
Soy hulls				
Raw	48.2	24.0	5.78	Flauzino Neto et al., 2013
Bleached	84.6	11.2	3.7	
Tea leaf waste fiber				
Raw	16.2	68.2	18.8	Abdul Rahman et al., 2017
Alkaline treated	58.8	22.2	5.5	
Bleached	87.9	8.1	1.8	
Borer powder of bamboo				
Raw	35.7	30.4	27.3	Hu et al., 2014
Bleached	37.5	27.8	27.9	

Oil palm trunk				
Raw	50.74	77.39	11.68	Lamaming et al., 2015
Hot water treated	51.75	81.36	13.19	
Sweet potato residue				
Raw	83.57	12.81	2.27	Lu et al., 2013
Alkaline treated	94.85	3.98	0.76	
Rice husk				
Raw	33.8	17.1	21.5	Collazo-Bigliardi et al., 2018
Alkali treated	55.9	15.8	19.9	
Bleached	73.8	19.2	1.6	
Coffee husk				
Raw	35.4	18.2	23.2	Collazo-Bigliardi et al., 2018
Alkaline treated	52.6	19.0	20.4	
Bleached	61.8	27.2	2.6	

The results of the chemical compositions of the RDP at different treatment stages of methods 1 & 2 are listed in Table 7. The RDP has a chemical composition of 21.2, 28.1, and 19.9% for α -cellulose, hemicellulose, and lignin, respectively (Al-Ghouti et al., 2019). The non-cellulosic content like hemicellulose has the highest percentages in comparison to the cellulose content. Therefore, the main objective is to chemically treat the RDP in order to remove the non-cellulosic contents. Hence, when the RDP were subjected to treatment by NaOH, the hemicellulose and lignin contents of the RDP decreased from 28.1% and 19.9% to 7.95% and 6.7%, respectively for both methods (N₁-DP & N₂-DP). On the other hand, the concentration of cellulose increased for both methods (N₁-DP & N₂-DP) to 63.1% and 51.5%, respectively. Comparing these values to the original α -cellulose of the RDP, which is 21.2%, the values are significantly high. Hence, the delignification process performed by the NaOH treatment was successful. Furthermore, it can be concluded that method 1 yields better results than method 2, in terms of chemical composition after the delignification process.

After the bleaching treatment, the hemicellulose and lignin contents decreased even

more to 2.6% and 1.5%, respectively for both methods (B₁.DP & B₂.DP). Abu-Thabit et al. (2020) isolated and characterized microcrystalline cellulose from *Phoenix dactylifera* L. date seeds and found that bleached date seeds have 3.92% hemicellulose and 0.86% lignin. Moreover, it can be justified that the bleaching treatment is the second treatment for the RDP, therefore less hemicellulose and lignin contents are yielded. Whereas it is evident that the cellulose content for both methods (B₁.DP & B₂.DP) increased significantly to 84% and 72.5%, respectively. This can be attributed to the elimination of the amorphous phase that was characterized by the water-soluble hemicellulose and alkali-soluble lignin components, which in turn led to the presence of higher cellulose content (Tarchoun et al., 2019). It is clear that the first method that relies on the mechanical stirrer yields better results for purified cellulose.

4.1.2 Physicochemical properties of CNC₁ & CNC₂

CNC₁ & CNC₂ properties are listed in Table 8. Measurement of true density of cellulosic materials is important since it provides the required physical quantity value needed for future practical uses. The density of CNC₁ (1.7) and CNC₂ (1.9) are considered to be very close in value to each other. In addition, comparing these results to previous studies, the true density of nanocellulose was found to be almost 1.60 g/mL regardless of the cellulose biological origin (Daicho et al., 2019). This means that most nano-scale products have true densities that are less than 2.0 g/mL irrespective of the chemical composition and other physicochemical properties the fiber possesses. According to Crouter & Briens, (2014), the moisture content is considered a significant parameter when dealing with CNC at pilot scales such as manufacturing stages. In the current study, the measured moisture content of CNC₁ is 5.6% and CNC₂ 6.2%. It can also be concluded that method 2 tends to retain more moisture in the samples due to the extraction step performed with hexane & water. Lastly, the pH value for the CNC₁

suspension (6.4) and that of CNC₂ (6.2) are close to neutral, which fulfills the aim of obtaining pure cellulose nanocrystals after modifying by sulfuric acid.

Table 8. Physicochemical properties of isolated CNCs.

Physicochemical property	CNC ₁	CNC ₂
True density	1.7	1.9
Moisture content (%)	5.6	6.2
pH	6.5	6.2

4.1.3 Scanning electron microscopy (SEM) analysis

The RDP, N₁-DP, B₁-DP, N₂-DP, B₂-DP, CNC₁ & CNC₂ are shown in Figure 4.A-J below. The SEM images of RDP demonstrate that the sample has agglomerated and smooth surface morphology with few rough areas, which is due to the occurrence of hemicellulose and cellulose content that compacts and hides the cellulose fibers below them. The high magnification of the surface of the RDP reveals an extremely smooth surface, which can be due to the reflection of the lignin content that coats the cell wall of the RDP. Comparing this to the intermediate products of both methods (N₁-DP, N₂-DP, B₁-DP, & B₂-DP), it is evident that all the samples exhibit a rough surface with irregular morphologies because of the strong chemical treatments during the delignification and bleaching process. However, after the delignification process by NaOH, it can be inferred that the surface of both N₁-DP & N₂-DP had an irregular structure with a porous exterior. In other words, the filled parts of the surface were removed and that can be obvious from the empty structure due to the removal of the amorphous materials. Similar results were obtained by Zou et al. (2020), who studied

the morphology of transparent cellulose nanofibrils composites and found that the removal of cementing amorphous components led to the presence of hollow surface morphology. This is explained by the fact that the degradation process of the hemicellulose and the lignin content occurred by the alkali treatment (Liu et al., 2018). Further, B₁-DP & B₂-DP exhibited more irregular porous structures, as can be shown in Figures 4e and 5f. The porous morphology of the bleached samples is clear and that is due to the successful removal of hemicellulose and lignin contents. Additionally, this indicates that the removal of the residual lignin by the NaClO solution was successful. All the obtained results are also consistent with the values reported in Table 7. As for the isolated CNC₁ & CNC₂, they have distinct morphologies that are displayed in Figures 4G, and 4I, respectively. It is clearly shown that the acid hydrolysis treatment by sulfuric acid has converted the large porous pieces of cellulose into smaller pieces and fragments with a crystal-like morphology. The resulted CNC of both methods (CNC₁ & CNC₂) possess a porous network with a lamellar structure. Furthermore, at high magnification, both SEM images display cellulose microfibrils with structures that are highly packed due to the strong hydrogen bonding of the intermolecular and intramolecular forces. The crowded structure of the microfibrils is also due to the presence of van der Waals forces (Trache et al., 2017). In the end, it can be inferred that both methods (CNC₁ & CNC₂) have similar morphologies.

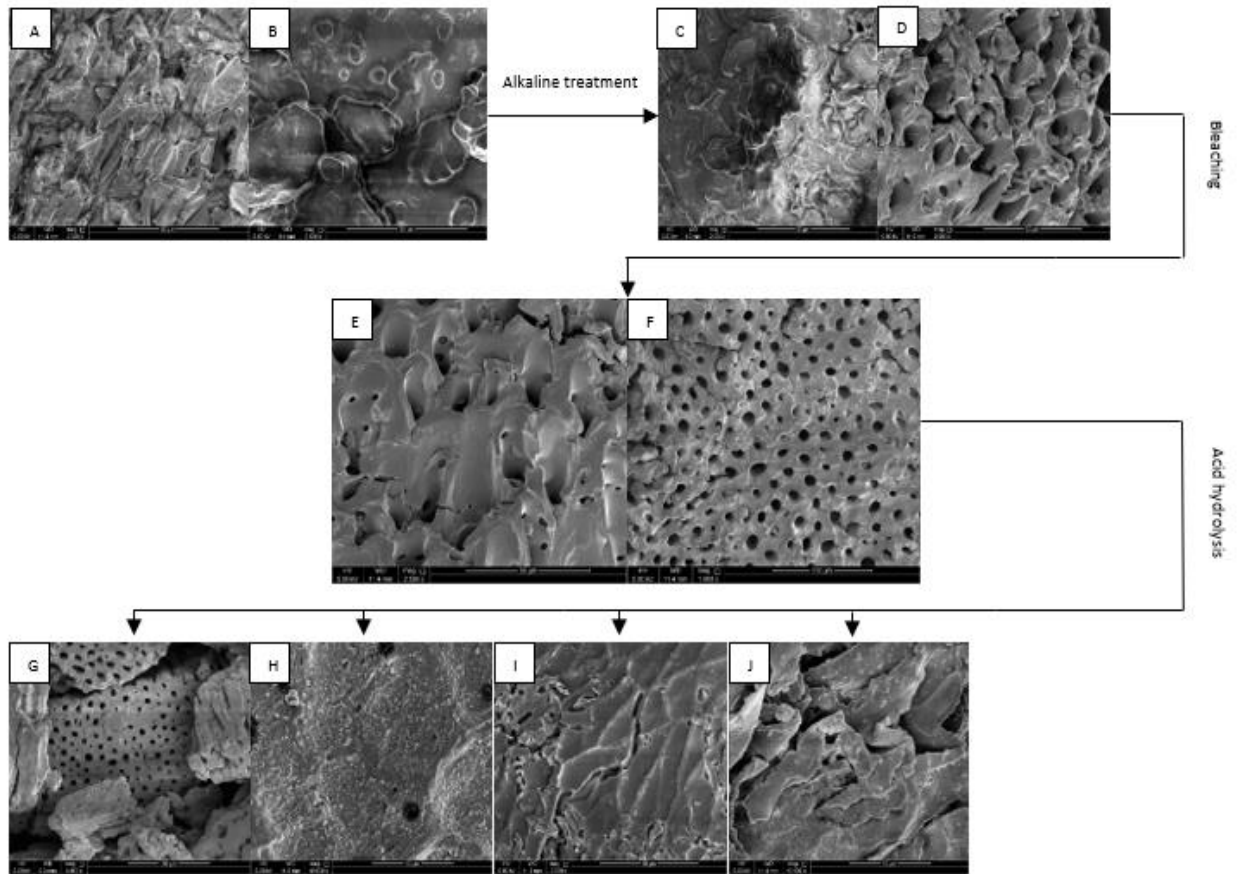


Figure 4. A-J Schematic illustration of SEM surface morphology of A) RDP at 5000x, B) RDP at 2500x, C) N₁_DP, D) N₂_DP, E) B₁_DP, F) B₂_DP, G) CNC₁ at 10,000x, H) CNC₁ at 2500x, I) CNC₂ at 10,000x, J) CNC₂ at 2500x.

Other than studying the SEM images for CNC using different methods of isolation for CNC and its intermediates, we also studied the surface of the unmodified and modified adsorbents that were used in the adsorption study of the metal ions.

Figure 5.A–D shows the modified IL-CNC@DP before and after Li⁺, Mo⁶⁺, & B³⁺ adsorption. The utilization of SEM in this shows that the adsorbent itself before the adsorption process occurs seems to have holes with diverse shapes and sizes. Moreover, these irregular pores or cavities are significant since they indicate that the modified adsorbent has a high surface area. In Figure 5A, the magnification at 500x presents

various cavities onto the whole adsorbent. Furthermore, a closer look at 25,000x demonstrates one cavity that appears to be deep and hollow. Nonetheless, by comparing this modified sample to the unmodified sample (RDP) in Figure 6B, it can be seen that the surface morphology appears to be slightly smoother with fewer pores and cavities. This means that the modified adsorbent's morphology is enhanced and improved after the addition of IL and CNCs onto the DP. After the Li^+ adsorption process in Figure 5B, it can be shown that the pores or cavities are still available even after the increase in temperature to 45°C ; however, they appear to be filled and blocked. This filling could be due to the deposition as aggregates of multi-layer heavy metals. At 25,000x, the surface morphology appears to be densely packed with irregular structures after the adsorption of Li^+ metal ions. As for Mo^{6+} adsorption in Figure 5C, the morphology also looks smoother with fewer pores that are partly filled, shown at 500x. This can imply that the adsorption of Li^+ was better than Mo^{6+} just by looking at their surface morphology. Lastly, in Figure 5D, the surface morphology is different from Li^+ & Mo^{6+} since it demonstrates more pores seen at 500x. Furthermore, on a more magnified scale such as 5,000x, the pores seem to be packed to some extent due to the adsorption of B^{3+} metal ions. It is also important to note that the SEM images of Li^+ , Mo^{6+} , and B^{3+} after adsorption were taken under the same experimental conditions, therefore the assumption that Li^+ adsorption onto the modified IL-CNC@DP is more favorable than Mo^{6+} & B^{3+} can be justified. This result is consistent with the data obtained regarding their adsorption capacities in section 4.4. It is worth mentioning that a momentous finding was found in the SEM image of Figure 5.C that can be shown up close at 25,000x, which are the cellulose fibers. Other fibers are also scattered on the surface of the adsorbent; hence, this implies that modification did in fact occur on the DP surface. For example, modified date pits by activated carbon intended for the adsorption of

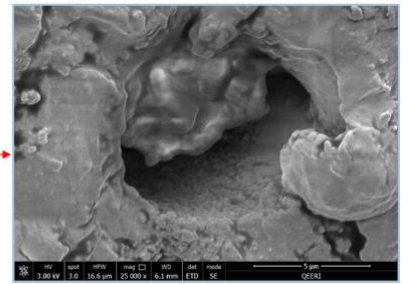
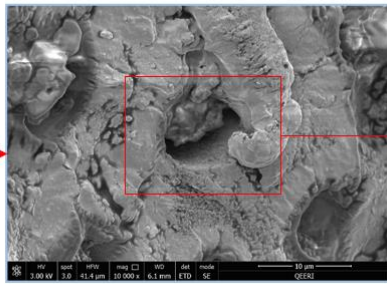
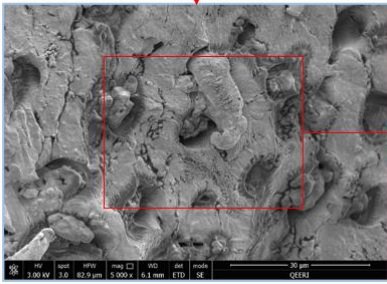
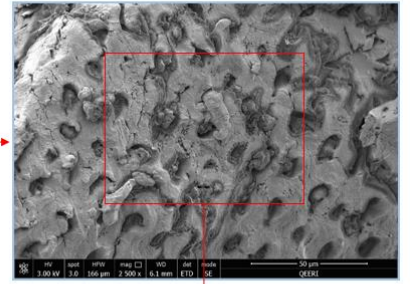
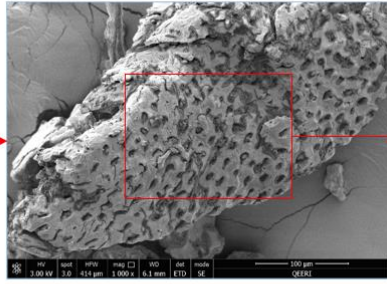
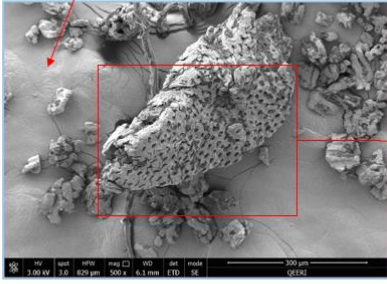
heavy metals like Cd(II), Cu(II), Pb(II), and Zn(II) also presents morphological changes with deposited aggregates providing multi-layer adsorption of heavy metals onto the adsorbent's surface (Aldawsari et al., 2017).

Figures 6.A–D show the scanning electron microscopy (SEM) of the unmodified RDP before and after Li^{1+} , Mo^{6+} , and B^{3+} adsorption. In Figure 6A, the RDP structure presents a smoother morphology with no holes implying that the surface area is not yet modified and improved. Furthermore, the surface has agglomerates that are found as clusters on top of each other, shown at 5000x, whereas by looking closely at the larger magnification at 25,000x, the clusters are less presenting an even surface morphology. After Li^{1+} adsorption onto the RDP, the surface becomes more cracked and dented. At 2,500x magnification, the surface appears to have holes that are elongated in shape suggesting how the adsorption process of Li^{1+} altered the physical appearance of the adsorbent, in Figure 6B. Additionally, the dark areas of the elongated dents are probably due to the increase of temperature to 45°C . This can also be shown after the adsorption of Mo^{6+} , where there are cracks and dents on the surface with agglomeration that appear to be semi-spherical, in Figure 6C. Lastly, in Figure 6D, the images are similar to the adsorption of Mo^{6+} , where multiple surface agglomeration occurred after the adsorption of B^{3+} . The SEM figures of RDP are also found in previous studies where the surface morphology is almost similar to our results that were obtained (Fakhfakh et al., 2019; Mathew et al., 2018). Moreover, the study by Al-Ghouti and others (2019) showed how the SEM image of the roasted date pits presented more pores and holes upon modification by roasting the date pits at 130°C for 3 hours. In this case, no modification or alteration occurred on the date pits. In other words, the sample used in this study is not modified to enhance the surface area of the adsorbent in order to reveal more adsorption sites. Hence, these results are confirmed by the BET analysis since the

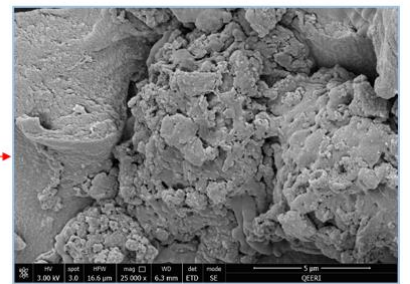
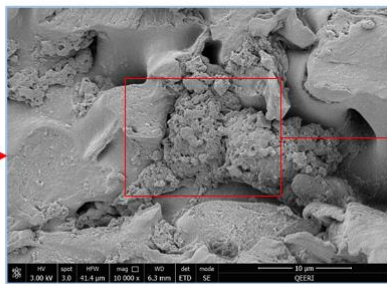
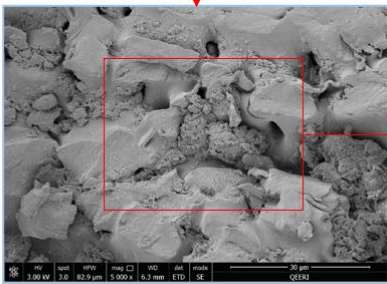
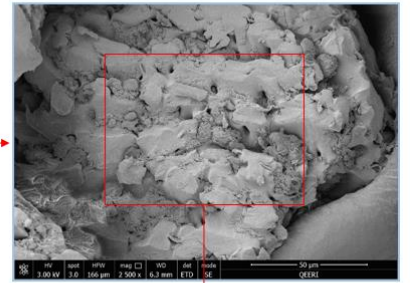
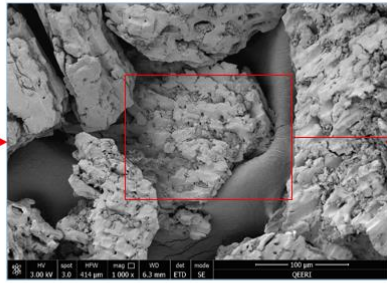
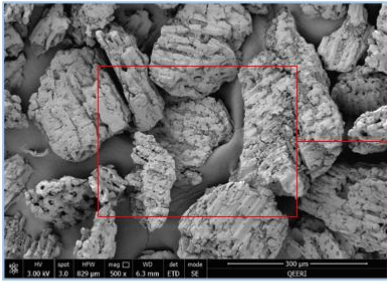
specific surface area of the RDP was found to be 2.126 m²/g, where the modified form of the RDP has a specific surface area of 4.254 m²/g.

Carbon Tape

A



B



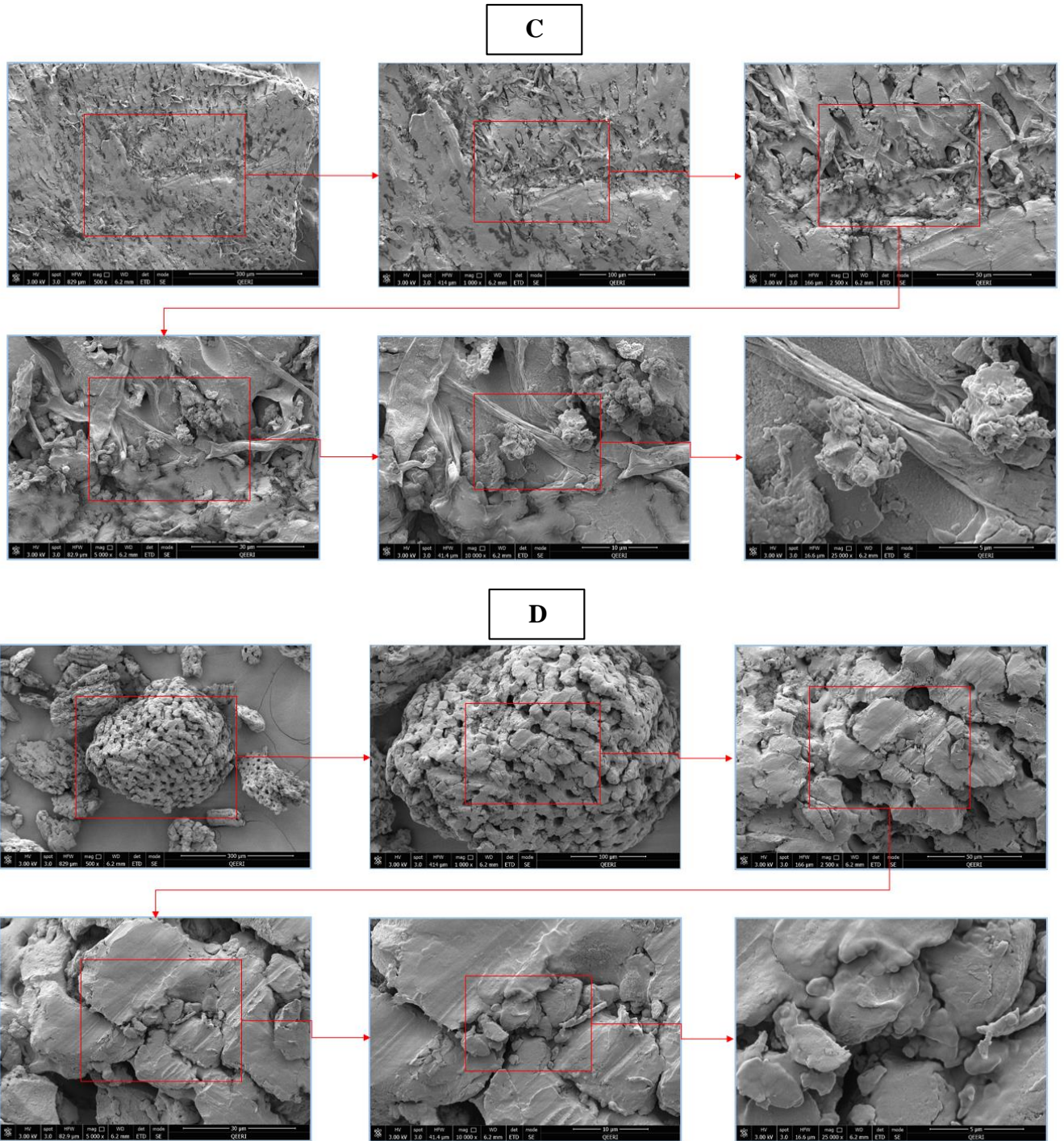
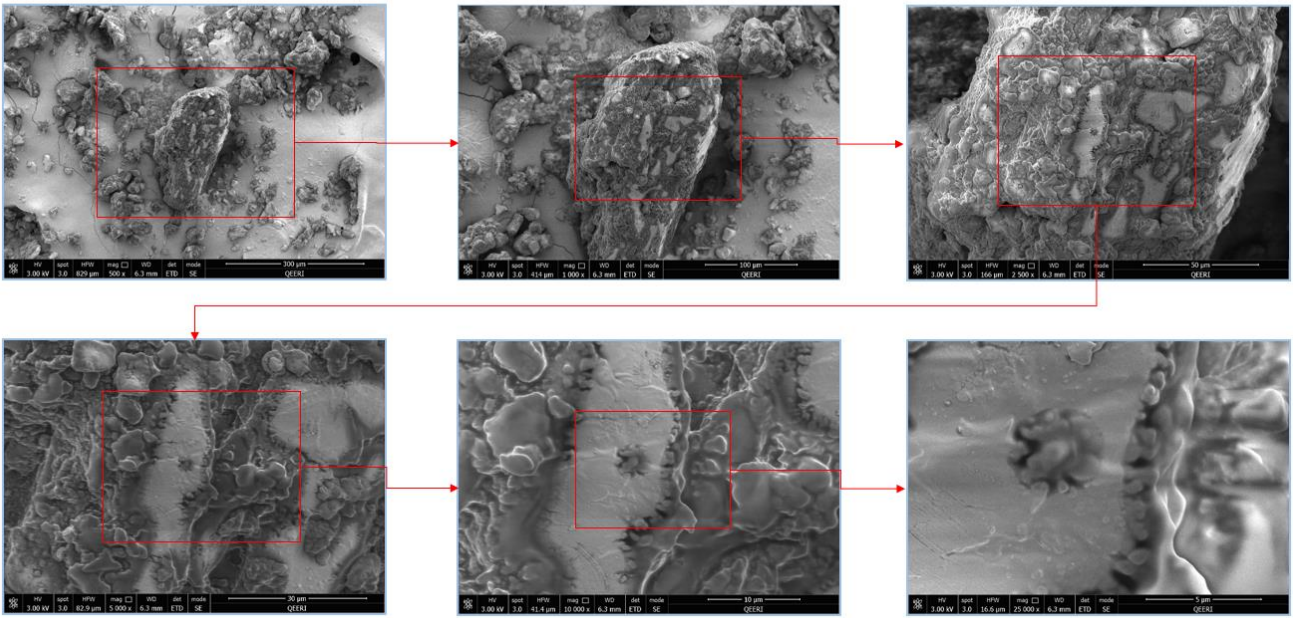
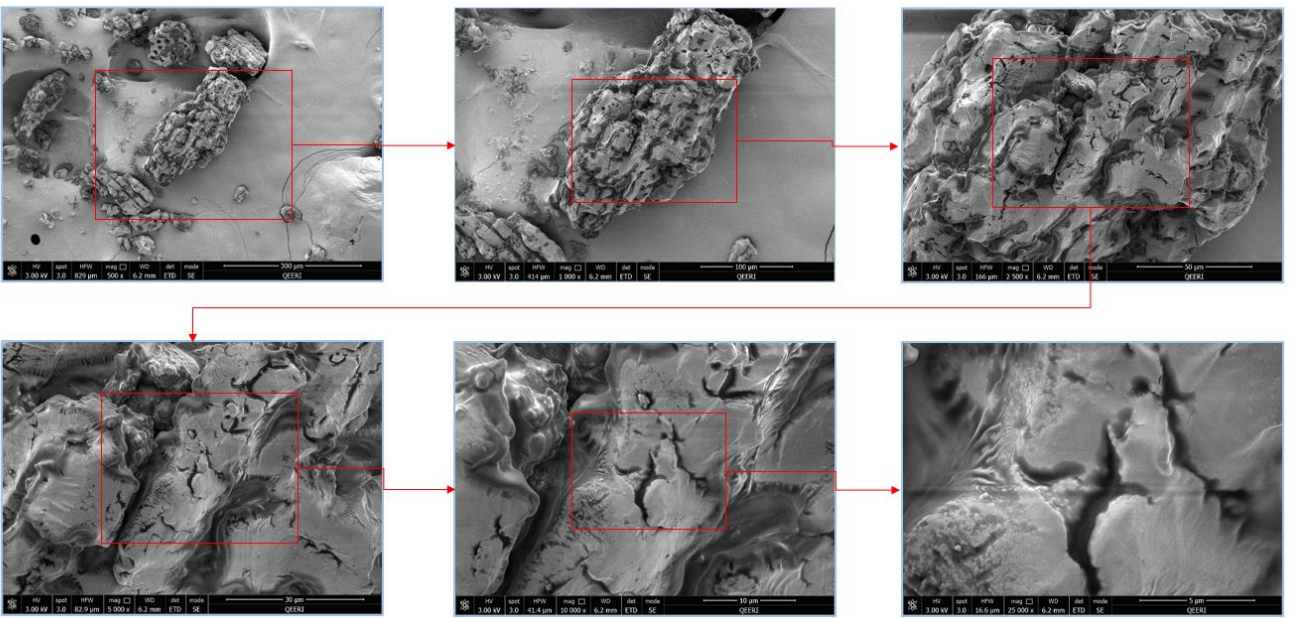


Figure 5. SEM images of the IL-CNC@DP before and after adsorption. (A) Before the treatment under 25 °C. (B) After Li^+ adsorption at 100 ppm with pH 6 under 45 °C. (C) After Mo^{6+} adsorption at 100 ppm with pH 6 under 45 °C. (D) After B^{3+} adsorption at 100 ppm with pH 6 under 45 °C.

A



B



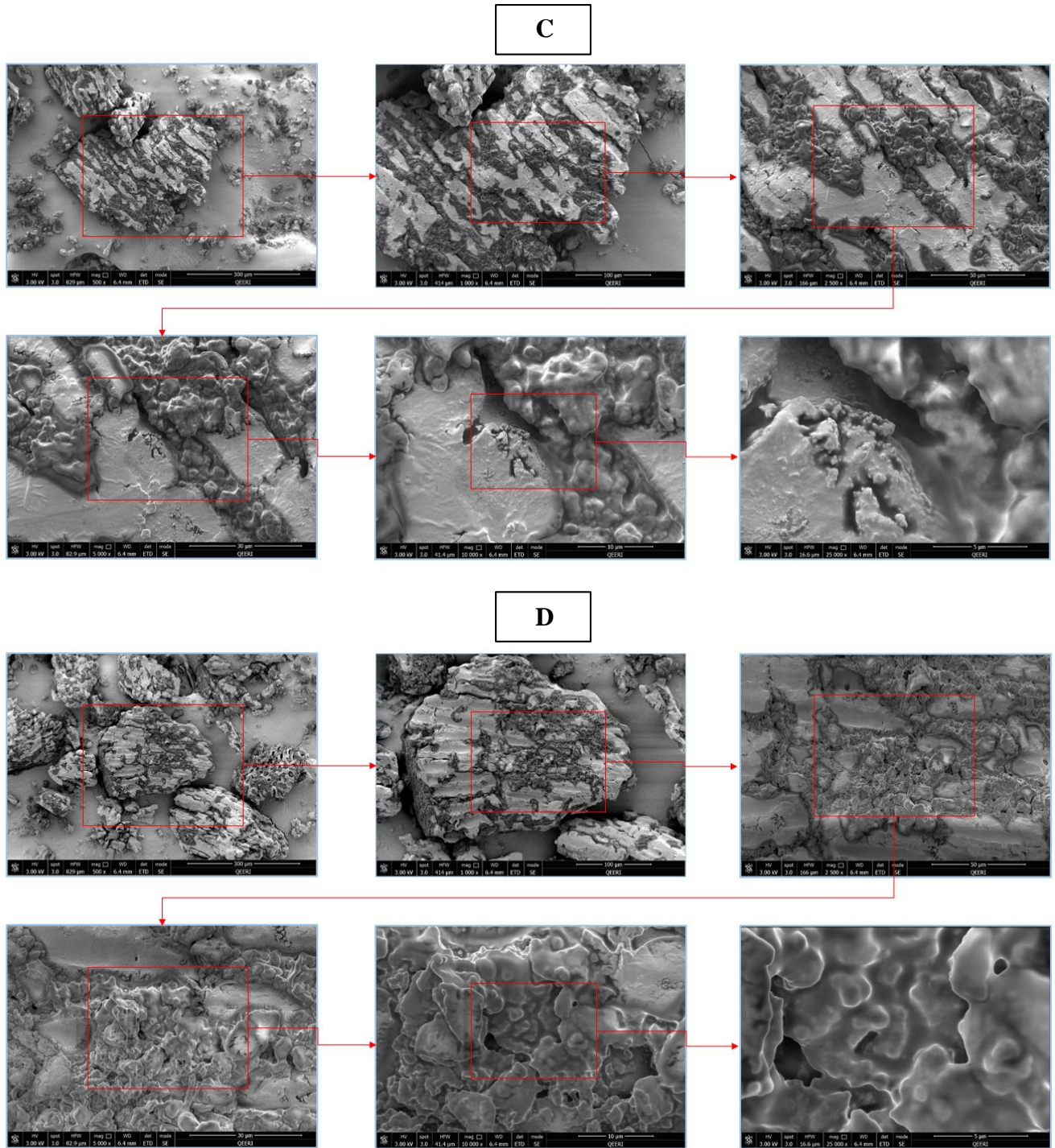


Figure 6. SEM images of the RDP before and after adsorption. (A) Before the treatment under 25 °C. (B) After Li^+ adsorption at 100 ppm with pH 6 under 45 °C. (C) After Mo^{6+} adsorption at 100 ppm with pH 6 under 45 °C. (D) After B^{3+} adsorption at 100 ppm with pH 6 under 45 °C.

4.1.4 Transmission electron microscopy (TEM) analysis

The transmission electron microscope was used to study and observe the morphology of the cellulose nanocrystals in two different methods. The arrangement of the cellulose nanocrystals extracted after acid hydrolysis of bleached RDP is shown in Figure 7 of both CNC₁ & CNC₂. The TEM was the best to study the cellulose at the nanoscale. Based on literature and previous studies, the usage of sulfuric acid at optimum concentration, temperature, and time yields ideal nanocrystals (Khan et al., 2020; Guo et al., 2020; Zheng et al., 2019). The TEM results for the CNC₁ morphology after modification through sulfuric acid hydrolysis reveal fibrils with packed structure due to the presence of hydrogen bonding (Chen et al., 2011). It could also be due to the sonication treatment that caused the fibers to spread unevenly, but not well enough, therefore at low magnification, multiple aggregations of nanofibers are present. It is important to note that when preparing nanosize particles sufficient sonication for the sample is required in order to fully break the fibers into smaller microfibrils (Abu-Thabit et al., 2020). Therefore, the CNC₁ sample needs to be further sonicated in order to avoid the aggregation of the nanofibrils. Furthermore, the appearance of the aggregated nanofibrils could be due to the high specific area between the nanofibers themselves. It is evident that the fibers have rod-like morphologies, which is one of the typical cellulose nanocrystals shape (Kontturi et al., 2018). The same findings of nanocellulose TEM images obtained through sulfuric acid hydrolysis are reported by Moreno et al., 2018. Nevertheless, at high magnification, the morphology of the nanofibers showed that the aggregates are assembled in parallel to each other and are aligned neatly alongside one another. This could be explained by the fact that the hydrogen bonds between the hydroxyl groups are found on the surface of the nanofibrils, which forces the fibers to be aligned in that way (Chen et al., 2011).

Therefore, at high magnification, the appearance of the fibrils is of an organized structure. Furthermore, the ordered arrangement of the fibrils represents the crystalline region of CNC₁ with few amorphous regions. This is due to the removal by sulfuric acid chemical treatment. It is worth mentioning that 64% concentration of sulfuric acid has been reported to be the best in the formation of nanocellulose and that using lower acid concentration can yield lower nanocellulose (Börjesson and Westman, 2015). As for the second methodology, it shows that the CNC₂ also possesses a packed structure due to the strong hydrogen bonding. Moreover, the fibrils, in this case, are more dispersed and less clumped in comparison to CNC₁, although it is similarly evident that the fibers are also rod-shaped cellulose particles. Although, as the magnification increased, the morphology of the nanofibers is shown to be assembled next to each other, where they are similar to the TEM image of CNC₁. Both methods for CNC₁ & CNC₂ have similar morphologies, meaning that the isolation under any procedure is applicable and successful. In the end, the size and shape of cellulose nanocrystals impact the properties it has in an aqueous media, hence these characteristics determine the application of CNCs.

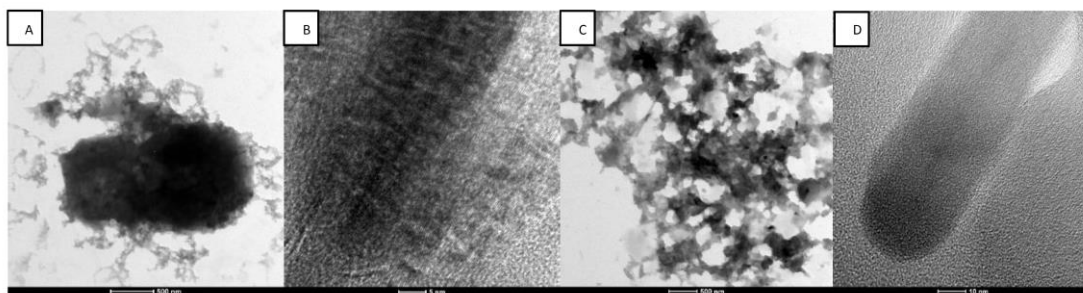


Figure 7. TEM image of A) CNC₁ at high magnification, B) CNC₁ at low magnification, C) CNC₂ at high magnification, D) CNC₂ at low magnification.

4.1.5 Fourier transform infrared (FTIR) analysis

The importance of the FTIR spectrum relies on the fact that it demonstrates significant information regarding the chemical structure of the biopolymers obtained (Eldos et al., 2020). The presence of multiple functionalities such as hydroxyl, methoxy, and cellulosic components were verified from the characteristic peaks detected in the FTIR spectrum of both CNC₁ & CNC₂ as shown in Figure 8. This form of analysis can give us an idea of whether the isolated cellulose nanocrystals are similar in their chemical structure or whether the different methodology of isolation can reveal different chemical structures of CNC.

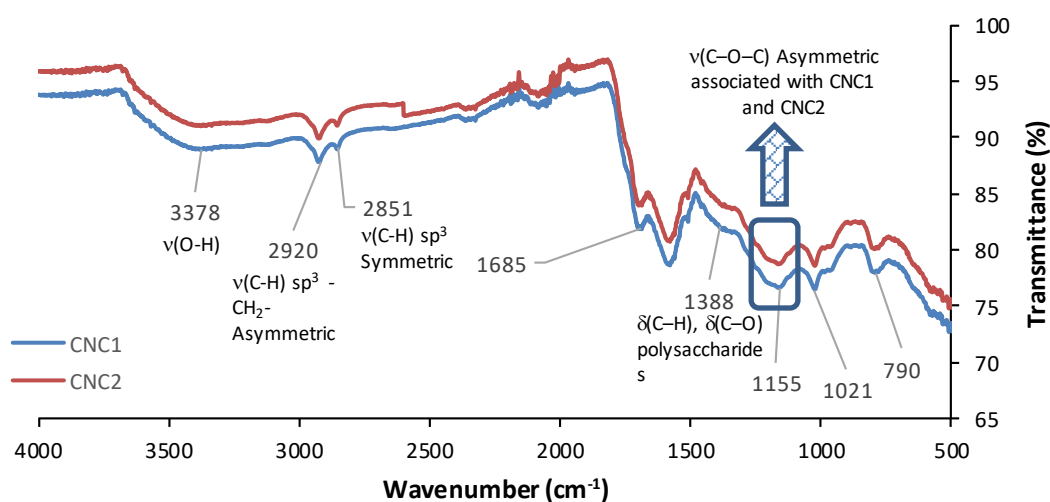


Figure 8. FTIR spectrum of CNC₁ and CNC₂.

As has been previously mentioned, the RDPs consist of primarily cellulose, hemicellulose, and lignin. Therefore, the main functional groups present in these three materials are alkanes, esters, aromatics, ketones, and alcohols with different oxygen-containing functional groups (Chandra et al., 2016). As a result, the elimination of some

peaks in the FTIR spectra will indicate the complete removal of the components posts chemical treatment of the RDP fiber. Two main absorption regions appeared in both curves, where one is at low wavelengths from 500 cm^{-1} to 1750 cm^{-1} and the other at high wavelengths from 2800 cm^{-1} to 3500 cm^{-1} (Zheng et al., 2019). Moreover, O-H stretching vibration in both samples that represent the hydrogen-bonded hydroxyl groups in the cellulose molecules is found near the region 3400 cm^{-1} as a wide broad peak. The peak intensity is reduced due to the successive treatments made by alkali and acid treatment on the RDPs to obtain CNC. Moreover, it can be due to the degradation of the intramolecular and intermolecular hydrogen bonds formed by most of the hydroxyl groups (Abu-Thabit et al., 2020; George & Sabapathi, 2015; Adel et al., 2011). This can also result in lower moisture absorption, hence a broad wide peak is formed (Chandra et al., 2016; Abraham et al., 2013). The broad peak at 1388 cm^{-1} corresponds to the bending vibrations of the C-H and C-O groups of the polysaccharides. The peak at 1155 cm^{-1} was attributed to C-O-C asymmetric stretching vibration associated with CNC₁ and CNC₂. The small peaks at 2851 cm^{-1} and 2920 cm^{-1} are allocated to the C-H stretching vibrations of the methoxyl groups. This signifies the lignin component (Abu-Thabit et al., 2020). This means that small traces of lignin materials are found in both samples. Furthermore, since these bands are not strong sharp peaks, then it can be inferred that most of the lignin components are removed by the delignification process by the NaOH treatment.

It is necessary to note that the FTIR results should demonstrate cellulose components since CNCs originate mainly from them. For example, the peak at 897 cm^{-1} corresponds to the C₁-H deformation of the glucose ring in cellulose (Kubovský et al., 2020). In the current study, this band is found at 790 cm^{-1} , where it indicates that the original molecular structure of cellulose was still maintained even with the removal of

lignin and hemicellulose components. Furthermore, the vibrations of adsorbed water molecules are demonstrated at bands 1685 cm^{-1} (Zheng et al., 2019; Haafiz et al., 2013; Mandal & Chakrabarty, 2011). This is due to cellulose and water molecules strong interactions with each other even though all the samples are dried at 70°C (Abu-Thabit et al., 2020). The stretching vibration of the C–O–C bonds are shown at peaks 1155 cm^{-1} and 1021 cm^{-1} in both samples. These peaks correspond to the typical cellulose structure shown in previous studies (Kubovský et al., 2020; Luzi et al., 2019). It can be concluded that modification presented by sulfuric acid that was used to obtain CNCs is successful due to the significant peaks that represent the changes in its chemical structure. The CNCs were successfully extracted from the methods (1 & 2) without any further degradation or secondary product formation. Based on the FTIR spectrum, both CNC samples had similar chemical structures and no significant changes were observed; therefore, any isolation methods (1 & 2) can be used in the future to attain CNC.

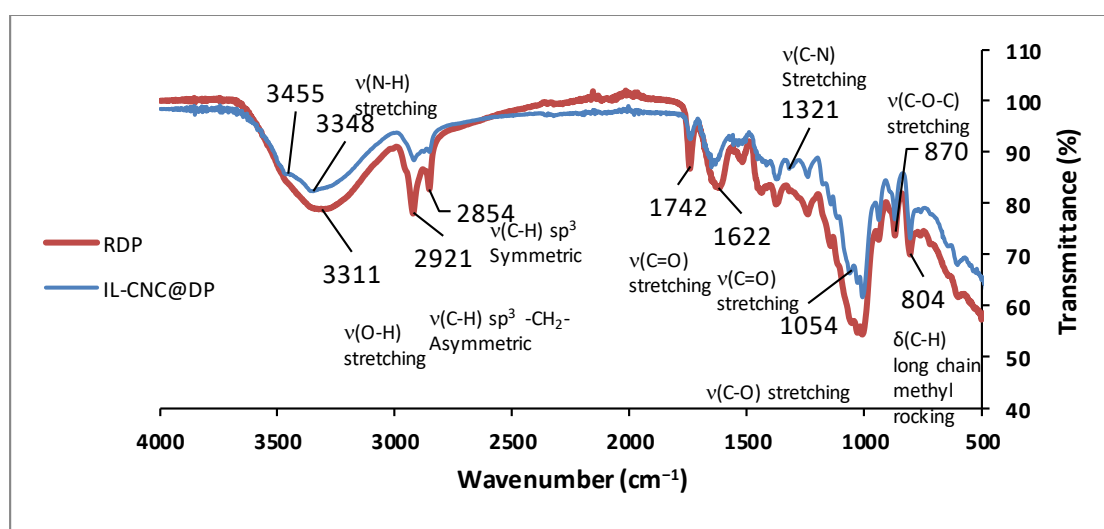


Figure 9. FTIR spectrum of the unmodified RDP and the modified IL-CNC@DP adsorbents.

It is also clearly evident that the modification performed by IL and CNCs did occur. By looking at the spectra in general, the adsorbent IL-CNC@DP has less intense peaks in comparison to the RDP due to the modification performed. One important finding that the FTIR spectra presented is the bending of the peaks in the 3000-3500 cm^{-1} region of IL-CNC@DP. The peaks at 3348 cm^{-1} and 3455 cm^{-1} are attributed to the N-H stretching vibration absorption peak found in the adsorbent (Zheng et al., 2019). This means that there is a hydrogen bonding between the nitrogen of the IL and the hydroxyl groups of the CNCs. This is also represented in Figure 9. Moreover, that indicates why the broad O-H stretching band at 3311 cm^{-1} in the RDP is found and in the IL-CNC@DP adsorbent, the peak is starting to shift to present bending peaks. The same bands at 2851 cm^{-1} and 2920 cm^{-1} that are found in Figure 8 are found in the IL-CNC@DP adsorbent at 2854 cm^{-1} and 2921 cm^{-1} . Nonetheless, it can be inferred that their intensity and sharpness of the absorption bands decreased in comparison to the RDP and this can be explained by the fact that the CNC sample that was used to prepare the modified adsorbent had less lignin content that was removed by the hydrolysis treatment in order to obtain pure CNC.

To understand the modification better, the peak at 1742 cm^{-1} implies significant results. This noticeable sharp peak represents hemicellulose of the RDP and the same peak disappeared when the pure CNC was obtained. Nevertheless, this peak was reintroduced in the IL-CNC@DP adsorbent indicating this time the presence of aldehyde corresponding to the C=O stretching of the IL, demonstrated in Figure 9 (Gholami-Bonabi et al., 2020). Furthermore, there are other absorption peaks, which represent the lignin components in the range of 700 cm^{-1} - 900 cm^{-1} related to the C-H functional group of the aromatic hydrogen compound (Morán et al., 2008). The peaks

are visible in both adsorbents because date pits were used as the supporting mechanism in the case of the modified adsorbent. Comparing this result to Figure 8, the various absorption peaks are not available which further proves that the chemical treatment performed is indeed effective. The peak at 1622 cm^{-1} correlates to the C=O asymmetric stretching band in hemicellulose and to the conjugated carbonyl of lignin stretching (Zhuang et al., 2020). It can be seen that in the IL-CNC@DP adsorbent the peak shifted slightly to the left and became narrower due to the modification performed on the sample that removed part of the hemicellulose and lignin components. In addition, a closer look of the FTIR spectra demonstrates a peak that is only visible in the novel adsorbent at 1321 cm^{-1} that represents the C-N stretching of the IL that was used to modify the RDP. Lastly, the peak at 1054 cm^{-1} in the IL-CNC@DP corresponds to the C-O stretch in cellulose and hemicellulose (Al-Ghouti et al., 2010). From figure 9, it can be shown that this peak is more evident in the modified IL-CNC@DP sample more than the RDP possibly due to more cellulosic components from the CNC.

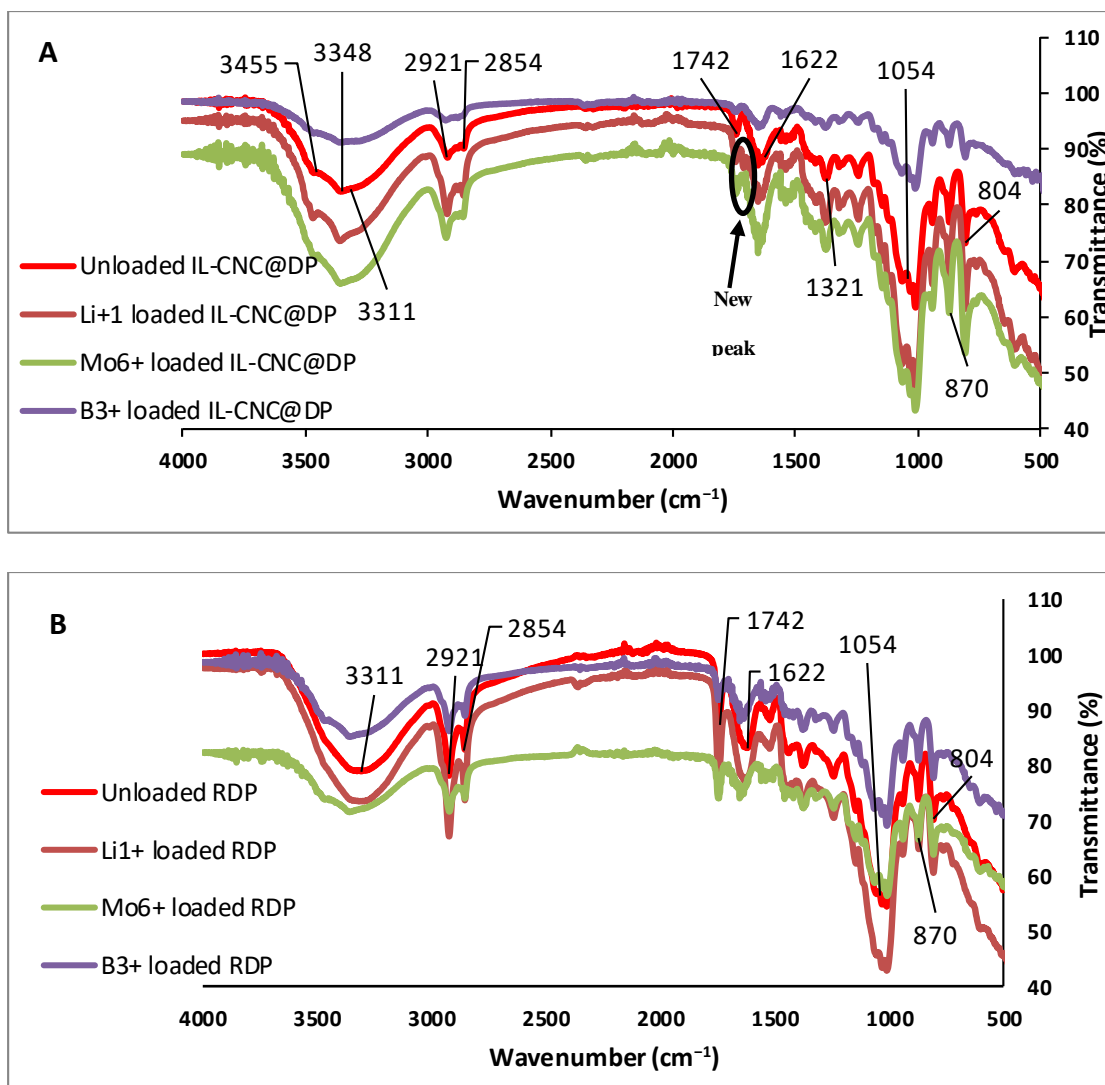


Figure 10. FTIR spectra of the IL-CNC@DP and RDP before and after Li^{1+} , Mo^{6+} , B^{3+} ions adsorption. (A) IL-CNC@DP and (B) RDP.

Figure 10A demonstrates the FTIR spectra of the four samples, namely unloaded IL-CNC@DP, Li^{1+} loaded IL-CNC@DP, Mo^{6+} loaded IL-CNC@DP, and B^{3+} loaded IL-CNC@DP at an initial concentration of 100 mg/L. Visible differences can be detected in the FTIR spectra regarding the absorbance shapes and locations of the bands but the absorbance pattern did not significantly change after the adsorption of Li^{1+} , Mo^{6+} , & B^{3+} . For example, the bending of the peaks in the 3000 cm^{-1} - 3500 cm^{-1} region at 3348 cm^{-1} and 3455 cm^{-1} that corresponds to the N-H stretching vibration absorption became

more intense and sharper after the adsorption of the Li^{1+} ions. The adsorption of Li^{1+} onto IL-CNC@DP caused a dip in the two peaks as they become narrower comparing to the unloaded adsorbent. As for the adsorption of Mo^{6+} onto IL-CNC@DP, the intensity of the two peaks decreased in comparison to the Li^{1+} metal, however, in comparison to the unloaded adsorbent IL-CNC@DP, the absorption peaks became broader and slightly sharper. Moreover, these two bands are becoming unnoticeable after B^{3+} was loaded onto IL-CNC@DP due to the different adsorption mechanisms the metal possesses. Additionally, the O-H band at 3311 cm^{-1} in the unloaded IL-CNC@DP is broad as it started to present bending peaks but after the adsorption of Li^{1+} and Mo^{6+} , the width of the entire band became narrower. On the other hand, the B^{3+} adsorption band at 3311 cm^{-1} became wider in comparison to the three FTIR spectra. This can also be explained by the possibility of the different adsorption mechanisms each ion possesses. As for the C-H stretching vibrations of the methoxyl groups at 2851 cm^{-1} and 2920 cm^{-1} after adsorption, the band's intensity and sharpness are signifying that the lignin functional group that is found from the date pits is expected to contribute to the Li^{1+} & Mo^{6+} binding. Whereas, the band's intensity and sharpness decreased significantly implying that the lignin functional group is not the main contributor to the B^{3+} adsorption and that other functional groups could be contributing to it. Moreover, the peak at 804 cm^{-1} that also represents the lignin components related to the C-H functional group demonstrates more intensity and sharpness after the adsorption of Li^{1+} & Mo^{6+} takes place. However, the peak after B^{3+} adsorption demonstrates less intensity and sharpens. As for the unconjugated C=O hemicellulose functional group at 1742 cm^{-1} , the peaks remained the same before and after adsorption suggesting that perhaps this functional group did not contribute to the adsorption process for Li^{1+} & Mo^{6+} adsorption. Nonetheless, the peak changed after B^{3+} adsorption as it became less

noticeable than the others. Although looking closely at the FTIR spectra of Li^{1+} loaded IL-CNC@DP, and Mo^{6+} loaded IL-CNC@DP, it can be shown that a small peak can be detected at around 1707 cm^{-1} . This means that the hemicellulose functional group from the date pits did in fact contribute to the Li^{1+} & Mo^{6+} binding for the adsorption process since they are only visible on the Li^{1+} & Mo^{6+} loaded IL-CNC@DP. Furthermore, the peak 1622 cm^{-1} did not change for the Li^{1+} loaded IL-CNC@DP but as for the Mo^{6+} loaded IL-CNC@DP the peak became sharper and narrower. It is also worth mentioning that after B^{3+} loaded IL-CNC@DP, the peak became wider but less sharp in comparison to Mo^{6+} loaded IL-CNC@DP suggesting the different adsorption behavior between the two metal ions. The peaks that were observed at 1321 cm^{-1} and 1054 cm^{-1} demonstrated no alterations in the absorbance bands after the adsorption of Li^{1+} & Mo^{6+} , but as for B^{3+} , the peaks slightly changed.

Figure 10B shows the FTIR spectra of the four samples, corresponding to the unloaded RDP, Li^{1+} loaded RDP, Mo^{6+} loaded RDP, and B^{3+} loaded RDP at an initial concentration of 100 mg/L . For the unloaded RDP, a strong inter- and intra-hydrogen bonding (O-H) stretching absorption is seen at 3311 cm^{-1} that occurs in cellulose components. After adsorption of Li^{1+} ions no changes in the hydroxyl band occurred, although a difference is seen in this band after the adsorption of Mo^{6+} & B^{3+} ions suggesting the possibility of the different adsorption mechanisms each metal ion possesses since it started to present bending peaks in the broad O-H stretching band. Furthermore, the peaks at 2854 cm^{-1} and 2921 cm^{-1} that correspond to the lignin content show a sharp dip after the loading of Li^{1+} ions but as for Mo^{6+} & B^{3+} ions, the bands remained the same. This proposes that the lignin functional group found in RDP after the adsorption of Li^{1+} ions contributes to the adsorption process. Furthermore, there are other absorption peaks, which represent the lignin components in the range of 700 cm^{-1}

¹ - 900 cm⁻¹, such as band 804 cm⁻¹, where no differences in adsorption of Li¹⁺, Mo⁶⁺, & B³⁺ occurred. As for the unconjugated C=O hemicellulose functional group at 1742 cm⁻¹, the peak became sharper after the adsorption of Li¹⁺ ions, whereas for the Mo⁶⁺ & B³⁺ ions, the peaks became less sharp. This can suggest that the hemicellulose functional group found in RDP plays a role in the adsorption process. The peak at 1622 cm⁻¹ did not change for the Li¹⁺ loaded IL-CNC@DP but as for the Mo⁶⁺ & B³⁺ loaded IL-CNC@DP the peak became smaller and narrower suggesting the different adsorption behavior between the three ions. Lastly, the peak at 1054 cm⁻¹ for the three ions demonstrated no significant changes in the absorbance peaks.

4.1.6 X-ray powder diffraction (XRD) analysis

Biomass composed of lignocellulosic components has amorphous and crystalline regions according to Chandra & Madakka (2019). This amorphous region is due to the presence of lignin and hemicellulose found in date pits, on the other hand, the crystalline region is due to the presence of cellulose. Therefore, the treatment that is done chemically leads to the depolymerization of hemicellulose and delignification of RDPs, which tends to increase the crystallinity of cellulose obtained in the end. The XRD analysis of the extracted cellulose from both methods that are successfully converted to nanocellulose is indicated by the crystalline nature of the fibers as shown in Figure 11. The XRD spectra of CNC₁ are represented by diffraction peaks at 2-theta (2θ) values 15.9°, 22.6°, and 33.8 °. Similarly, the diffractogram of the CNC₂ from method 2 also shows similar peaks. These peaks correspond to the lattice planes 110, 200, and 004, respectively (Guo et al., 2020; Zheng et al., 2019; Chandra et al., 2016). The peaks of both samples indicate that the typical cellulosic structure was maintained and preserved. This further indicates that the chemical treatments done to obtain CNCs by using sulfuric acid did not modify it (Marett et al., 2017). The sharp diffraction peak

at $2\theta = 22.6^\circ$ proves that high crystallinity is present as reported by Trilokesh & Uppuluri (2019). In the current study, this sharp peak is present at 15.9° , which still proves the high crystallinity of cellulose extracted from RDPs, is present. The order of the crystalline arrangements in each CNC is reported due to the formation of inter and intramolecular H-bonding by the hydroxyl groups. This H-bonding tends to limit the movement of the cellulosic chains that causes the chains to align next to one another, which forms the crystallinity of the cellulose (Chandra et al., 2016). From equation (3), the crystallinity index is calculated for CNC₁ & CNC₂ to measure if the % crystallinity changed based on the two different methodologies. It was found that the apparent crystallinity of CNC₁ was 67.06%, whereas the crystallinity of CNC₂ was 61.58%. The decrease in the crystallinity index could be due to the sulfuric acid hydrolysis and ultrasonication that could have caused damage to the amorphous and crystalline regions of the cellulose (Zheng et al., 2019). In general, there were no noteworthy changes in the location of the XRD bands between the CNC₁ & CNC₂. Furthermore, the results from methods 1 & 2 demonstrate high crystallinity that is attributed to the effective removal of the non-crystalline regions due to the consecutive chemical treatments performed on RDPs. Table 9 summarizes the crystallinity percentage of the CNC obtained, and other CNC obtained from different resources by acid hydrolysis.

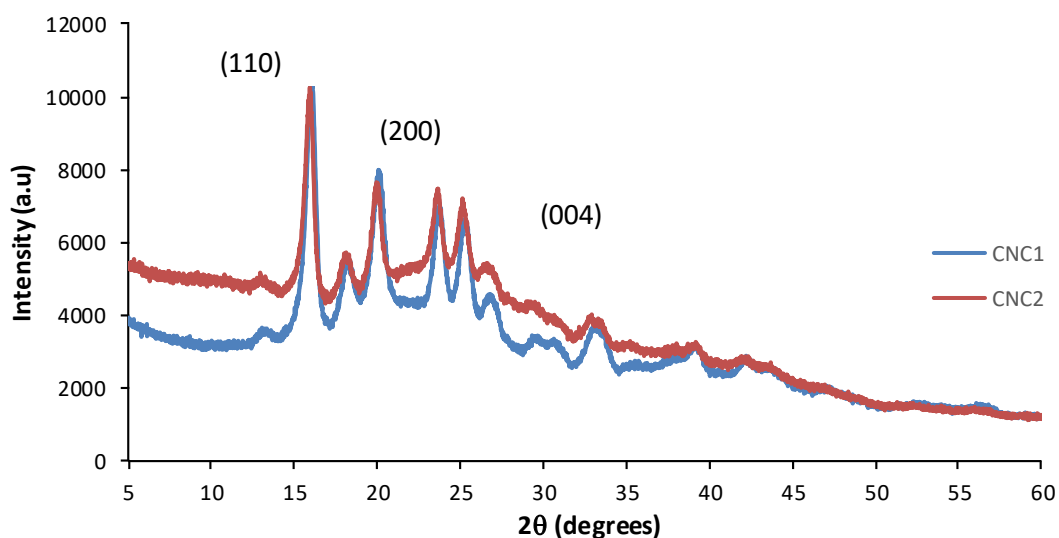


Figure 11. XRD patterns of CNC₁ and CNC₂.

Table 9. Crystallinity value of cellulose nanocrystals (CNC) obtained from different sources through acid hydrolysis.

Cellulose nanocrystal's (CNC) source	Crystallinity (%)	Reference
RDP (CNC ₁)	67.06	This Study
RDP (CNC ₂)	61.58	This Study
Industrial bio-residue (CNC-BR)	85.4	Herrera et al., 2012
Sugarcane peel (SP-CNC)	99.2	Abiazem et al., 2019
Jackfruit peel	83.42	Trilokesh & Uppuluri, 2019
<i>Eucalyptus globulus</i>	55.3	Carrillo et al., 2018
<i>Eucalyptus Benthamii</i>	54.1	Carrillo et al., 2018
Walnut shell (WS-CNC)	40.1	Zheng et al., 2019
Sisal fibers	94.03	Sosiati et al., 2017
Sugarcane bagasse	76.89	Evans et al., 2019
<i>Calotropis procera</i>	68.7	Song et al., 2019

4.2 Mechanisms of adsorption onto IL-CNC@DP modified adsorbent

Understanding the different mechanisms each metal demonstrates, it can help with understanding the adsorption process onto IL-CNC@DP and RDP surface. The reason for adsorption can result from the solubility of the solute relative to the solvent. Moreover, it could be due to the affinity the solute possesses towards the adsorbent. Therefore, this type of attraction could be mainly due to electrical, van der Waals forces, or chemical reactions (Alimohammadi et al., 2017). The surfaces of the adsorbent and its outcome on the process of adsorption are significant to understand the entire solute adsorption. The FTIR results can help determine the relationship and interaction between the adsorbate and functional groups that are found on the surface of the adsorbent. Other parameters such as the effect of pH and initial concentration are of importance in determining the adsorption mechanisms. Taking into account that the removal of metal ions from any aqueous solutions can be done by a variety of different methods such as chemical precipitation (Wang et al., 2018), ion exchange (Peng & Guo, 2020), adsorption (Castro et al., 2018), membrane filtration (Ates & Uzal, 2018), and electrochemical treatment (Zhou et al., 2015). Nonetheless, adsorption is considered one of the dominating methods used considering its low-cost, economically friendly, and high efficiency (Ouyang et al., 2019). Therefore, the adsorption process is undeniably the most noteworthy physicochemical process that is reasonable for the remediation of aquatic environments from inorganic and organic pollutants (Jeirani et al., 2017). Hence, multiple adsorption mechanisms such as electrostatic attractions, chelation, ion exchange, bridging, π - π interactions, hydrogen bonding, and complexation can be employed in the adsorption mechanism (Zhang et al., 2019). This work investigates the adsorption mechanisms of Li^{1+} , Mo^{6+} , & B^{3+} from aqueous solutions onto the novel IL-CNC@DP. The RDP was used as a reference material due

to the fact that date pits are commonly used in the remediation and removal applications of pollutants (Al-Ghouti et al., 2019; Saleem et al., 2019; Crini et al., 2019; Mahdi et al., 2018; Al-Ghouti et al., 2017).

The uptake of Li^{1+} , Mo^{6+} , & B^{3+} from aqueous solutions is significantly influenced by the chemistry and surface morphology of the adsorbents. It is worth mentioning that the RDP is considered acidic in nature with a pH value of 4.6 (Al-Ghouti et al., 2010). This is because of the presence of multiple functional groups such as phenolic hydroxides, alcohols, and ethers. Furthermore, under acidic conditions, when the pH is too low, the functionality of the groups is not changed, whereas, at higher pH values, the groups will begin to neutralize their activities and binding properties (Al-Ghouti et al., 2010). The RDP is mainly composed of cellulose with the empirical formula of $(\text{C}_6\text{H}_{10}\text{O}_5)_n$. In addition, 28.1% and 19.9% account for hemicellulose and lignin, respectively (Al-Ghouti et al., 2019). In Figure 14, it can be seen that the RDP consists of mainly cellulose, hemicellulose, and lignin (Díez et al., 2020; Jung et al., 2015; Isik et al., 2014). Cellulose and hemicellulose comprise the majority of oxygen functional groups such as hydroxyl, ether, and carbonyl that are present in the lignocellulosic components of RDP. On the other hand, lignin is considered a complex polymer of aromatic substances, which tends to act as a cementing matrix that binds within and amongst cellulose and hemicellulose components (Lu et al., 2017). Therefore, the existence of these groups on the surface of the adsorbent considerably influences the adsorption characteristics of Li^{1+} , Mo^{6+} , and B^{3+} . Hydrogen bonding and electrostatic interactions due to the hydroxyl groups of cellulose, hemicellulose, and lignin and the oxygen atom of the aldehyde compound that is found in the IL, illustrated in Figure 14.

In more detail, to prepare the modified RDP, the obtained IL and the isolated CNCs are used to create a composite, shown in Figure 12, along with the RDP to functionalize

and improve the adsorption capacity of the ion uptake. Once the composite is prepared, it can be then used as an adsorbent to remove Li^+ , Mo^{6+} , & B^{3+} ions from a solution. It is worth mentioning that the RDP used throughout this whole study had two main roles. Firstly, cellulose is extracted from the RDP and then converted to CNCs in order to have a high surface to volume ratio. Secondly, the RDP is used as a supporting material, where it can facilitate the adsorption process by forming a film layer over its surface with IL-CNC that promotes high surface to volume ratio, biodegradability, high functionalizability, and sustainability. Also, the fact that the percentage removal efficiency was dependent on the pH value; therefore this can indicate that ion exchange and electrostatic interactions are involved in the removal of the Li^{1+} , Mo^{6+} , & B^{3+} ion by IL-CNC@DP and RDP (Al-Ghouti et al., 2019). The availability of hydroxyl groups, as previously mentioned, would help in the adsorption process, which will enhance the adsorbent binding levels along with the electrostatic interactions that are occurring. The mechanism of ion exchange occurs as Li^{1+} , Mo^{6+} , & B^{3+} ions bind to the anionic sites by returning protons from acidic groups found on the adsorbent's surface (Hawari et al., 2014).

The adsorption behavior of Li^{1+} , Mo^{6+} , and B^{3+} ion onto the IL-CNC@DP surface might be explained by the fact that when ions are added, the ions willingly adsorb on the surface of the adsorbents. This action at first initially happens on the external surface of the adsorbents, therefore high metal concentrations will tend to increase. Monodentate, bidentate, or polydentate aggregates of Mo^{6+} and B^{3+} ions could be favored onto the adsorbent, also monodentate aggregates of Li^{1+} exclusively occur onto the adsorbent. This means that depending upon the size and orientation of adsorbed Li^{1+} , Mo^{6+} , & B^{3+} ions, different structural surface complexes tend to form, as shown in Figure 13. It is important to mention that there is a chance these ions migrate and

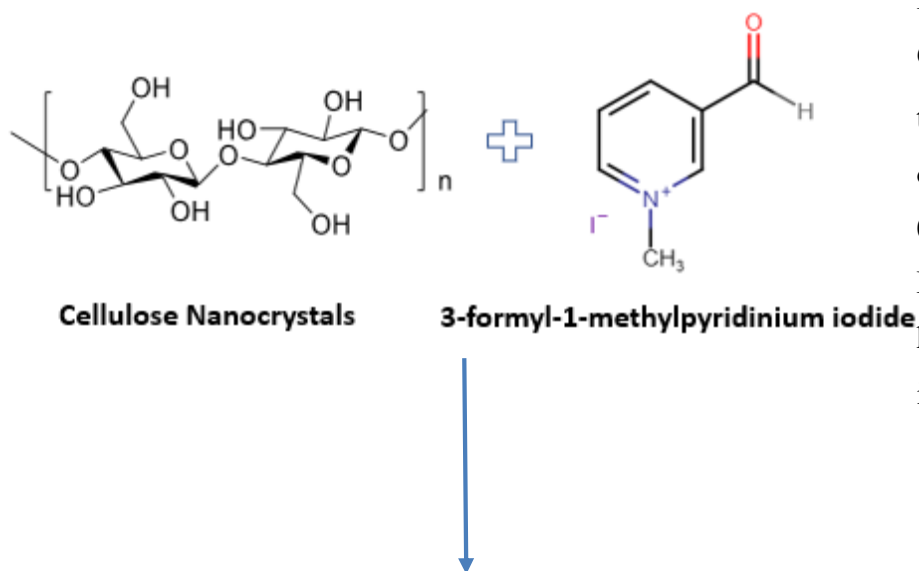
penetrate from the external surface of the adsorbents to their pores, as shown in Figure 15 (Al-Ghouti et al., 2014).

Moreover, understanding the physicochemical properties of Li^{1+} , Mo^{6+} , and B^{3+} is considered to be vital for improving the removal and recovery of ions and to understand the adsorption mechanisms (Al-Ghouti et al., 2014). To find possible attractive sites between Li^{1+} , Mo^{6+} , and B^{3+} adsorbate ions and the CNCs adsorbent's surface, characteristic properties such as crystal radius, equilibrium constants, and electronegativity for adsorbate ions are shown in Table 10. Moreover, ions that tend to have larger electronegativity and high hydrolysis coefficients, adsorb effortlessly. On the other hand, ions with a high ionic radius have a low charge density and low electrostatic attraction. This will tend to decrease the adsorption (Minceva, 2008). In this study, the size and structure of each ion tend to impact the mechanism and the mobility of the ions such as the crystal radius for the chosen Li^{1+} , Mo^{6+} , and B^{3+} ions. According to Table 10, it can be shown that B^{3+} is the most capable to be adsorbed on the surface of the adsorbents (inter-particle diffusion) and migrating into the pores of the adsorbents (intra-particle diffusion) since it has the smallest crystal radius (0.25 Å). Whereas, Li^{1+} and Mo^{6+} have almost similar crystal radius values of 0.9 Å and 0.79 Å, respectively. Therefore, external and internal diffusions will most likely not be found, or they could be fewer in comparison to B^{3+} diffusion. Consequently, it can be concluded that according to each ion's crystal radius, the adsorption behavior will be different. In other words, the smaller the crystal radius is, the easier it is for the metal to be adsorbed on the surface and into the pores. The adsorption mechanisms can be studied according to the ion hydrolysis constant (pKa), where a larger hydrolysis constant would increase the adsorptive capacity. It is evident that B^{3+} in an aqueous solution reacts to give a weakly acidic cation named boric acid $\text{B}(\text{OH})_3$ with a pKa

value of 9.24. Therefore, the adsorptive capacity of B^{3+} is significantly high as it reached 98.2 mg/g at 35 °C and 99 mg/g at 45 °C at an initial concentration of 100 mg/L. Furthermore, Li^{1+} reacts to give a feebly acidic cation like $Li(OH)$ with a pKa value of 9.24. According to the obtained results of the effect of initial concentration and temperature, the adsorption capacity of Li^{1+} reached 99 mg/g at 100 mg/L of initial ion concentration onto IL-CNC@DP. Therefore, the adsorptive capacity of Li^{1+} is quite high. On the other hand, molybdate ions in water produce molybdic acid (MoO_3 or $MoO_3(OH)_3$) that is strongly acid with a low pKa value of 0.9. The results prove to demonstrate that Mo^{6+} adsorption reached 89 mg/g at 100 mg/L of initial metal concentration onto IL-CNC@DP, which is less than the adsorption capacity of Li^{1+} . This is due to the differences in their hydrolysis constant (pKa). In addition, the ion's adsorption mechanism can be discussed according to the electronegativity of each ion. This means that the metal with the highest electronegativity tends to adsorb more easily. However, Mo^{6+} and B^{3+} have almost the same electronegativity at 2.16 and 2.051, respectively, but different adsorption capacities. This might explain our above hypothesis that the inter- and intra-particle diffusion is the controlling mechanism of adsorption in the case of B^{3+} and that the adsorption of Mo^{6+} occurs most probably only onto the external surface of the adsorbent (inter-particle diffusion), which implies why their adsorption capacities are different from one another. Nonetheless, Li^{1+} has the least value regarding its electronegativity, but it has the highest adsorption capacity due to the hydrolysis constant (pKa).

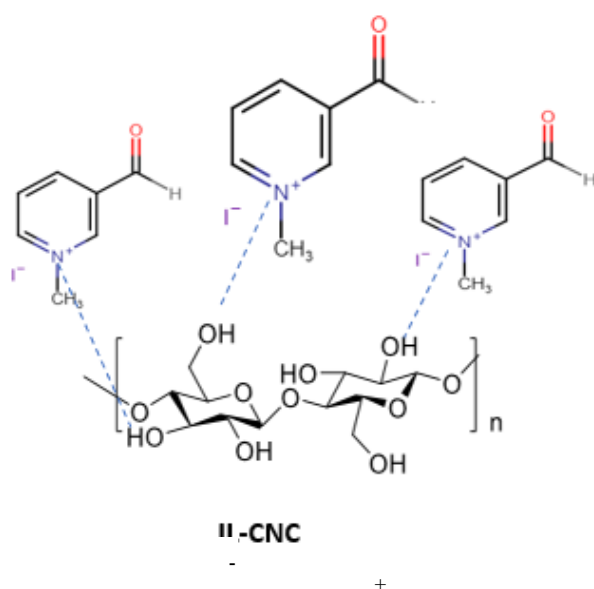
Table 10. Physicochemical characteristics of Li^+ , Mo^{6+} , & B^{3+} ions.

Adsorbate ion	Crystal radius r_{cryst} (Å) (Shannon, 1976)	Hydrolysis constant pKa (Nagul et al., 2015; Miessler et al., 2014; Wulfsberg, 1987)	Pauling electronegativity (Wulfsberg, 1991)
B^{3+}	0.25	Boric acid $\text{B}(\text{OH})_3$ 9.24	2.051
Mo^{6+}	0.79	Molybdic acid (MoO_3 or $\text{MoO}_3(\text{OH})_2$) 0.9	2.16
Li^+	0.9	$\text{Li}(\text{OH})$ 13.6	0.912



Isolated cellulose was treated by 64% sulfuric acid (H_2SO_4) for 1 hr then centrifuged and sonicated to obtain pure CNCs.

0.01g IL was solubilized in 50 ml DMSO until the solution is homogenized. Then, 0.05g of CNC is added to the mixture and left for 1 hr.



Electrostatic attraction and hydrogen bonding between nitrogen ions of the IL with hydroxyl groups of the CNC.

Figure 12. Schematic representation of the formation of the modified IL-CNC@DP adsorbent.

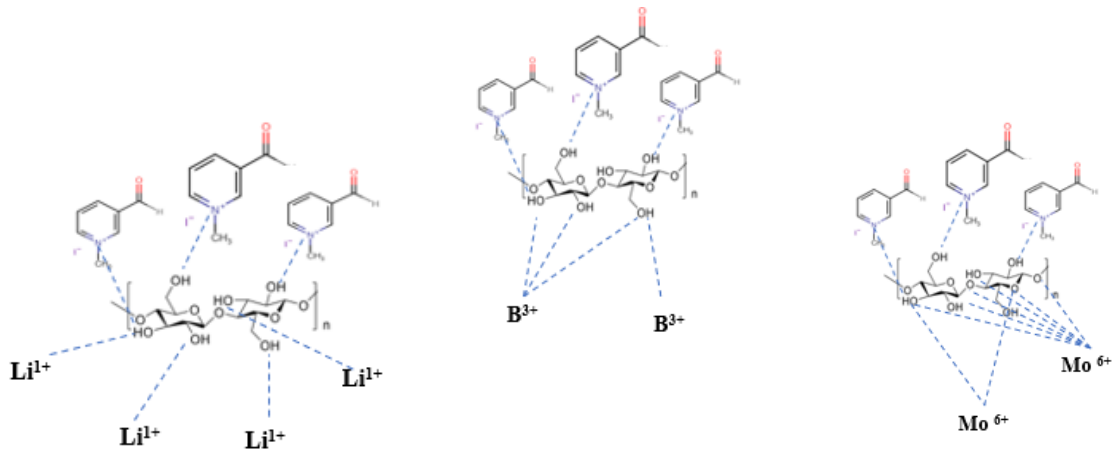
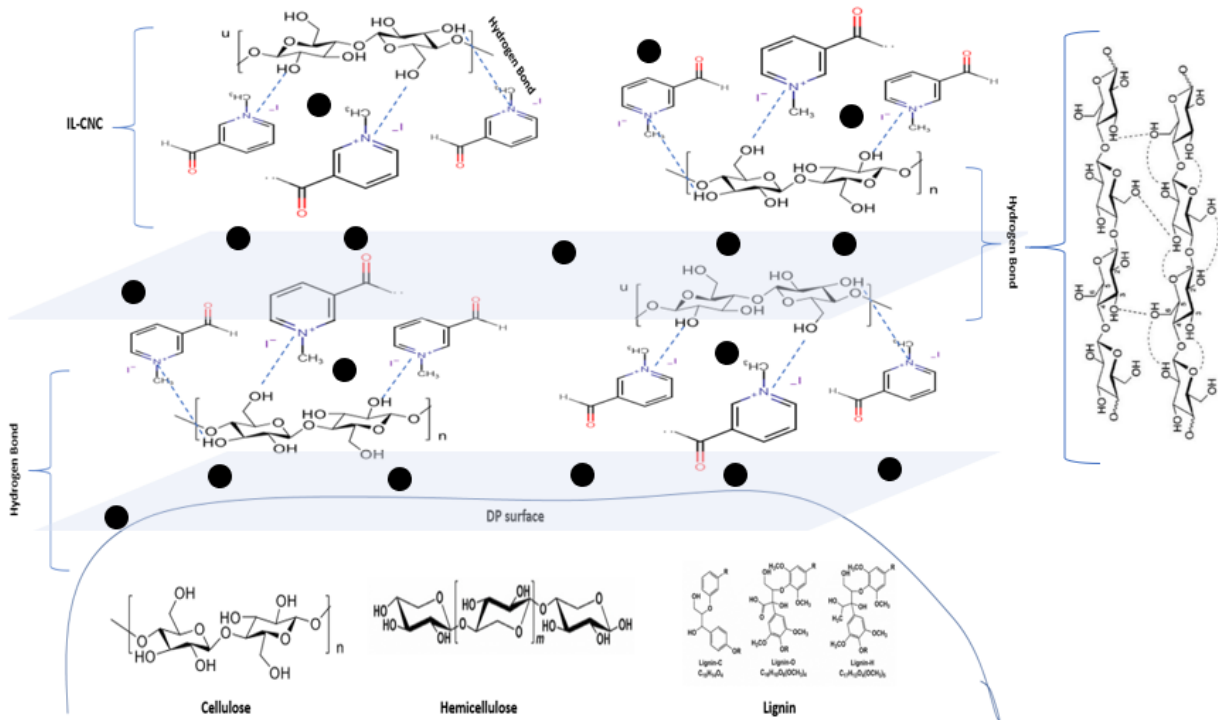


Figure 13. Proposes the different mechanisms of adsorption onto the adsorbent by the



pollutants through monodentate, bidentate, or polydentate ligands.

Figure 14. Schematic representation of the modified adsorbent IL-CNC@DP.

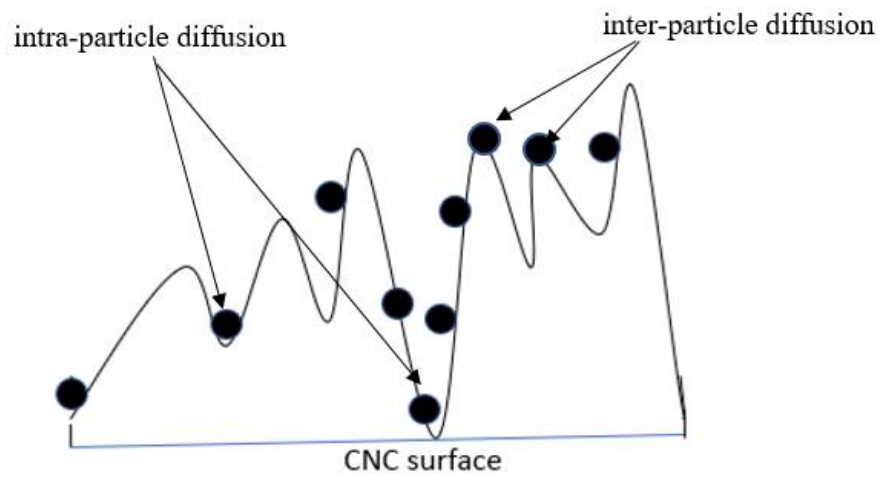


Figure 15. Adsorption onto the surface of CNC and its pores, modified from Al-Ghouti et al. (2014).

4.3 Effect of pH value on Li^{1+} , Mo^{6+} , and B^{3+} ions adsorption

The demand for water in Qatar is increasing; leading to a national water crisis in the region (Hussein & Lambert, 2020), and as Qatar relies on groundwater aquifers to be the sole source of natural water (Baalousha & Ouda, 2017; Ismail, 2015). Therefore, high priority should be given to groundwater management and protection. The groundwater in Qatar demonstrates that the mean concentration of Li^{1+} is 0.120 mg/L, which are considered higher than WHO limits of drinking purposes. Most of the studies performed were done on lithium in drinking water and the correlation it has with suicide mortality rates (Helbich et al., 2015; Helbich et al., 2012). However, other studies focused on extracting Li^{1+} from seawater by relying on the adsorption method using manganese oxide as an adsorbent (Liu et al. 2015; Park et al. 2015). Since Li^{1+} is considered a very rare metal and the increasing demand for it in the coming years will keep on growing, developing various methods for the recovery of Li^{1+} is essential. As stated by Murodjon et al. (2020), recovering Li^{1+} from seawater, brine, or geothermal water by precipitation, extraction, membrane separation, and adsorption are the commonly listed methods for recovery. The most promising method proved to be the adsorption method because of its cost-effectiveness and sustainable nature. Previous researches demonstrated that equilibrium is attained in 24 h. Therefore, in these experiments, the initial pH of the solute comprising the solution was adjusted to the desired value of 2, 4, 6, 8, and 10. The pH was adjusted using either 1 M HCl or 1 M NaOH solution. The adjusted pH was then used to study the adsorption of Li^{1+} . The effect of pH on the percentage removal of solute from the aqueous solution by IL-CNC@DP & RDP that was used as control is illustrated in Figure 16. Therefore, this gives an idea about the adsorption mechanism and the efficiency removal so it can be applied on a larger scale to treat groundwater in Qatar.

The modification done on raw date pits by using CNCs and IL can increase the functional groups to improve its adsorption capabilities, stability, and interaction with Li^{1+} . For example, as previously mentioned, Zante et al. (2019) effectively confirmed the use of supported ionic liquid membranes (SLMs) to extract lithium. The SLMs were used to separate lithium cations from a mixture of an aqueous solution by infusing mixtures of hydrophobic ionic liquid. Impregnation or infusing of membranes displays that the mass uptake of ILs is associated with the density of the organic phase. Moreover, the stability of the membrane is related to the solubility of the organic phase. As a result, due to the several useful features of ILs, they have been shown to combine with nanomaterials for combined functionalities and their use has been demonstrated in catalysis and separations. Therefore, in this study, the adsorption of Li^{1+} onto IL-CNC@DP was investigated by studying the first parameter, which is solution pH. It is important to note that pH is one of the significant parameters impacting metal ions' adsorption (Liang et al., 2020; Xu et al., 2020; Xiao et al., 2015). Lithium, an alkaline-earth metal, is found in a solution as a protonated form with an atomic number of three (Ahmad et al., 2020). This means that at a lower pH value, H^{+} ions at high concentrations can compete with the metal ions for the active sites to form protonation. Hence, the percentage of solute removal tends to decline. The increase in the pH value demonstrated an increase in the removal capacity of Li^{1+} by both adsorbents, IL-CNC@DP & RDP. In more details, the Li^{1+} adsorption onto the adsorbent IL-CNC@DP displays a trend, where it shows as the pH value increases from 2 to 10, the adsorption also increases. The lowest adsorption was observed at pH 2, which was found to be at 55%. While the highest percentage of removal was found to be at pH 6 and 8 at 90%. The differences between the adsorption behavior is due to the fact that the solution at low pH possesses highly protonated H^{+} ions where it competes with the

protonated Li^{1+} for the active sites on the negatively modified adsorbent. As a result, this will cause lower adsorption for low pH values. Furthermore, at low pH values, the H^+ ions might desorb the previously bound metals back into the solution (Hawari et al., 2014). It is worth noting that at low pH, protonation of the surface functional group occurs; hence, a positive charge would be formed on the surface. On the other hand, while at high pH, the surface loses its protons and it will become anionic (Heibati et al., 2014). Moreover, at pH 4, the percentage removal slightly increased as the competing behavior in the solution decreased, which allowed the adsorption to be enhanced. At pH 6, there is a significant increase in the removal efficiency where it increased to 90%. This also could be explained by the fact that electrostatic attraction forces and hydrogen bonding existed between the protonated Li^{1+} and the less protonated IL-CNC@DP adsorbent surface, which enhanced the percentage of solute removal. Nevertheless, as the pH becomes more basic at values 8 & 10, it will be concentrated with more OH^- ions, therefore the attraction forces increased between the positively charged Li^{1+} and the negatively charged surface of the adsorbent. This will allow more adsorption of Li^{1+} to occur and enhance the removal percentage at high pH values. Another explanation could be due to "faked" adsorption behavior due to the presence of metal ions, such as Li^{1+} , and at high concentrations of OH^- ions, lithium hydroxides (LiOH) in the solution forms. Precipitation of metals forms metal hydroxides at high pH values is explained in recent studies (Eggermont et al., 2020; Kim et al., 2020; Soliman & Moustafa, 2020). Therefore, the high adsorption behavior could be due to the behavior of metals and not the adsorption mechanism itself. Another study by Al-Ghouti et al. (2010) demonstrated the adsorption mechanism of two metals onto RDP under different pH values. The results show a similar trend in the fact that the adsorbent under basic conditions and less protonated forms, the precipitation of metals occurs. To try to

understand the modification better, the RDP was used as a control to compare with the novel adsorbent; IL-CNC@DP. The control adsorbent shows a similar trend as the one observed by the modified adsorbent. In other words, at pH 2 the percentage of solute removal was found at 17%, and at pH 10, the percentage of solute removal increased to 45%. The pH values at 4, 6, and 8 have minor differences regarding their adsorption efficiency, where the values are 20, 23, and 25%, respectively.

This also proves that the utilization of RDP alone without modifications is not as efficient enough to be used as adsorbents for the selective adsorption of lithium in comparison to the modified adsorbent, IL-CNC@DP. Besides, it further proves that the modification on RDP by using CNCs and IL occurred as it improved its adsorption capabilities by enhancing its functional groups, which is supported by the FTIR analysis shown in Figure 9. Furthermore, other studies support the fact that cellulose is an important polymer for the adsorption of Li^{1+} elements at high pH values. For example, CNCs were used as bio templates to synthesize mesoporous films as a way to enhance the surface area and physicochemical properties for the adsorption of Li^{1+} . The mesoporous films template by CNCs demonstrates an increase in the Li^{1+} adsorption capacity with increasing pH from 3 to 7. Moreover, they stated that the acidic nature of the adsorption sites is influenced by the decrease in pH as a result of the ion exchange system and the lower extent of dissociation of functional groups of the mesoporous film (Zheng et al., 2019). Another study by Xu et al. (2020), confirmed that Li^{1+} uptake was less at low pH values. This is also because of the competition of H^{+} and Li^{1+} ions against each other on the active sites of the cellulose microsphere adsorbent.

Therefore, according to the obtained results for Li^{1+} removal, the best pH value is at 6 and 8, but as previously mentioned, at high basic conditions, lithium hydroxides (LiOH) in the solution will tend to form. Thus, it will not be practical to proceed with the

following experiments at such pH value, therefore a more moderate pH value was selected which is 6. The differences between pH 6, 8, and 10 removal efficiencies are not that significant between one another. Lastly, this pH value is more economically feasible and sustainable for the environment since it does not require huge amounts of NaOH or HCl when modifying the pH values. The continuation of the RDP control experiment was also conducted at pH 6 for the same reasons mentioned.

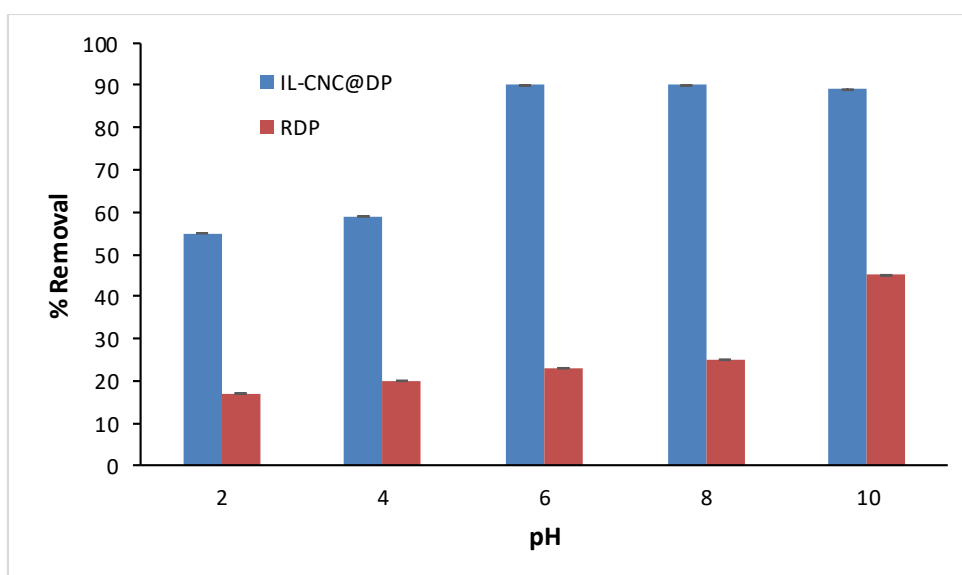


Figure 16. Percentage removal of Li^+ from solution by IL-CNC@DP & RDP at different pH values.

Another pollutant found in the groundwater of Qatar is molybdenum. This metal has mean concentration of 0.053 mg/L (Ahmad et al., 2020). According to Kuiper et al. (2015), this potential source of molybdenum could be due to the industrial activities of oil and gas processing plants since it is used as a catalyst for the desulfurization reaction. In general, molybdenum levels in drinking water do not exceed 0.01 mg/L,

nevertheless, in areas near industrial and mining operations, they tend to exceed as high as 0.2 mg/L. The problem with this metal is the fact that water-drinking treatments cannot be performed by conventional processes; therefore, it requires specific treatments such as ion exchange (WHO, 2003). Thus, as far as now, molybdenum removal studies are few, hence it is important to find ways that are cost-effective and sustainable in order to remove and recover this metal other than ion exchange. Therefore, a recent study demonstrated a low-cost adsorbent by using chitosan to effectively remove molybdenum (Brion-Roby et al., 2018). Furthermore, another study used magnetic nano-adsorption to remove Mo^{6+} efficiently from contaminated water (Chao et al., 2020). Consequently, the adsorption of nanomaterials can be considered an efficient treatment in this case. Hence, the adsorption of Mo^{6+} by modified adsorbent using nanocrystals can be employed. The same experiment is done for Mo^{6+} . The pH was tested at five different values and adjusted using either 1 M HCl or 1 M NaOH solution. The adjusted pH was then used to study the adsorption of Mo^{6+} . Figure 17 illustrates the percentage removal of solute from the aqueous solution by the modified IL-CNC@DP & unmodified RDP adsorbent that was used as control. This can also provide an idea about the adsorption mechanism and efficiency in the removal process so that treatment of groundwater in Qatar can be applied on larger scales.

Some studies proved that IL could be used as extractants for Mo^{6+} from aqueous solutions using IL as diluents (Quijada-Maldonado, 2018; 2017). On the other hand, the extraction of Mo^{6+} can be also performed using diluted and undiluted sulfate IL (Raiguel et al., 2019). In this study, the IL are not used as extractants, they are used as a supporting material that can help with the binding of the extracted CNCs and RDP. As mentioned previously, the adsorption capacity, stability, and interaction will be enhanced when RDP are modified to adsorb Mo^{6+} . Consequently, in this work, the adsorption of Mo^{6+}

onto IL-CNC@DP was studied by analyzing the first parameter, which is solution pH. Molybdenum has several oxidation states that are found as a protonated form in an aqueous solution (Reedijk & Poeppelmeier, 2013). At lower pH values, the H^+ ions tend to compete with the metal ions on the surface of active sites of the adsorbent. Therefore, as previously mentioned, the removal percentage will decline. The increase in the pH value demonstrated an increase in the removal capacity of Mo^{6+} by both adsorbents; IL-CNC@DP and RDP. The results of the modified adsorbent follow a trend, where it shows as the pH value increases from 2 to 10, the adsorption also increases. The same trend is also found in the adsorption of Li^+ ions. The lowest adsorption is shown at pH 2, which was found at 51% for IL-CNC@DP. The highest percentage removal was found to be at pH 6, 8, and 10 at 84%. As discussed earlier, this is explained by the fact that at a low pH value there exist many H^+ ions that competes with the protonated Mo^{6+} for the active sites on the negatively modified adsorbent. Therefore, this will cause lower adsorption for low pH values. Additionally, at pH 4, the percentage removal to some extent increased as the competing behavior in the solution decreased, which allowed the adsorption to be improved. On the other hand, the rest of the pH values demonstrated a significant increase in the efficiency removal due to the electrostatic attraction forces and hydrogen bonding between the protonated Mo^{6+} and the less protonated IL-CNC@DP adsorbent surface. The concept of "faked" adsorption is demonstrated in the case of more basic pH values at 8 & 10 since more OH^- ions are found in the solution, which will promote molybdenum hydroxide precipitation. Hence, high pH values such as 8 & 10 cannot be considered for the upcoming experiments. As for the control adsorbent (RDP), it presents similar trends that are observed by the modified adsorbent (IL-CNC@DP). Furthermore, the adsorption of Li^+ ions onto RDP demonstrates almost identical trends but the removal

capacity was much less in comparison to the Mo^{6+} adsorption. In other words, at pH 2 the percentage of solute removal was found at 52%, and at pH 8, the highest percentage of solute removal was at 69%. This can indicate how the modification performed onto RDP is significant in order to increase the percentage removal of Mo^{6+} ions.

Thus, according to the obtained results for Mo^{6+} removal, the best pH value is at 6, 8, and 10 since the removal efficiencies are not that significant between one another, thus the pH value of 6 was selected for both adsorbents for the same reasons mentioned previously. Moreover, this pH was found to be suitable since usually, the treatment of industrial wastewaters for molybdenum removal is around a pH value of 7 (Brion-Roby et al., 2018). Therefore, the development of an inexpensive and efficient adsorbent the removal of molybdate ions at nearly neutral pH is essential. It is also worth mentioning that the previous experiment of adsorption of Li^{1+} had better removal efficiencies in comparison to Mo^{6+} . In other words, the optimum pH value for the removal of Li^{1+} was found to be at pH 6 and 8 at 90%, while for Mo^{6+} was found to be at pH 6, 8, & 10 at 84% for IL-CNC@DP. On the other hand, for the unmodified adsorbent (RDP), the best pH value for the elimination of Li^{1+} was found to be at pH 10 at 45%, while for Mo^{6+} was found to be at pH 8 at 69%. This can indicate that the modified adsorbent (IL-CNC@DP) is slightly more favorable towards Li^{1+} than Mo^{6+} . Furthermore, the unmodified adsorbent (RDP) is much more favorable towards Mo^{6+} than Li^{1+} .

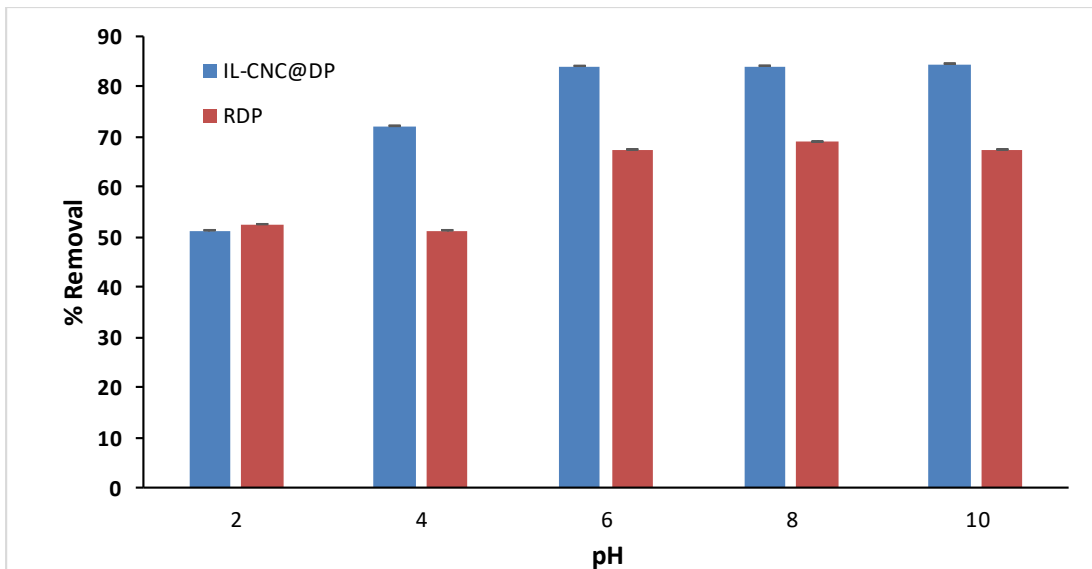


Figure 17. Percentage removal of Mo^{6+} from solution by IL-CNC@DP & RDP at different pH values.

The final pollutant investigated in this study is boron. Boron has a mean concentration of 1.88 mg/L in Qatar's groundwater exceeding the permissible limits of WHO, GSO, and Qatar drinking water (Ahmad et al., 2020). Moreover, the availability of boron in groundwater systems used for drinking and irrigation purposes could pose a risk to individuals. Regardless, boron is still a vital trace element that is essential for typical plant growth (Guan et al., 2016). Nevertheless, there is a fine line between finding boron in trace quantities and having it reach high levels of toxicity. Therefore, the adsorption process could be the answer to remove and remediate boron from aqueous solutions. For example, Köse et al. (2011) used activated carbon prepared from olive bagasse to remove boron from aqueous solutions. As previously mentioned, activated carbon is an expensive yet effective method to be used as an adsorbent. Therefore, this study relies on a modified low-cost adsorbent using nanocrystals for the effective removal of B^{3+} metals. Based on a previous study, it is proven that cellulose extracted from walnut shells can be employed for chemical modification for the selective

adsorbent of B^{3+} metals (Sarsenov et al., 2018). Moreover, nanoscale cellulose such as cellulose nanocrystals and gum arabic conjugates in crosslinked membranes were recently seen as an innovative method for B^{3+} removal (Asim et al., 2018). In addition to CNC, there are studies that also supported the usage of IL for the removal of B^{3+} metals. Glucaminium-based ionic liquids were applied to remove B^{3+} from water (Joshi et al., 2012). Moreover, supported liquid membranes (SLM) for the extraction of B^{3+} is presented by Coll et al. (2014). Hence, CNC extracted from the cellulose of RDP is used in this study, along with the already prepared IL. The same experiment is performed for B^{3+} . The pH was tested at five different values and adjusted using either 1 M HCl or 1 M NaOH solution. The adjusted pH was then used to study the effect of pH on the adsorption of B^{3+} . Figure 18 demonstrates the percentage removal of solute from B^{3+} solution by the modified IL-CNC@DP & unmodified RDP adsorbent. The results can offer knowledge regarding the efficiency in the removal process of B^{3+} metals to treat groundwater systems in Qatar.

As discussed formerly, the modification made onto RDP to adsorb B^{3+} will be discussed through studying the first parameter, which is the effect of pH. It can be concluded that the increase in the pH value demonstrates an increase in the removal capacity of B^{3+} by both adsorbents; IL-CNC@DP and RDP. The results of the modified and unmodified adsorbents follow a trend, where it shows as the pH value increases from 2 to 10, the adsorption of B^{3+} also increases. The same trend is also found in the adsorption of Li^{1+} and Mo^{6+} metals. The lowest adsorption is shown at pH 2, which was found at 77%. The highest percentage removal was found to be at pH 6, 8, and 10 at 98%. The lower adsorption found at low pH values is due to the protonated B^{3+} metals and H^{+} ions as they compete on the negative surface of IL-CNC@DP. The competing behavior tends to decrease as the pH value increases since more OH^{-} ions are found in the solution,

therefore an increase in percentage removal of B^{3+} metals is shown at 6, 8, and 10 pH values. However, the concept of "faked" adsorption should be considered when studying the effect of pH since at more basic pH values more OH^- ions are found in the solution, which will encourage hydroxide precipitation of boron metals. Therefore, high pH values are not reliable to be considered for the upcoming experiments. As for the control unmodified adsorbent (RDP), the removal capacity was much less in comparison to the modified adsorbent. In other words, at pH 2 the percentage of solute removal was found at 50%, and at pH 10, the highest percentage of solute removal was at 63%. This proves how the modification performed onto RDP is momentous in order to increase the percentage removal of B^{3+} ions.

Consequently, according to the obtained results for B^{3+} removal, the best pH value was at 6, 8, and 10 and since the percentages of removal are similar, so pH value of 6 was selected for IL-CNC@DP adsorbent. This is also presented by a study where the maximum boron removal was obtained at a pH value of 5.5 using a modified adsorbent (Köse et al., 2011). As for RDP, even though a pH value of 10 demonstrates the highest removal efficiency, the pH value of 4 was selected since the lower pH values are not that significant between one another. This can also discard the concept of "faked" adsorption.

Comparing these findings with the other results for the effect of pH for IL-CNC@DP, it can be concluded that Li^{1+} and B^{3+} , at pH of 6, had the best removal efficiencies of 90% and higher, on other hand, Mo^{6+} , at pH of 6, had removal efficiencies of 84%. As for RDP, as discussed previously, the ideal pH value for Li^{1+} was found to be at pH 10 at 45%, while for Mo^{6+} was found to be at pH 8 at 69%, and for B^{3+} at pH 10 at 63%. This can conclude that IL-CNC@DP is slightly more favorable towards Li^{1+} and B^{3+} than Mo^{6+} and that RDP is much more favorable towards Mo^{6+} and B^{3+} than Li^{1+} ,

making B^{3+} metal the most favorable pollutant towards both adsorbents. Furthermore, this can depend upon the different mechanisms of adsorption of metals according to their physicochemical properties, as explained in section 4.2.

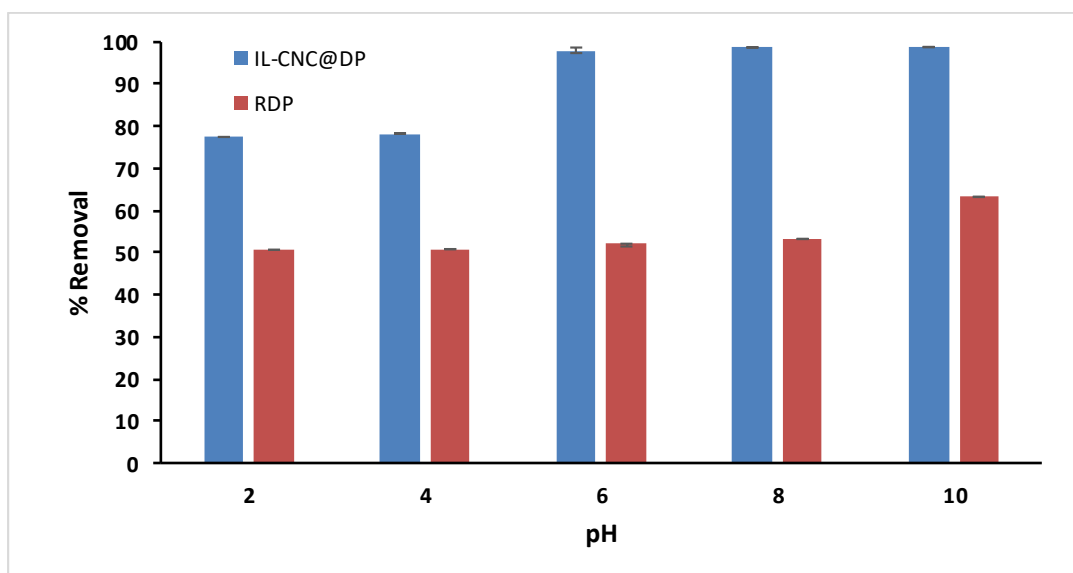


Figure 18. Percentage removal of B^{3+} from solution by IL-CNC@DP & RDP at different pH values.

4.4 Effect of initial Li^{1+} , Mo^{6+} , & B^{3+} concentration on the adsorption process

Understanding the effect of metal concentrations on the adsorption capacities of adsorbents is also essential for metal recovery. Keeping in mind that the concentration of the targeted metal impacts the efficiency, capacity, and adsorption mechanism in a solution (Zhuang and Wang, 2019). Moreover, it is important to mention that breaking down the adsorbent into smaller particles tends to open the sealed channels on the adsorbent; hence, the adsorption rate will tend to increase. Therefore, in this study smaller particle sizes of the adsorbent that ranged from 0.125 mm - 0.250 mm were used. Furthermore, most studies correlated the practicality of using cellulose nanofibrils (CNF) as adsorbents for metal ions, and only a few studies reported on CNCs (Mahfoudhi & Boufi, 2017). Hence, this study presents a modified RDP using IL and CNC for the enhancement of the surface area and adsorption capacity.

The groundwater quality was found to be deteriorated due to the presence of Li^{1+} ions that exceed the permissible limits. According to the ICP-OES results of the collected groundwater samples, the Li^{1+} concentrations were 0.120 mg/L therefore providing an adsorbent that can recover the metal is one of the aims of this study. Figure 19 illustrates the adsorption capacity for Li^{1+} onto IL-CNC@DP & RDP at multiple concentrations. The metal concentrations that were used with an optimum pH value of 6 for both adsorbents present a general trend in results. The steady constant increase of adsorption capacity with the increasing Li^{1+} concentrations is evident for both adsorbents. It is apparent that the adsorption capacity of IL-CNC@DP is the highest in comparison to RDP. This is also confirmed by the previous results that present the adsorption efficiency of Li^{1+} at several pH values was the highest for IL-CNC@DP in contrast to RDP. It is important to mention that nanocellulose composites are significant adsorbents that can be used to adsorb many classes of pollutants including metals (Tao

et al., 2020; Mahfoudhi & Boufi, 2017). Therefore, the modification made onto the RDP, where IL was used as a linkage between the surface of the RDP and the CNC promoted better and enhanced removal percentages. It can be clear that the adsorption capacity of Li^{1+} onto IL-CNC@DP presented a steady increase overall the concentrations used. Nonetheless, the adsorption capacity onto RDP was much less under the same concentrations used. According to Hilal et al. (2012), the removal efficiency increased as the concentration increased for Cu^{2+} and Cd^{2+} metal ions. This is due to the overall mass transfer driving force. Therefore, in this study, the constant increase in the adsorption capacity along with the increase in concentration is directly linked to the increase in metal mass transfer onto the adsorbent's surface of the CNC. The modified adsorbent proved that adsorption was highest at high initial concentrations due to the increase in metal mass transfer and collision between the ions and the active binding sites (Manirethan et al., 2019). Furthermore, the enhancement of the adsorption capacity of the modified adsorbent with an increase in the initial concentration of metal ions is due to the increased diffusion of the metal (Samra et al., 2014). A better illustration is found in Figure 15. In other words, the internal diffusion of the ions to the pores of the adsorbent is one of the driving forces that enhance the adsorption capacities (Girish & Murty, 2016). To sum up, the modified adsorbent IL-CNC@DP had a better mass transfer, collision, and diffusion, which resulted in enhanced adsorption capacity in comparison to RDP.

To be more specific, the adsorption capacity (q_e) delivers information about the amount of ions adsorbed per gram of adsorbate at equilibrium (mg/g). Therefore, the adsorption capacities for the adsorption of Li^{1+} onto IL-CNC@DP were found to be 4.47, 9.40, 14.34, 19.29, 24.25, 29.22, 34.21, 49.19, 69.18, and 99.17 mg/g for Li^{1+} metal concentrations of 5, 10, 15, 20, 25, 30, 35, 50, 70, and 100 mg/L, respectively. On the

other hand, the adsorption capacities for the adsorption of Li^{1+} onto RDP were found to be 0.59, 1.64, 2.57, 4.65, 6.26, 9.60, 13.73, 20.93, 31.38, and 53.02 mg/g for Li^{1+} metal concentrations of 5, 10, 15, 20, 25, 30, 35, 50, 70, and 100 mg/L, respectively. The high adsorptive capacity of IL-CNC@DP towards Li^{1+} was more prominent at high Li^{1+} initial concentrations due to the fact that more binding sites were available at high metal concentrations that promoted better filling inside the pores of the adsorbent surface. Furthermore, studies by Al-Ghouti et al. (2019 & 2017) demonstrated that the adsorption increased with the increase in concentration because of collision and enhance mass transfer forces between the metal ions and the adsorbent itself. Also relying on the adsorption capacity concept, the adsorption mechanisms through adsorption isotherm models will be presented later on.

In this study, concentrations above 100 mg/L for IL-CNC@DP were not employed since the adsorption capacity of Li^{1+} reached 99 mg/g with 99% adsorption efficiency at 100 mg/L of initial metal concentration. It reached equilibrium due to the increase in metal concentrations that facilitated the mass transfer driving force that increased the adsorption onto the CNC available surface-active sites. Nevertheless, it is expected that the adsorbent eventually will have limited available active sites; therefore, the adsorption capacity will reach a plateau (Jiang et al., 2020). It is also important to mention that the higher adsorption capacity of IL-CNC@DP in comparison to RDP could be attributed to the adsorbents' characteristics. This means that the characterization of the adsorbent can enhance the selectivity of any pollutant. In this study, the BET results that were obtained demonstrated that the RDP adsorbent had a specific surface area of 2.126 m^2/g with a pore volume of 0.008611 cm^3/g . After modification, the specific surface area of the IL-CNC@DP adsorbent was found to be 4.254 m^2/g with a pore volume of 0.015527 cm^3/g . Therefore, such characterization

proves why Li^{1+} favors adsorption onto the surface of IL-CNC@DP more than RDP since it has higher pore volume and surface, which provides more active binding sites; therefore, more adsorption towards Li^{1+} . This is also supported by the SEM results of Figures 5A–C, where the surface of IL-CNC@DP contains more pores and dents in comparison to the smoother surface of RDP.

The adsorption of Li^{1+} can reach its all-time high at 99 mg/g at 100 mg/L by using the modified adsorbent. Researchers can have the choice of either relying on the modified adsorbent for optimum Li^{1+} removal for remediation and recovery purposes or they could utilize RDP at high concentrations for limited pollutant removal.

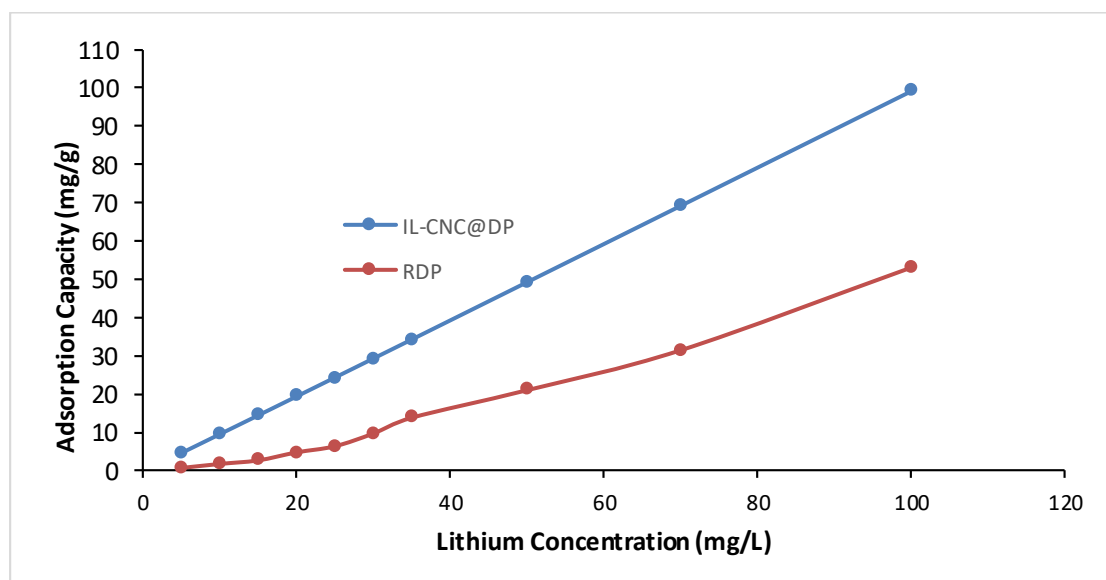


Figure 19. Effect of initial concentration on the IL-CNC@DP & RDP at different concentrations on Li^{1+} adsorption.

As discussed earlier, another pollutant that was found to exceed the permissible limits is molybdenum (Mo). Therefore, this study is to understand the adsorption capacity of Mo^{6+} onto both adsorbents as a way to recover this metal. Figure 20 demonstrates the adsorption capacity for Mo^{6+} onto IL-CNC@DP & RDP at multiple concentrations. A general trend was observed for the Mo^{6+} concentrations that were studied at an optimum pH value of 6 for both adsorbents. It is evident that there is a steady increase in adsorption capacity along with the increase in Mo^{6+} concentrations for both adsorbents. In addition, the adsorption capacity of IL-CNC@DP is the highest in comparison to RDP for Mo^{6+} adsorption and these results are similar to the ones obtained by Li^{1+} adsorption. It is important to point that the results are also confirmed by the percentage removal of Mo^{6+} at several pH values was the highest for IL-CNC@DP in contrast to RDP. As discussed earlier, the modification performed by CNC promoted better and enhanced removal percentages and that IL was used to bind or link the surface of the RDP and the CNC together. This can enhance and optimize the removal of the pollutant, such as heavy metals, from the environment. This is why it can be clear that the adsorption capacity of Mo^{6+} onto IL-CNC@DP presented a steady increase overall the concentrations used, whereas the adsorption capacity onto RDP was less under the same Mo^{6+} concentrations used. This is due to the overall mass transfer driving force of the Mo^{6+} metal. In other words, the increase in the adsorption capacity along with the increase in concentration is due to the increase in metal mass transfer onto the adsorbent's surface of the CNC. Furthermore, at high initial concentrations, the collision between the metals and the active binding sites of the adsorbent occurs along with an increase in the diffusion of the solute to the pores of the adsorbent. Hence, the modified adsorbent IL-CNC@DP had a better mass transfer, collision, and diffusion of the Mo^{6+} metal that enhanced the adsorption capacity in comparison to RDP.

The adsorption capacities for the adsorption of Mo^{6+} onto IL-CNC@DP were found to be 4.69, 9.67, 14.38, 19.53, 24.54, 29.44, 34.48, 49.62, 69.55, and 88.42 mg/g for Mo^{6+} metal concentrations of 5, 10, 15, 20, 25, 30, 35, 50, 70, and 100 mg/L, respectively. However, the adsorption capacities for the adsorption of Mo^{6+} onto RDP were found to be 0.36, 0.93, 1.72, 4.45, 7.13, 11.28, 14.91, 25.54, 39.71, and 61.49 mg/g for Mo^{6+} metal concentrations of 5, 10, 15, 20, 25, 30, 35, 50, 70, and 100 mg/L, respectively. It is obvious that the high adsorptive capacity of Mo^{6+} onto IL-CNC@DP is significant at high initial Mo^{6+} concentrations. As previously discussed, this is due to the fact that more binding sites were available at high metal concentrations that promoted better filling inside the pores of the adsorbent surface. For this study, the highest adsorption capacity at 100 mg/L for IL-CNC@DP reached 89 mg/g with 89% adsorption efficiency. Since it did not reach the adsorption capacity of Li^{1+} at 99 mg/g, then perhaps this study did not reach equilibrium and the adsorption capacity can still increase as the initial concentrations increases until it reaches around 99 mg/g. Although, another reason could be attributed to the adsorbent itself since it has limited available active sites on the adsorbent's surface until it reaches a plateau.

The higher adsorption capacity also depends on the adsorbent's characteristics such as the previously mentioned BET and SEM results. Moreover, this is why Mo^{6+} favors adsorption onto the modified adsorbent more than the unmodified adsorbent since it has higher pore volume and surface, which provides more active binding sites. All in all, the adsorption of Mo^{6+} can reach its all-time high at 89 mg/g at 100 mg/L by using the modified adsorbent, as for the unmodified adsorbent it reaches 61 mg/g at 100 mg/L. In this case, depending upon the accessibility of resources and the amount of metal pollutant available, the removal of Mo^{6+} ions can be performed by either. Lastly, if researchers are utilizing unmodified adsorbents, such as RDP, then it is more favorable

towards Mo^{6+} than Li^{1+} , whereas if they are considering a more enhanced and modified adsorbent, then it is more favorable towards Li^{1+} than Mo^{6+} at 100 mg/L of initial metal concentration.

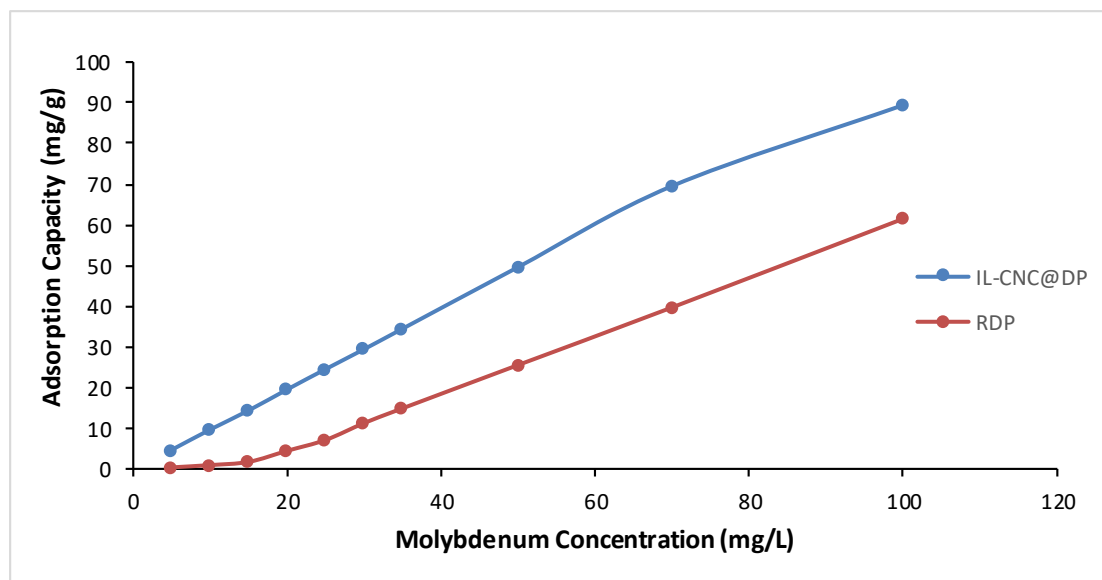


Figure 20. Effect of initial concentration on the IL-CNC@DP & RDP at different concentrations on Mo^{6+} adsorption.

Figure 21 demonstrates the adsorption capacity for B^{3+} onto IL-CNC@DP & RDP at multiple concentrations. A general trend is found for the B^{3+} concentrations that were studied at an optimum pH value of 6 for IL-CNC@DP and a pH value of 4 for RDP. It is apparent that there is a steady increase in adsorption capacity along with the increase in B^{3+} concentrations for both adsorbents. The adsorption capacity of IL-CNC@DP is the highest in comparison to RDP for B^{3+} adsorption and these results are similar to the ones obtained by Li^{1+} and Mo^{6+} adsorption. Moreover, these findings are also consistent with the ones obtained for the percentage removal of B^{3+} at several pH values since it

also shows that IL-CNC@DP is the highest in contrast to RDP. The reason is due to the modification made onto RDP by using CNC and IL. Because it can be clear that the adsorption capacity of B^{3+} onto IL-CNC@DP was significantly enhanced and improved, whereas, under the same experimental conditions, the adsorption capacity onto RDP was much less. It is worth mentioning that the overall mass transfer driving force of B^{3+} metals plays a major role as it provides better adsorption capacity at high initial concentrations. As initial concentration increases, collision and diffusion of the B^{3+} metal and the surface of the adsorbent occurs, therefore the adsorption capacity increases. Thus, the modified adsorbent IL-CNC@DP had a better mass transfer, collision, and diffusion of the B^{3+} metal that enhanced the adsorption capacity in contrast to RDP.

The adsorption capacities for the adsorption of B^{3+} onto IL-CNC@DP were found to be 4.50, 9.19, 13.88, 19.00, 24.13, 29.11, 34.02, 48.27, 68.17, and 97.60 mg/g for B^{3+} metal concentrations of 5, 10, 15, 20, 25, 30, 35, 50, 70, and 100 mg/L, respectively. Nevertheless, the adsorption capacities for the adsorption of B^{3+} onto RDP were found to be 0.44, 1.58, 4.36, 6.50, 13.12, 16.24, 20.24, 31.13, 43.67, and 65.56 mg/g for B^{3+} metal concentrations of 5, 10, 15, 20, 25, 30, 35, 50, 70, and 100 mg/L, respectively. These results prove that the high adsorptive capacity of B^{3+} onto IL-CNC@DP is significant at high initial B^{3+} concentrations. As formerly stated from the previous two experiments (Li^{1+} & Mo^{6+}), this is due to the fact that more binding sites were available at high B^{3+} metal concentrations that encouraged better filling inside the pores of the adsorbent surface. In this study, the highest adsorption capacity at 100 mg/L for IL-CNC@DP reached 97 mg/g with 97% adsorption efficiency. It is probable that the adsorbent will eventually reach a plateau as the limited available sites are used.

Furthermore, the adsorbent's characteristics such as the previously mentioned BET and

SEM results are highly dependent upon the enhancement of adsorption capacity.

This is why B^{3+} favors adsorption onto the modified adsorbent more than the unmodified adsorbent since it has higher pore volume and surface, which provides more active binding sites. Nevertheless, the unmodified adsorbent reaches its all-time high at 65 mg/g at 100 mg/L, therefore, B^{3+} can still be remediated from the environment using the RDP. Comparing the adsorption capacities of Li^{1+} , Mo^{6+} , & B^{3+} , it can be concluded that $Li^{1+} > B^{3+} > Mo^{6+}$ for IL-CNC@DP and $B^{3+} > Mo^{6+} > Li^{1+}$ for RDP at 100 mg/L of initial metal concentration.

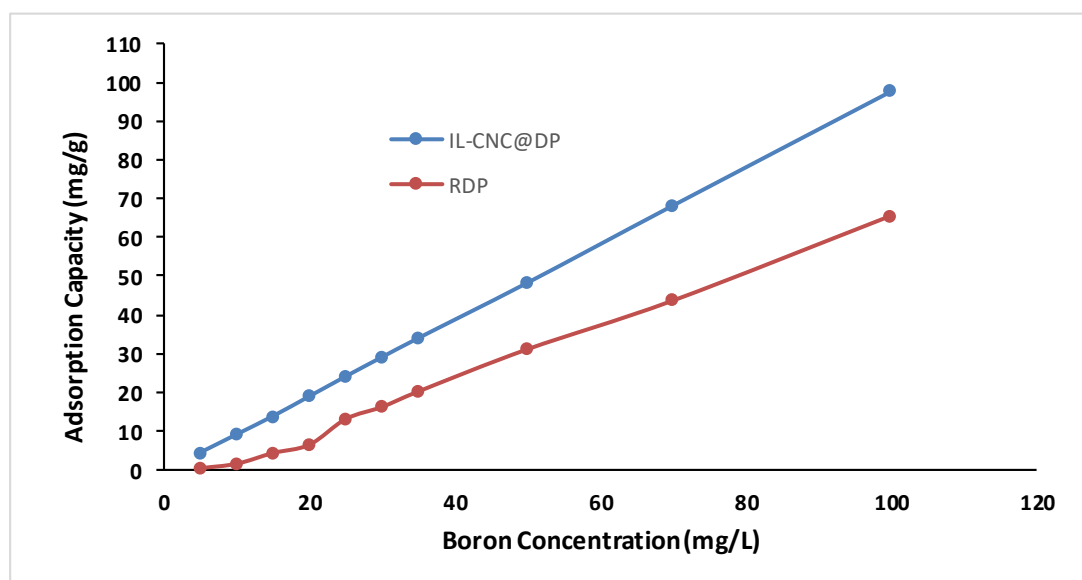


Figure 21. Effect of initial concentration on the IL-CNC@DP & RDP at different concentrations on B^{3+} adsorption.

4.5 Effect of temperature on adsorption of Li^{1+} , Mo^{6+} , & B^{3+} and thermodynamics.

Another important parameter in any adsorption process is temperature. Any batch adsorption process depends greatly on the surrounding temperature. In general, there exist two methods of activation for an adsorbent: chemical and physical. The chemical activation includes treatment of the adsorbent with chemicals. This method was done by modifying the adsorbent with IL and CNC. On the other hand, the physical activation was done by using three different temperatures, where 25°C mimics the room temperature surroundings and 35 and 45°C are high temperatures that require more input of energy and cost (Heibati et al., 2015). This means that exothermic and endothermic nature adsorption processes exist depending on the temperature used. Therefore, it is important to know exactly what optimum temperature to use in order to recover metals from water processes for maximum adsorption capacity.

The effects of temperatures on Li^{1+} adsorption onto IL-CNC@DP & RDP were investigated at different temperatures and the results are shown in Figure 22 (A & B). Figure 22A shows a linear increase of Li^{1+} adsorption onto IL-CNC@DP with increasing initial concentrations as it directs the accessibility of several active sites as the Li^{1+} concentration increases. It is evident that when the adsorption process was conducted at 25 °C, 35 °C, and 45 °C, the amount of Li^{1+} being adsorbed did not fluctuate much and that the effect of temperature did not contribute as a major factor in this study. However, there is an increase in the adsorption capacity and efficiency as the temperature increases, but the differences between the temperatures are insignificant. These findings are noteworthy since the increase in temperature requires more energy and cost, therefore room temperature experiments are more practical and affordable. Moreover, this means that the modified adsorbent is effective enough to be

physically active at low temperatures rather than utilizing high temperatures. Despite that recent findings validate that the effect of the temperature factor does in fact contribute to the adsorption capacity (Al-Ghouti & Al-Absi, 2020; Al-Ghouti & Da'ana, 2020; Al-Ghouti et al., 2019). In this study, the temperature factor did not play a significant role in the modified adsorbent. Regardless, analysis of variance (ANOVA) was used to assess the significance of the results in this study. A two-factor ANOVA test was conducted and the results of Li^{1+} onto IL-CNC@DP show a significant difference at a p-value of 0.03, but experimentally the results are not significant.

Therefore the results show that the adsorption capacity of Li^{1+} at 5 mg/L onto IL-CNC@DP is found to slightly increase from 4.47 mg/g (89.46%) at 25 °C to 4.50 mg/g (90.06%) at 35 °C to 4.54 mg/g (90.96%) at 45 °C. By comparing these results to the adsorption capacity of Li^{1+} at 100 mg/L, it was found that it also increases slightly from 99.1 mg/g (99.17%) at 25 °C to 99.2 mg/g (99.23%) at 35 °C to 99.2 mg/g (99.25%) at 45 °C. This indicates the availability of active sites on the surface of the adsorbent at increasing initial concentrations. Therefore, water treatment processes that are concentrated with Li^{1+} can be recovered at low temperatures using IL-CNC@DP at high initial concentrations for optimum and maximum recovery of Li^{1+} . While on the other hand, Figure 22B shows a linear increase of Li^{1+} adsorption onto RDP with increasing initial concentrations, but fluctuations are demonstrated under the three different temperatures. The adsorption capacity of Li^{1+} at 5 mg/L onto RDP is found to decrease from 0.58 mg/g (11.71%) at 25 °C to 0.51 mg/g (10.32%) at 35 °C to 0.32 mg/g (6.57%) at 45 °C. This trend of decreasing with increasing temperatures is shown up until initial concentrations of 15 mg/L and then the trend started to show other variations. One constant result was observed for RDP was that at initial concentrations of 20 until 70 mg/L, the optimum adsorption capacity was found at 35 °C. Later, it showed a constant

trend of increasing that indicates the incapability of the molecules to naturally adhere on the surface of the RDP adsorbent due to the presence of few available active sites. Similar results are shown by a recent study by Al-Ghouti et al. (2019), where the adsorption of mercury at 25 °C increased with increasing concentrations, but at 35 °C and 45 °C, the adsorption started to show fluctuating trends of increasing and decreasing. In this study, at 100 mg/L, the optimum temperature was found to be 45 °C, although at 35 °C the adsorption capacity is still high. Overall, it can be concluded that moderate temperature is more favored by the adsorption process onto RDP. Besides, the statistical analysis results of Li^{1+} onto RDP show a significant difference at a p-value of 3×10^{-8} .

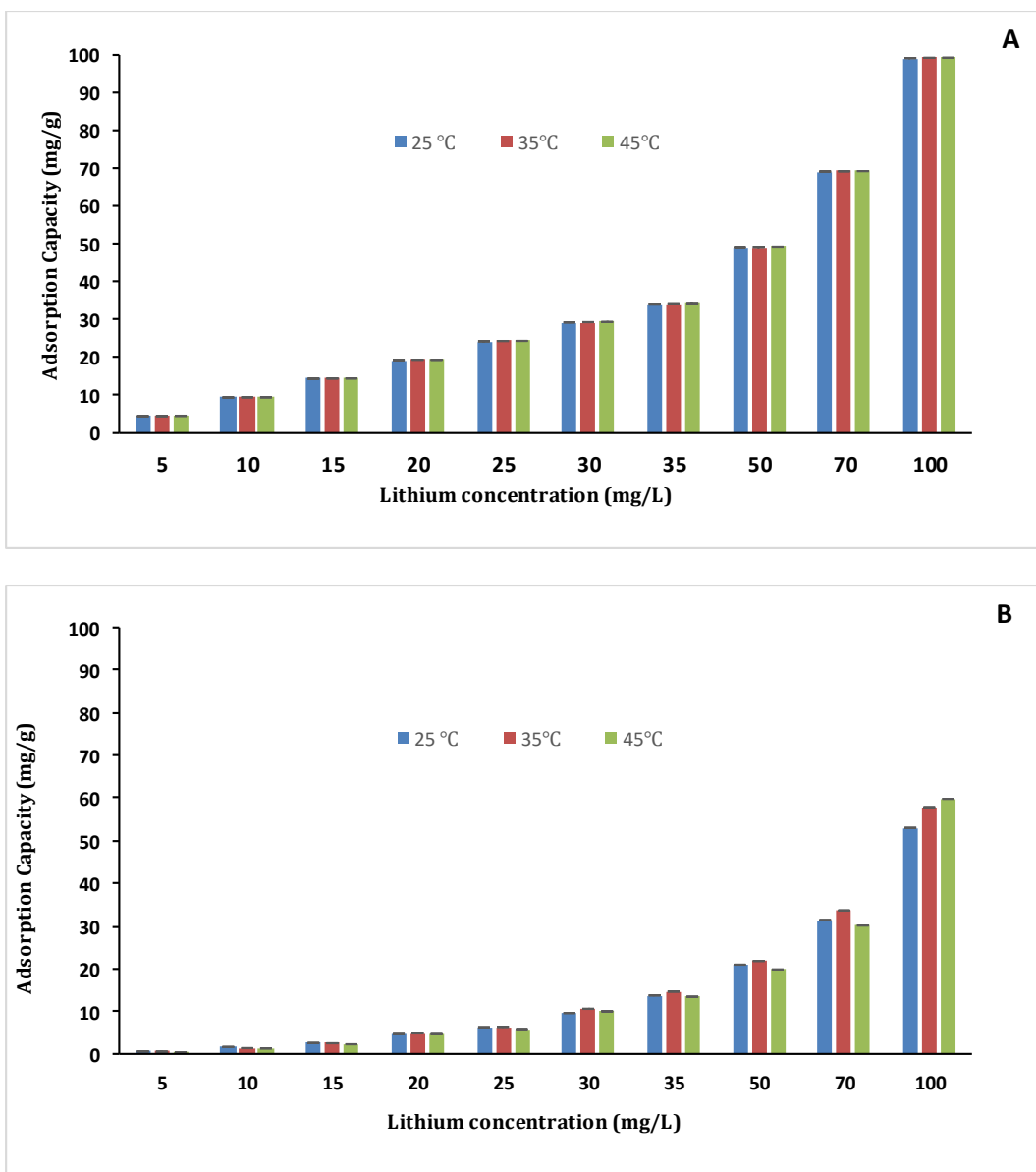


Figure 22. Effect of temperature on the IL-CNC@DP (A) & RDP (B) at different concentrations on Li^{1+} adsorption.

Based on the obtained results, thermodynamics calculations were analyzed for both adsorbents at 25, 35, and 45 °C. This was performed in order to understand the behavior of the reactions that took place under different temperatures. From Table 11, the values of ΔG° are found to have a negative value throughout all the experiments, indicating that the adsorption of Li^{1+} onto IL-CNC@DP & RDP is feasible, spontaneous, and do

not need an external driver for the reaction to take place. Similarly, the negative value of ΔH° for all the experiments indicates that the reactions were exothermic. Lastly, the negative value of ΔS° confirmed that the adsorption of Li^{1+} on the surface of the adsorbents is an associated mechanism (Al-Ghouti et al., 2019; Imran Din et al., 2013). The calculation of the thermodynamics at 25°C, 35°C, and 45 °C was carried out based on the previously mentioned equations (6) and (7), where the Li^{1+} concentrations varied. Furthermore, the equation of the line for enthalpy and entropy determination is demonstrated in Figure 26. The ΔG° values for the modified adsorbent IL-CNC@DP were -11.21 kJ/mol, -9.08.11 kJ/mol, and - 6.96 kJ/mol at 25 °C, 35 °C, and 45 °C, respectively. According to the negative values obtained for Gibbs free energy, it can be concluded that the adsorption of Li^{1+} onto IL-CNC@DP was spontaneous at all the studied temperatures. While the values of ΔH° and ΔS° were -74.57 kJ/mol and - 0.21 kJ/mol, respectively. The ΔH° verifies the previous results of the effect of temperature on the adsorption of Li^{1+} onto IL-CNC@DP, where utilization of different temperatures did not have an effect on the adsorption process. As for ΔS° results, it does not favor the high level of disorder in the adsorption process. For the unmodified adsorbent RDP, the ΔG° values were -12.25 kJ/mol, -11.11 kJ/mol, and -9.98 kJ/mol at 25 °C, 35 °C, and 45 °C, respectively. The values of ΔH° and ΔS° were -46.05 kJ/mol and -0.11 kJ/mol, respectively.

Table 11. Thermodynamic parameters for Li^{1+} adsorption onto IL-CNC@DP & RDP.

Adsorbent	Temperature (°C)	$\ln(K_L)$	ΔG° (kJ/mol)	ΔH° (kJ/mol)	ΔS° (kJ/mol)
IL-CNC@DP	25	4.46	-11.21	-74.57	-0.21
	35	3.67	-9.08		
	45	2.57	-6.96		

RDP	25	5.14	-12.25	-46.05	-0.11
	35	3.93	-11.11		
	45	3.98	-9.98		

Further experiments were performed on Mo^{6+} adsorption by understanding the optimum temperature in order to recover this metal from water processes under maximum adsorption capacity. The effects of temperatures on Mo^{6+} adsorption onto IL-CNC@DP & RDP were investigated at different temperatures and the results are illustrated in Figure 23. Figure 23A displays a linear increase of Mo^{6+} adsorption onto IL-CNC@DP with increasing initial concentrations due to the availability of multiple active sites on the modified adsorbent's surface as the Mo^{6+} concentration increases. Although comparing the reaction under 25 °C, 35 °C, and 45 °C, the amount of Mo^{6+} adsorbed by IL-CNC@DP did not vary. This study can confirm that the effect of a variety of temperatures was not a significant factor for the modified adsorbent. Nonetheless, there is still a fluctuation in the adsorption capacity as the temperature increases, but the differences are trivial. On the other hand, the removal of Mo^{6+} onto IL-CNC@DP displays a significant difference at a p-value of 5×10^{-5} , but experimentally the results are not significant. The results are similar to Li^{1+} adsorption; therefore, proving that the modified adsorbent is effective enough to be physically active at low temperatures rather than utilizing high temperatures, regardless of what other studies have found, as previously mentioned.

The finding displays the adsorption capacity of Mo^{6+} at 5 mg/L onto IL-CNC@DP to be 4.69 mg/g (83.81%) at 25 °C then to decrease slightly to 4.471 mg/g (79.43%) at 35 °C and then to increase slightly to 4.476 mg/g (79.53%) at 45 °C. Comparing these

results to the adsorption capacity of Mo^{6+} at 100 mg/L, it was found to be 89.4 mg/g (89.42%) at 25 °C then to decrease slightly to 89.3 mg/g (89.39%) at 35 °C and to remain the same at 89.3 mg/g (89.38%) at 45 °C. Therefore, this indicates the availability of active sites on the surface of the adsorbent at increasing initial concentrations. Hence, at large-scale operations for the removal of Mo^{6+} by the adsorption process, the modified adsorbent (IL-CNC@DP) can be employed at low temperatures such as 25 °C since it demonstrates high adsorption capacities at high initial concentrations. Figure (B) illustrates a linear increase of Mo^{6+} adsorption onto RDP with increasing initial concentrations, but with more obvious variations under the three different temperatures. The results of the removal of Mo^{6+} onto RDP display a significant difference at a p-value of 1×10^{-5} . Moreover, the adsorption capacity of Mo^{6+} at 5 mg/L onto RDP is found to increase from 0.36 mg/g (7.38%) at 25 °C to 0.66 mg/g (13.23%) at 35 °C to 0.88 mg/g (17.69%) at 45 °C. This trend of increasing with increasing temperatures is also presented at initial concentrations of 30 till 100 mg/L. However, at initial concentrations of 10 until 25 mg/L, the adsorption capacity at 35 °C reaches its optimum then decreases at 45 °C. As mentioned previously, this trend of increasing and decreasing adsorption capacities under a variety of temperatures has been proven and it can be seen for Li^{1+} onto RDP. Nonetheless, in this specific study, at 100 mg/L, the optimum temperature was found to be 45 °C. Therefore, it can be concluded that higher temperature is more preferred by the adsorption process onto RDP. It is also important to note that the variations in adsorption capacities between Li^{1+} & Mo^{6+} are significant. Moreover, based on all of the previous experiments, the adsorption of Li^{1+} is more favorable towards IL-CNC@DP adsorbent than Mo^{6+} at higher initial concentrations. Once the temperature factor was introduced, differences between the adsorption capacities of the metals are presented under 25 °C, 35 °C, & 45

°C. In other words, Li^{1+} adsorption at 5 and 100 mg/L onto IL-CNC@DP presents an increasing trend as the temperature increases. On the other hand, Mo^{6+} adsorption at 5 mg/L presents fluctuating trends but at 100 mg/L, it can be increasing towards high temperatures. Nonetheless, comparing Li^{1+} and Mo^{6+} adsorption capacity onto RDP at 5 mg/L, the trend is different, where for Li^{1+} it decreases with increasing temperatures and for Mo^{6+} it is the opposite. On the other hand, at 100 mg/L for Li^{1+} & Mo^{6+} adsorption, it can be shown that as the temperature increases, the adsorption capacity increases.

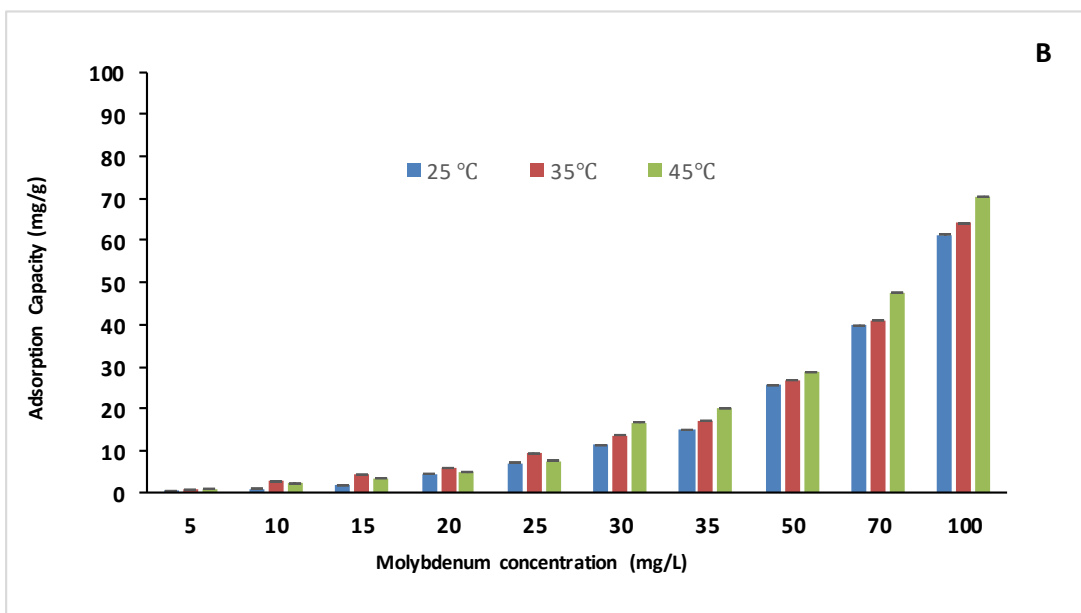
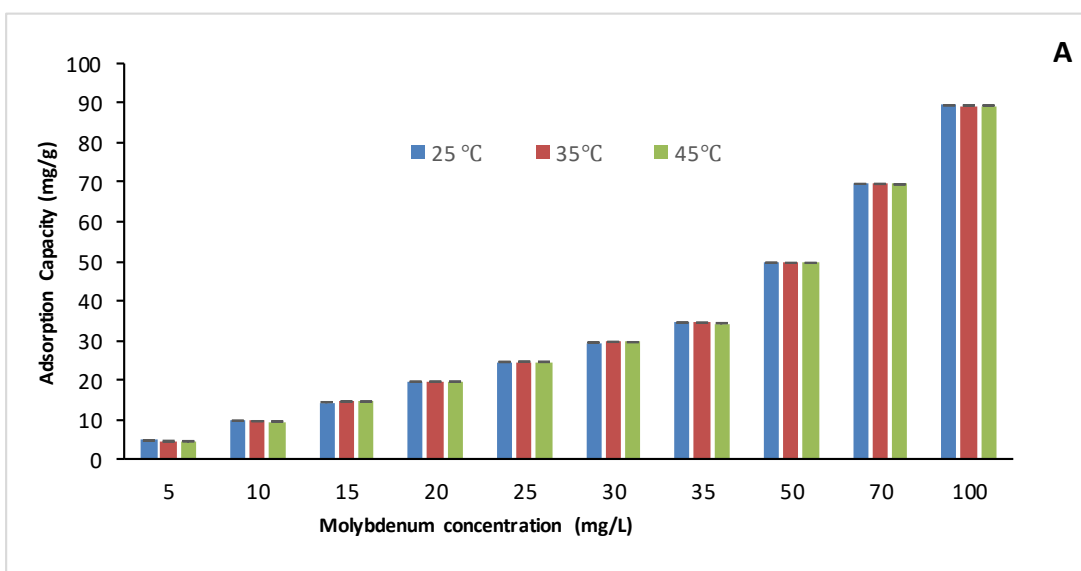


Figure 23. Effect of temperature on the IL-CNC@DP (A) & RDP (B) at different concentrations on Mo^{6+} adsorption.

Similarly, for this experiment, from Table 12, the values of ΔG° are negative for all the temperatures, indicating that the adsorption of Mo^{6+} onto IL-CNC@DP & RDP is feasible, spontaneous, and do not need an external driver for the reaction to take place. Likewise, the negative value of ΔH° for all the experiments indicates that the reactions were exothermic. Whereas the negative value of ΔS° confirmed that the adsorption of Mo^{6+} on the surface of the IL-CNC@DP adsorbent is an associated mechanism, but a positive value is found for RDP adsorbent. To be specific, the ΔG° values for the modified adsorbent IL-CNC@DP were -8.31 kJ/mol, -4.69 kJ/mol, and -1.08 kJ/mol at 25 °C, 35 °C, and 45 °C, respectively. According to the results obtained for Gibbs free energy, it can be concluded that the adsorption of Mo^{6+} onto IL-CNC@DP was spontaneous at all the studied temperatures. The same results can be concluded for the adsorption of Mo^{6+} onto RDP for Gibbs free energy. While the values of ΔH° and ΔS° for IL-CNC@DP were -116.01 kJ/mol and -0.36 kJ/mol, respectively, while for RDP the ΔH° and ΔS° values were -100.03 kJ/mol and 0.37 kJ/mol, respectively. The ΔH° confirms that the effect of temperature on the adsorption of Mo^{6+} onto IL-CNC@DP and RDP did not have a significant effect on the adsorption process. While as for ΔS° results, it does not favor the high level of disorder in the adsorption process of Mo^{6+} onto IL-CNC@DP but for RDP it confirms the high level of disorder. By comparing these results to the Li^{1+} adsorption experiment onto IL-CNC@DP and RDP, it is obvious that Gibbs free energy and enthalpy values are similar in their conclusions under the three studied temperatures. On the other hand, the entropy values for Li^{1+} and

Mo⁶⁺ for IL-CNC@DP are the same (negative value) but when it comes to the unmodified adsorbent, RDP, the conclusions differ since they follow a high level of disorder. The calculation of the thermodynamics was based on the previously mentioned equations (6) and (7).

Table 12. Thermodynamic parameters for Mo⁶⁺ adsorption onto IL-CNC@DP & RDP.

Adsorbent	Temperature (°C)	ln(KL)	ΔG° (kJ/mol)	ΔH° (kJ/mol)	ΔS° (kJ/mol)
IL-CNC@DP	25	3.46	-8.31	-116.01	-0.36
	35	1.44	-4.69		
	45	0.53	-1.08		
RDP	25	3.73	-210.93	-100.03	0.37
	35	7.02	-214.65		
	45	6.23	-218.376		

The last parameter, which is the effect of temperatures on B^{3+} adsorption onto IL-CNC@DP & RDP, is illustrated in Figure 24. Figure 24A displays a linear increase of B^{3+} adsorption onto IL-CNC@DP with increasing initial concentrations. This is due to the availability of multiple active sites present on the modified adsorbent's surface as the B^{3+} concentration increases. Yet, comparing the reaction under 25 °C, 35 °C, and 45 °C, the amount of B^{3+} adsorbed by IL-CNC@DP is not that significant amongst each other.

Therefore, this study indicates that the effect of the three temperatures was not a significant factor for the modified adsorbent. However, there is still a small variation in the adsorption capacity as the temperature increases. Applying statistical analysis the removal of B^{3+} onto IL-CNC@DP display a significant difference at a p-value of 1.8×10^{-13} , but experimentally the results are not significant. The results are consistent with the effect of temperature for Li^{1+} and Mo^{6+} adsorption onto IL-CNC@DP.

This further proves that the modified adsorbent is effective enough at low temperatures. The results demonstrate the adsorption capacity of B^{3+} at 5 mg/L onto IL-CNC@DP to be 4.50 mg/g (90.1%) at 25 °C then to increase slightly to 4.64 mg/g (92.9%) at 35 °C and then to decrease to 4.04 mg/g (80.9%) at 45 °C. Comparing these results to the adsorption capacity of B^{3+} at 100 mg/L, it was found to be 89.4 mg/g (97.60%) at 25 °C then to increase slightly to 98.2 mg/g (98.25%) at 35 °C and finally to 99 mg/g (99.00%) at 45 °C. Consequently, this shows the availability of active sites on the surface of the adsorbent at increasing initial concentrations. This can further prove that the removal of B^{3+} by the adsorption process using modified IL-CNC@DP adsorbent can be effective at low temperatures (25°C) since it shows high adsorption capacities at high initial concentrations. The other adsorbent, RDP, illustrated in Figure (B)

presents an increase of B^{3+} adsorption with increasing initial concentrations, but with more obvious variations under the three different temperatures. The removal of B^{3+} onto RDP illustrates a significant difference at a p-value of 1×10^{-7} . Additionally, the adsorption capacity of B^{3+} at 5 mg/L onto RDP is found to decrease from 0.44 mg/g (8.80%) at 25 °C to 0.32 mg/g (6.40%) at 35 °C and then increase to 0.40 mg/g (8.10%) at 45 °C. This trend of decreasing and then increasing with increasing temperatures is demonstrated up until initial concentrations of 30 mg/L and then the trend started to show other variations. At higher initial concentrations such as 70 mg/L and 100 mg/L, the optimum temperature was found to be 45 °C. Moreover, the trend of increasing and decreasing adsorption capacities under a variety of temperatures has been proven and it can be seen for Li^{1+} and Mo^{6+} adsorption onto RDP. Therefore, in this specific study, at 100 mg/L, the optimum temperature was found to be 45 °C, where the highest adsorption capacity occurs onto RDP.

Comparing all the effects of temperature results to each other, there are variations in the adsorption capacities for Li^{1+} , Mo^{6+} , & B^{3+} under 25 °C, 35 °C, & 45 °C. For example, the IL-CNC@DP adsorbent demonstrates fluctuations at 5 and 100 mg/L for all metals. Nonetheless, the highest adsorption capacity is obtained at 100 mg/L, regardless of the temperature value. As for RDP, at 5 mg/L, the trend is different, where for Li^{1+} & B^{3+} it decreases with increasing temperatures and for Mo^{6+} it is the opposite. On the other hand, at 100 mg/L for Li^{1+} , Mo^{6+} , & B^{3+} adsorption, it can be shown that as the temperature increases, the adsorption capacity increases. This can be justified by the different adsorption mechanisms each metal possesses towards the adsorbent and it is further explained in detail in 4.2.

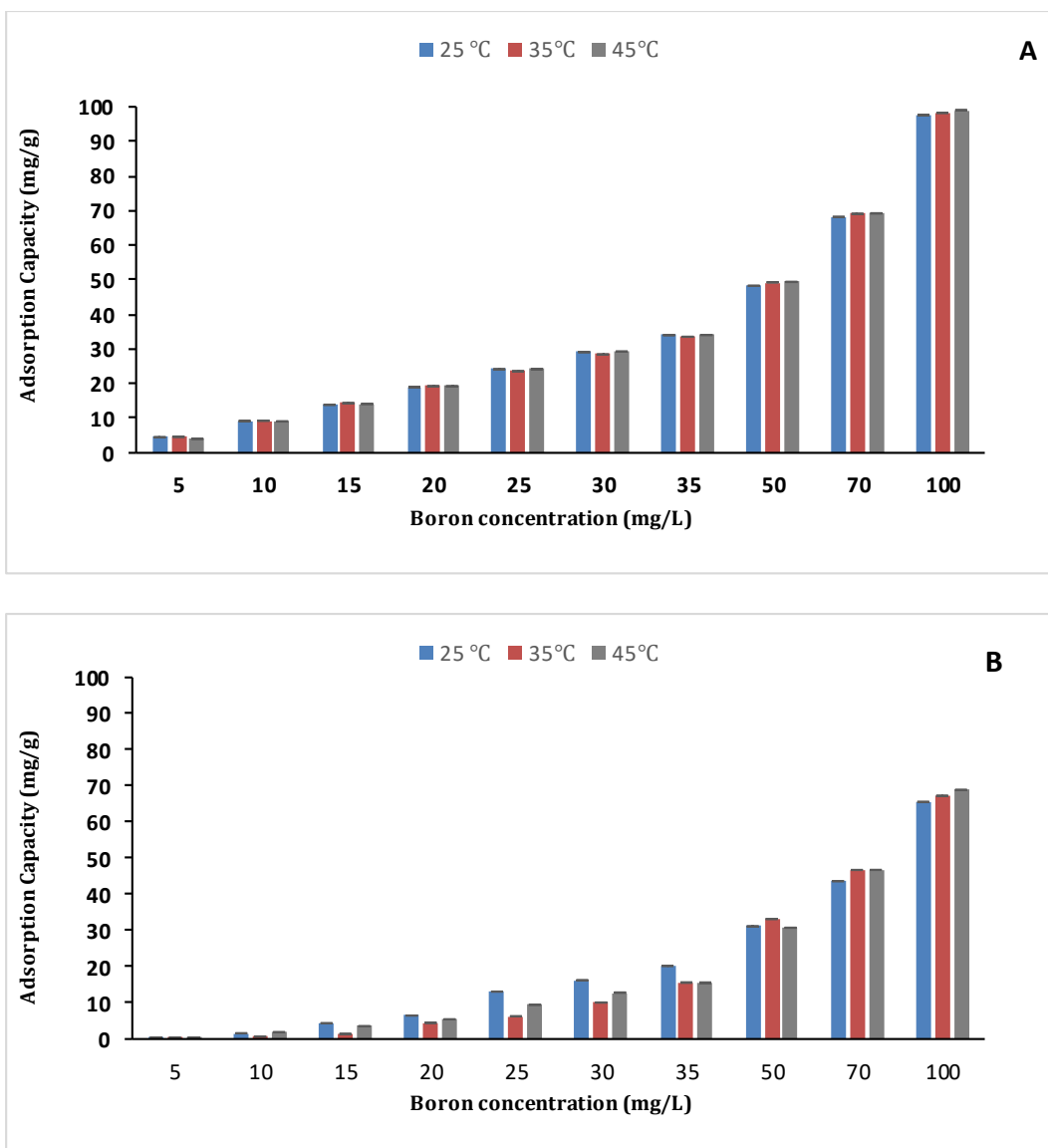


Figure 24. Effect of temperature on the IL-CNC@DP (A) & RDP (B) at different concentrations on B³⁺ adsorption.

Likewise, for this experiment, in Table 13, the values of ΔG° are negative for all the temperatures, indicating that the adsorption of B³⁺ onto IL-CNC@DP & RDP is feasible, spontaneous, and do not need an external driver for the reaction to take place. Similarly, the negative value of ΔH° for all the experiments indicates that the reactions were exothermic. Whereas the negative value of ΔS° confirmed that the adsorption of

B^{3+} on the surface of the IL-CNC@DP and RDP adsorbent is an associated mechanism. To be specific, the ΔG° values for the modified adsorbent IL-CNC@DP were -4037 kJ/mol, -3336 kJ/mol, and -2635 kJ/mol at 25 °C, 35 °C, and 45 °C, respectively. According to the results, it can be concluded that the adsorption of B^{3+} onto IL-CNC@DP was spontaneous at all the studied temperatures. The same results can be concluded for the adsorption of B^{3+} onto RDP for Gibbs free energy. While the values of ΔH° and ΔS° for IL-CNC@DP were -24942 kJ/mol and -70.11 kJ/mol, respectively, and for RDP the ΔH° and ΔS° values were -117.73 kJ/mol and -0.34 kJ/mol, respectively.

The ΔH° confirms that the effect of temperature on the adsorption of B^{3+} onto IL-CNC@DP and RDP did not have a noteworthy result on the adsorption process. While as for ΔS° results, it does not favor the high level of disorder in the adsorption process of B^{3+} onto IL-CNC@DP and RDP. These findings are similar to the Li^{1+} adsorption experiment onto IL-CNC@DP and RDP. The thermodynamics values are similar in their conclusions under the three studied temperatures. The calculation of the thermodynamics was based on the previously mentioned equations (6) and (7).

Table 13. Thermodynamic parameters for B^{3+} adsorption onto IL-CNC@DP & RDP.

Adsorbent	Temperature (°C)	$\ln(K_L)$	ΔG° (kJ/mol)	ΔH° (kJ/mol)	ΔS° (kJ/mol)
IL-CNC@DP	25	6.37	-4037	-24942	-70.11
	35	4.31	-3336		
	45	3.42	-2635		
RDP	25	1.55	-14.23	-117.73	-0.34
	35	1.84	-10.76		
	45	0.51	-7.29		

4.6 Adsorption isotherms of Li^{1+} , Mo^{6+} , B^{3+} removal onto IL-CNC@RDP and RDP

The linear adsorption isotherms for Li^{1+} adsorption onto IL-CNC@RDP and RDP at 25 °C, 35 °C, and 45 °C were investigated in order to define the relationship of the amount of metal adsorbed per gram of adsorbate at equilibrium (q_e) and equilibrium concentration of adsorbate (C_e) at constant temperature and pH. Therefore, four isotherm models were tested using Langmuir, Freundlich, Dubinin–Radushkevich, and Temkin models in Figures 25 and 27, and their parameters and constants are shown in Table 14 and their equations of line are shown in Figures 26 and 28 for both adsorbents. Based on general observation, the isotherm models for the two adsorbents show high values of R^2 . This means that the adsorption of Li^{1+} adsorption onto the modified and unmodified adsorbents could follow any of the mentioned models (Magdy et al., 2018). Both, the IL-CNC@DP & RDP adsorbent obtained the highest R^2 value with the Freundlich isotherm model.

It can be seen that the values of R^2 of the Langmuir model of the IL-CNC@DP and RDP follow the model's theory, although the R^2 value of the modified adsorbent is slightly better than the unmodified adsorbent. In general, this means that Li^{1+} molecules form a homogenous monolayer on the surface of both adsorbents along with different adsorption mechanisms with no interactions of molecules with adjacent sites (Uddin et al., 2017). The monolayer adsorption capacity (Q_0) of RDP is much higher than the modified adsorbent with values of 68 mg/g and 8.7 mg/g, respectively at 25 °C. Moreover, the b constant values indicate the adsorbent and adsorbate affinity offers the presence of strong binding of Li^{1+} onto both of the adsorbents (Al-Ghouti et al., 2019). Therefore, based on the Langmuir isotherm model the adsorption of Li^{1+} onto RDP is more favorable towards it than IL-CNC@DP in this case (Hilal et al., 2012). These

results mean that the RDP adsorbent best fits the Langmuir model theory. In addition, the R_L values of both adsorbents at all the studied temperatures were between value 0 and 1, therefore this indicates an energetically favorable adsorption process (Zango et al., 2020). The Freundlich isotherm model also shows that the adsorption process of both adsorbents as they follow this model to a great extent. The high R^2 values can conclude that the studied adsorbents are reversible and form non-uniform multilayers on the surface of the adsorbent (Vijayakumar et al., 2012). Moreover, the value of n of the modified and the unmodified adsorbent correspond to values that are less than 1. Therefore, both of the adsorption processes of Li^{1+} are considered unfavorable and chemical processes (Al-Ghouti & Al-Absi, 2020). Another important constant that is derived from this isotherm is $1/n$. According to the results, the value is greater than 1 for both adsorbents, therefore this indicates a cooperative adsorption process. Moreover, the adsorption capacity of Li^{1+} of the adsorbents is represented by the Freundlich constant (K_f) (Zango et al., 2020). According to the obtained results, it is evident that both IL-CNC@DP & RDP adsorbents have high adsorption capacities at 114.9 mg/g and 128.8 mg/g at 25 °C, respectively, for Li^{1+} when referring to the Freundlich isotherm model. It can be concluded that both adsorbents fit this model. Another isotherm model, Dubinin–Radushkevich, has B_D values obtained for both adsorbents as shown in Table 14. The results demonstrate that the adsorption process of Li^{1+} is an energy-free process. In addition, the adsorption capacity (q_s) values of the isotherm model show that the IL-CNC@DP adsorbent can attain higher adsorption of Li^{1+} than the RDP at 25 °C. Furthermore, the R^2 values of IL-CNC@DP are higher than RDP, which tends to provide a better description of the model than the RDP for the adsorption of Li^{1+} . Therefore, the Dubinin–Radushkevich isotherm model best fits the modified IL-CNC@DP adsorbent. The last isotherm model used in this study is the

Temkin adsorption isotherm model. It is evident that the R^2 values indicate that the model gives great fitting to both types of adsorbents although with better fitting for the RDP. As a result, the adsorption process of Li^{1+} depends on the heat of adsorption (Al-Ghouti & Al-Absi., 2020). The high values for the Temkin's heat of adsorption constant (B) will tend to offer a chemical exothermic adsorption process of Li^{1+} (de Farias Silva et al., 2020). It can be concluded that at 25 °C this model can fit both adsorbents.

The studies done at 35 & 45 °C for Langmuir, Freundlich, Dubinin–Radushkevich, and Temkin isotherm models are also demonstrated in Table 14. From Table 14, all the isotherm models for the two adsorbents show relatively high R^2 values at all temperatures, which means that the adsorption of Li^{1+} could follow all models. Yet, the IL-CNC@DP displayed the highest R^2 value with the Langmuir isotherm model at 45 °C, while with the Freundlich isotherm model, the highest R^2 is for IL-CNC@DP is at 35 °C. The Dubinin–Radushkevich isotherm model for IL-CNC@DP demonstrates the highest R^2 at 35 °C, whereas the Temkin isotherm model at 45 °C. The RDP displayed the highest R^2 value with the Langmuir isotherm model at 35 °C, while with the Freundlich isotherm model; the highest R^2 for RDP is at 45 °C. The highest R^2 for the RDP adsorbent with Dubinin–Radushkevich and Temkin isotherm model were observed at 35 °C. This signifies how the changes in temperature values impact the mechanism of adsorption onto the modified and unmodified adsorbent (Magdy et al., 2018). It is worth mentioning that the R^2 value reached 0.96 when the temperature increased to 45 °C for the IL-CNC@DP. This can indicate that that the adsorption of Li^{1+} onto IL-CNC@DP follows the Langmuir isotherm model better at higher temperatures, while the adsorption onto RDP best fits the model at lower temperatures (35°C). Although the monolayer adsorption capacity (Q_0) of both adsorbents at 35 and 45 °C did not drastically change as the temperature increased, however, the RDP is

much higher than the modified adsorbent regarding the adsorption capacity values. Moreover, the b constant values are more favorable towards RDP based on the Langmuir isotherm model. As for the Freundlich isotherm model, as previously mentioned, the high R^2 values for the IL-CNC@DP & RDP at both temperatures (35 & 45 °C) show the fitting of the adsorption mechanism of Li^{1+} . This means that Li^{1+} forms reversible and non-uniform multilayers on the surface of the adsorbent. Additionally, the value of n of the modified adsorbent and the unmodified adsorbent corresponds to values that are less than 1. Therefore, both of the adsorption processes of Li^{1+} is considered a considered unfavorable and chemical processes at 35 and 45 °C. Regarding the modified adsorbent, the value of n at 45 °C is 0.20 and at 35 °C is 0.18; this indicates that the increased favorability of the adsorption occurs as the temperature increases to 45 °C. In addition, the constant $1/n$ for IL-CNC@DP is greater than 1, but it decreases as the temperature increases, which indicates a cooperative adsorption process as it becomes more heterogeneous. The Freundlich constant (K_f) for IL-CNC@DP adsorbent did not significantly change when the temperature increased from 35 to 45 °C, meaning that they share comparable adsorption capacity towards Li^{1+} . However, the K_f value of the RDP decreased from 529.8 mg/g to 336.2 mg/g when the temperature increased from 35 to 45 °C, indicating the significant impact the temperature has on the adsorption capacity of RDP. As for the Dubinin–Radushkevich isotherm model, the B_D results demonstrate that the adsorption process of Li^{1+} is an energy-free process and the adsorption capacity (q_s) values of the isotherm model show that the IL-CNC@DP adsorbent at 35 °C displayed a higher adsorption capacity at 1098 mg/g than the RDP at 529.8 mg/g for the removal of Li^{1+} . Similar results demonstrate that at 45 °C, the IL-CNC@DP adsorbent displayed a higher adsorption capacity at 808 mg/g than the RDP at 336.2 mg/g. Lastly, the Temkin adsorption

isotherm model R^2 values indicate that the model gives great fitting to both types of adsorbents although with better fitting for the RDP at 35 & 45 °C. Moreover, positive values of Temkin's heat of sorption constant (B) offer a chemical exothermic adsorption process of Li^{1+} at both temperatures.

Table 14. The parameters of the two isotherms models for lithium adsorption onto IL-CNC@RDP and RDP at 25 °C, 35 °C, and 45 °C.

Adsorbent	T (°C)	Langmuir Q_0 (mg/g)	b (L/mg)	R^2	Freundlich K_f (mg/g) (L/g) ⁿ	n	1/n	R^2	
IL-CNC@DP	25	8.7	86.7	0.94	114.9	0.19	5.0	0.97	
	35	5.6	39.1	0.94	221.6	0.18	5.4	0.97	
	45	3.09	13.0	0.96	203.0	0.20	4.8	0.96	
	T (°C)	Temkin A_T (L/mg)	B (J/mol)	R^2	Dubinin-Radushkevich q_s (mg/g)	B_D	R^2		
	25	0.63	28.9	0.80	674.5	-9x10 ⁻⁷	0.97		
	35	0.69	26.6	0.86	1098	-7x10 ⁻⁷	0.98		
	45	0.46	4.5	0.96	808	-6x10 ⁻⁷	0.92		
	RDP	T (°C)	Langmuir Q_0 (mg/g)	b (L/mg)	R^2	Freundlich K_f (mg/g) (L/g) ⁿ	n	1/n	R^2
		25	68.0	170.4	0.83	128.8	0.14	6.8	0.94
35		32.7	50.6	0.93	529.8	0.102	9.7	0.90	
45		34.7	53.7	0.92	336.2	0.106	9.3	0.95	
T (°C)		Temkin A_T (L/mg)	B (J/mol)	R^2	Dubinin-Radushkevich q_s (mg/g)	B_D	R^2		
25		0.54	25.0	0.90	41.1	-0.0001	0.90		
35		0.52	16.9	0.95	48.9	-8x10 ⁻⁵	0.91		
45		0.54	33.3	0.91	44.0	-8x10 ⁻⁵	0.89		

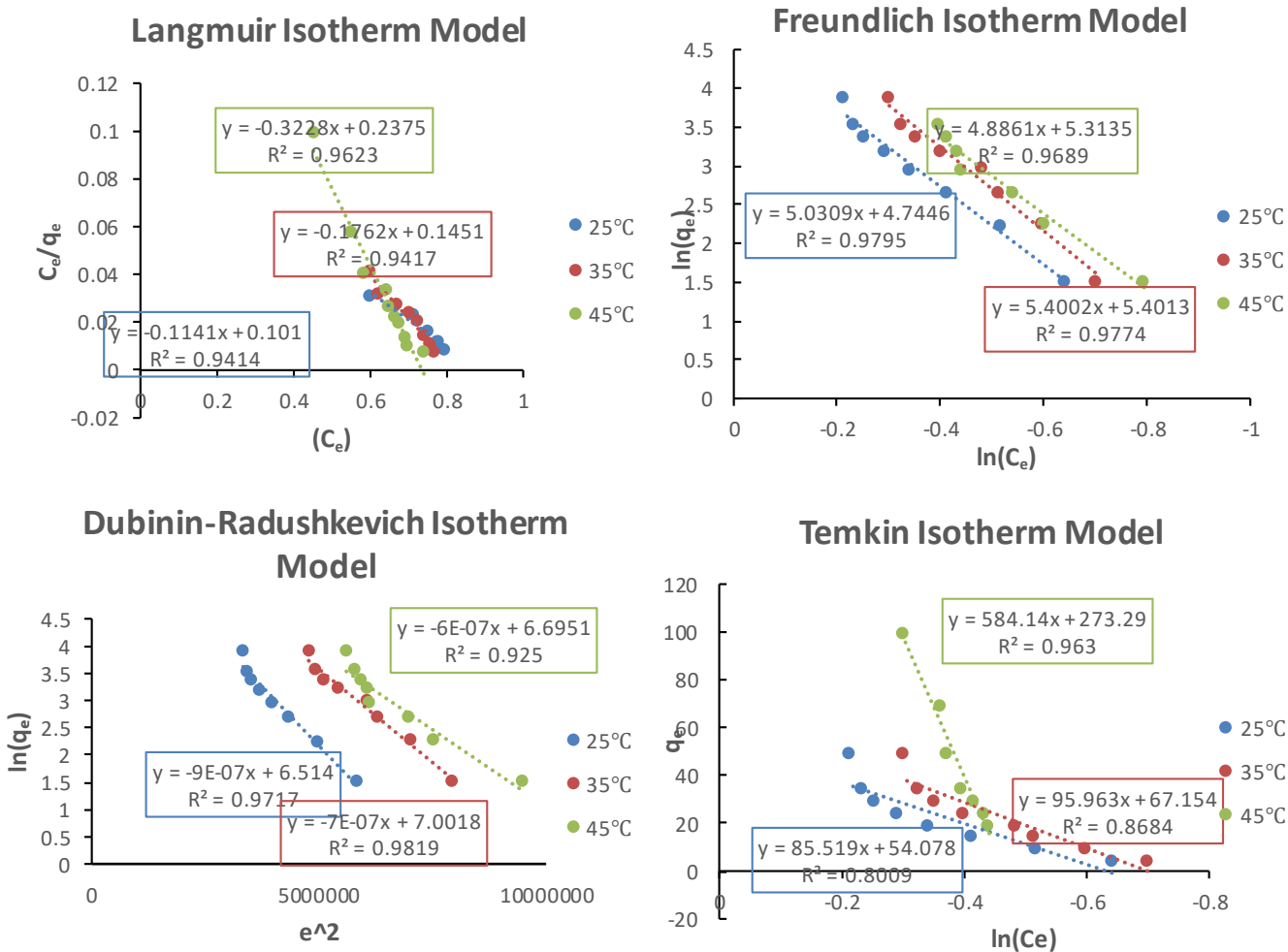


Figure 25. Adsorption isotherm models used in the current study of the adsorption of Li^{1+} metal ions onto IL-CNC@DP.

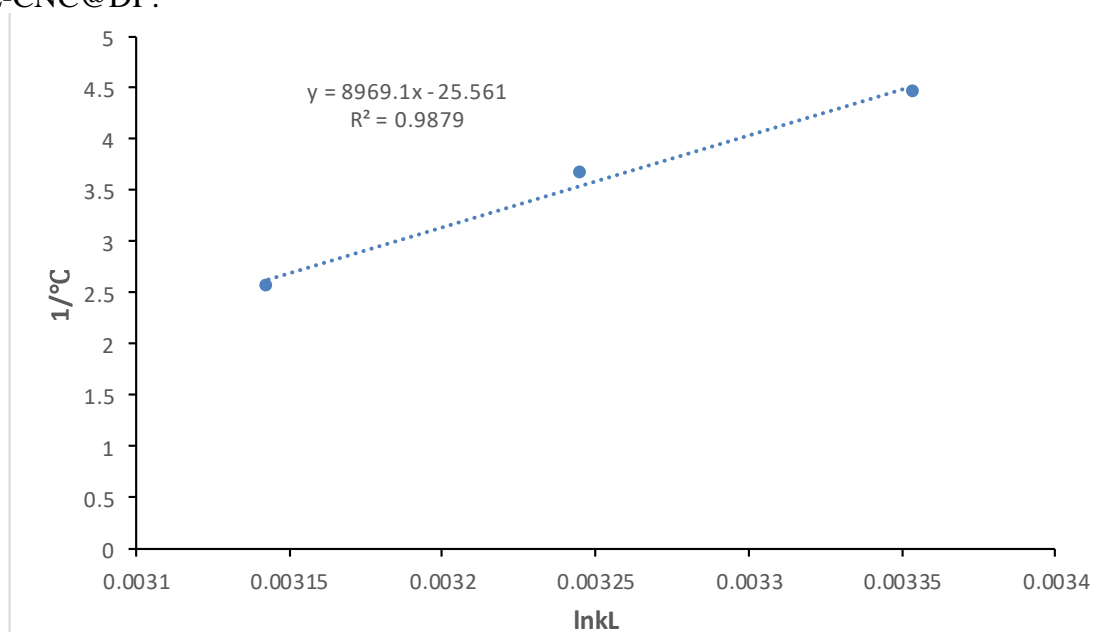


Figure 26. Plot for the calculation of the thermodynamic parameters ΔS° and ΔH° of Lithium adsorption onto IL-CNC@RDP.

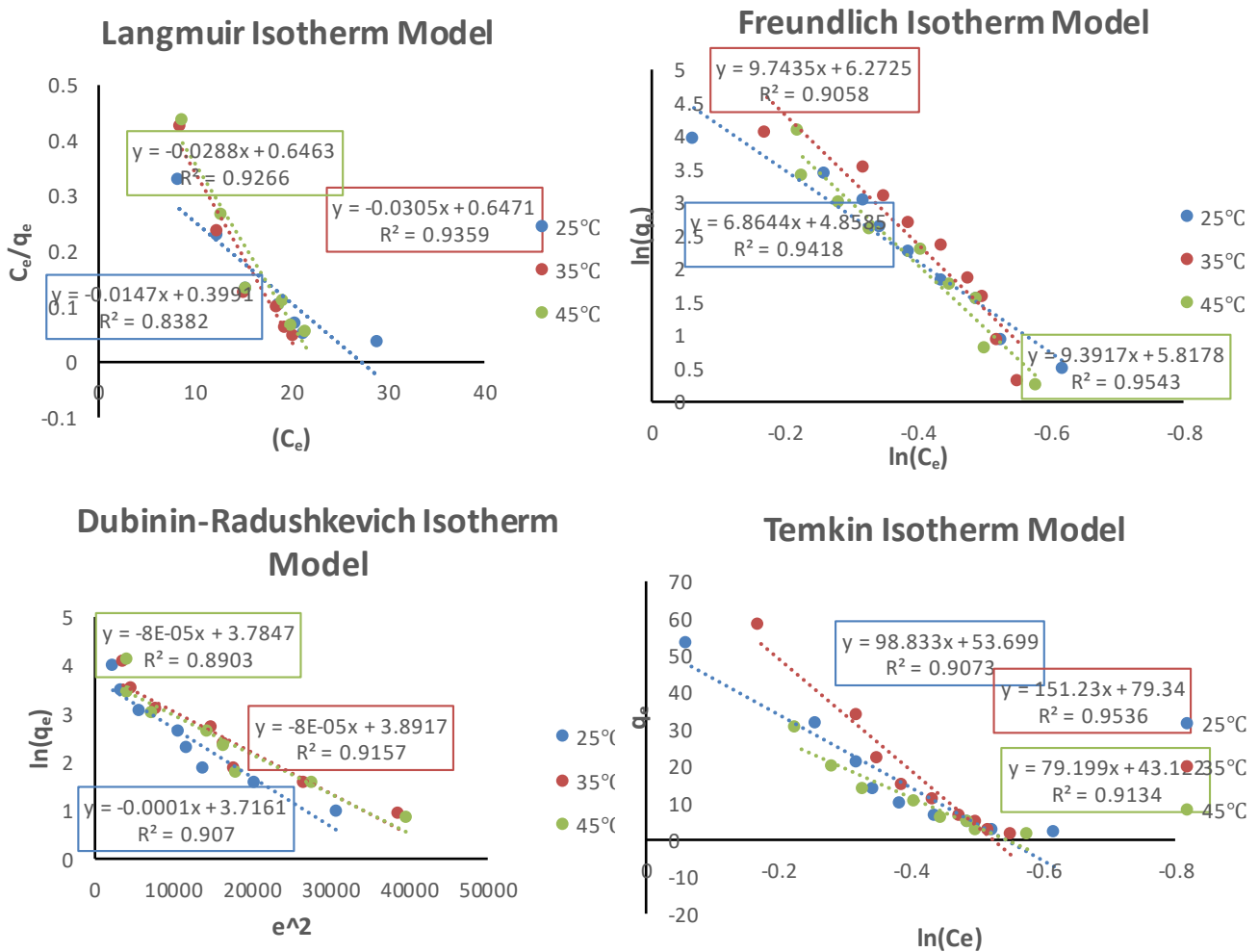


Figure 27. Adsorption isotherm models used in the current study of the adsorption of Li^{1+} metal ions onto RDP.

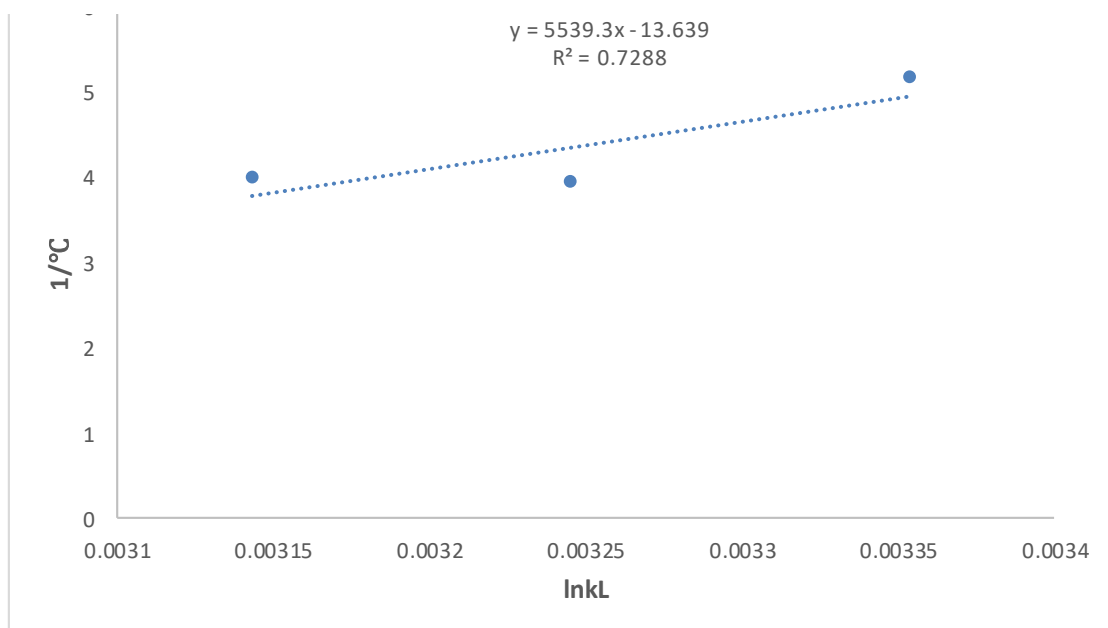


Figure 28. Plot for the calculation of the thermodynamic parameters ΔS° and ΔH° of Lithium adsorption onto RDP.

Regarding Mo^{6+} adsorption onto IL-CNC@RDP and RDP at 25 °C, 35 °C, and 45 °C, linear adsorption isotherms were investigated by studying the four isotherm models, shown in Figures 29 and 31. Their parameters and constants are shown in Table 15 and their equations of the line are shown in Figures 30 and 32 for both adsorbents. By generally looking at the table, the two adsorbents display high values of R^2 , meaning that the adsorption of Mo^{6+} onto the modified and unmodified adsorbents could follow any of the mentioned models. The IL-CNC@DP has the highest R^2 value with the Langmuir isotherm model, whereas the Temkin isotherm model with the highest R^2 value for the RDP.

To be specific, the values of R^2 of the Langmuir model of the IL-CNC@DP and RDP follow the model's theory, even though the R^2 value of the modified adsorbent is somewhat better than the unmodified adsorbent. This proves that the Mo^{6+} molecules form a homogenous monolayer on the surface of both adsorbents. Regardless of the R^2 value, the monolayer adsorption capacity (Q_0) of IL-CNC@DP is much higher than the RDP adsorbent with values of 7.4 mg/g and 1.4 mg/g, respectively at 25 °C. Additionally, the b constant values indicate the adsorbent and adsorbate affinity offers the presence of strong binding of Mo^{6+} onto both of the adsorbents. Therefore, based on the Langmuir isotherm model the adsorption of Mo^{6+} onto IL-CNC@DP is more favorable towards it than RDP. These results mean that the IL-CNC@DP adsorbent best fits the Langmuir model theory. The R_L values of both adsorbents at all the studied temperatures were between values 0 and 1, therefore this indicates an energetically favorable adsorption process. The second model is the Freundlich isotherm and it presents high R^2 values that could mean that the studied adsorbents are reversible and form non-uniform multilayers on the surface of the adsorbent. Additionally, the value of n of the modified and the unmodified adsorbent correspond to values that are less

than 1. Therefore, both of the adsorption processes of Mo^{6+} are considered unfavorable and chemical processes. Another constant, which is $1/n$, is found to be greater than 1 for both adsorbents, therefore this specifies a cooperative adsorption process. The Freundlich constant (K_f) has high adsorption capacities at 650.7 mg/g and 1553.5 mg/g at 25 °C for Mo^{6+} onto IL-CNC@DP and RDP, respectively. It can be concluded that both adsorbents fit this model. For the Dubinin–Radushkevich isotherm model, the B_D values obtained for both adsorbents demonstrate that the adsorption process of Mo^{6+} is an energy-free process, as shown in Table 15. Moreover, the adsorption capacity (q_s) values display that the IL-CNC@DP adsorbent can achieve higher adsorption of Mo^{6+} than the RDP at 25 °C along with higher R^2 values. Therefore, the Dubinin–Radushkevich isotherm model best fits the modified IL-CNC@DP adsorbent. The last isotherm model is the Temkin adsorption isotherm model. It is evident that the R^2 values indicate that the model gives great fitting to both types and the high values for the Temkin’s heat of sorption constant (B) will tend to offer a chemical exothermic adsorption process of Mo^{6+} . It can be concluded that at 25 °C this model can fit both adsorbents.

Regarding the other two temperatures, 35 °C & 45 °C, demonstrated in Table 15. From Table 15, all models for the two adsorbents show somewhat high R^2 values, which means that the adsorption of Mo^{6+} could follow any models. Yet, the IL-CNC@DP displayed similar high R^2 values for the Langmuir and Freundlich isotherm model at 35 °C & 45 °C. The Dubinin–Radushkevich and Temkin isotherm model for IL-CNC@DP demonstrated the highest R^2 at 45 °C & 35 °C, respectively. The RDP displayed the highest R^2 value with the Langmuir, Temkin, and Freundlich isotherm model at 35 °C, whereas the highest R^2 is with Dubinin–Radushkevich at 45 °C. By looking at the trend regarding the R^2 values, generally as the temperature increases, the values tend to

decrease for both adsorbents. As for the monolayer adsorption capacity (Q_0) of both adsorbents at 35 °C and 45 °C for the Langmuir isotherm model, it did not drastically change as the temperature increased. The b constant values are more favorable towards RDP based on the Langmuir isotherm model. As for the Freundlich isotherm model, as previously stated, the high R^2 values for the IL-CNC@DP & RDP at 35 °C and 45 °C show the fitting of the adsorption mechanism of Mo^{6+} . This means that Mo^{6+} forms reversible and non-uniform multilayers on the surface of the adsorbents. Additionally, the value of n of the modified adsorbent and the unmodified adsorbent corresponds to values that are less than 1. Therefore, both of the adsorption processes of Mo^{6+} is considered an unfavorable and chemical process at 35 °C and 45 °C. The constant $1/n$ is greater than 1, which indicates a cooperative adsorption process. The Freundlich constant (K_f) for IL-CNC@DP adsorbent did significantly change when the temperature increased from 35 °C to 45 °C, meaning that they have dissimilar adsorption capacity towards Mo^{6+} . The K_f value of the RDP decreased from 297152 mg/g to 162267 mg/g when the temperature increased from 35 to 45 °C, indicating the significant impact the temperature has on the adsorption capacity of RDP. As for the Dubinin–Radushkevich isotherm model, the B_D results demonstrate that the adsorption process of Mo^{6+} is an energy-free process and the adsorption capacity (q_s) values of the isotherm model show that the IL-CNC@DP adsorbent at 35 °C displayed a lower adsorption capacity at 6.47 mg/g than the RDP at 56.0 mg/g for the removal of Mo^{6+} . Similar results demonstrate that at 45 °C, the IL-CNC@DP adsorbent displayed a lower adsorption capacity at 64.07 mg/g than the RDP at 88.2 mg/g. Lastly, the Temkin adsorption isotherm model R^2 values prove that the model gives great fitting to both types of adsorbents although with better fitting for the RDP. Moreover, positive values of Temkin's heat of sorption constant (B) offer a chemical exothermic adsorption

process of Mo^{6+} at both temperatures.

Differences at 25 °C are most likely to be found between Mo^{6+} & Li^{1+} adsorption in terms of isotherm models. For example, the R^2 value for Mo^{6+} adsorption was less when comparing it to the Li^{1+} adsorption models at 25 °C for both adsorbents. Moreover, in general, the modified adsorbent (IL-CNC@DP), follows the Langmuir isotherm model better than unmodified (RDP) Mo^{6+} adsorption, whereas it's the opposite for Li^{1+} adsorption onto all temperatures. On the contrary, both adsorption processes for Mo^{6+} and Li^{1+} are considered unfavorable, chemical, and cooperative adsorption processes based on their constants for the Freundlich model. Therefore, both metals fit this model. Moreover, the Dubinin–Radushkevich isotherm model best fits the modified adsorbent (IL-CNC@DP) adsorbent better for Mo^{6+} & Li^{1+} , whereas the Temkin isotherm model gives great fitting to both types of adsorbents although with better fitting for the RDP for Li^{1+} adsorption. The other two temperatures (35°C and 45°C) also show variations in their isotherm models. For example, RDP adsorbent is much higher than IL-CNC@DP adsorbent regarding their adsorption capacity values for Li^{1+} in Langmuir isotherm model but Mo^{6+} ; no substantial differences are enough to form such a conclusion. Regarding the Dubinin–Radushkevich isotherm model, the B_D results demonstrate that the adsorption process of Mo^{6+} & Li^{1+} is an energy-free process and the adsorption capacities (q_s) between the metals differ according to their results depending upon the temperatures used.

Table 15. The parameters of the two isotherms models for molybdenum adsorption onto IL-CNC@RDP and RDP at 25 °C, 35 °C, and 45 °C.

Adsorbent	T (°C)	Langmuir Q ₀ (mg/g)	b (L/mg)	R ²	Freundlich K _f (mg/g) (L/g) ⁿ	n	1/n	R ²
IL-CNC@DP	25	7.4	32.1	0.94	650.7	0.24	4.0	0.91
	35	3.3	4.2	0.93	215.6	0.15	6.4	0.893
	45	2.00	1.7	0.93	53.5	0.11	9.04	0.894
	T (°C)	Temkin A _T (L/mg)	B (J/mol)	R ²	Dubinin-Radushkevich q _s (mg/g)	B _D	R ²	
	25	1.29	45.4	0.90	421.0	-4x10 ⁻⁷	0.84	
	35	0.57	72.7	0.806	6.47	5x10 ⁻⁷	0.76	
	45	0.57	103.6	0.803	64.07	8x10 ⁻⁷	0.85	
	T (°C)	Langmuir Q ₀ (mg/g)	b (L/mg)	R ²	Freundlich K _f (mg/g) (L/g) ⁿ	n	1/n	R ²
	25	1.4	42.0	0.95	1553.5	0.16	5.8	0.93
RDP	35	6.9	1127.9	0.86	297152	0.10	9.8	0.92
	45	4.7	509.0	0.85	162267	0.09	10.01	0.89
	T (°C)	Temkin A _T (L/mg)	B (J/mol)	R ²	Dubinin-Radushkevich q _s (mg/g)	B _D	R ²	
	25	1.08	84.2	0.90	38.3	-8x10 ⁻⁵	0.81	
	35	1.20	81.29	0.94	56.0	-6x10 ⁻⁵	0.87	
	45	1.12	118.34	0.93	88.2	-8x10 ⁻⁵	0.89	

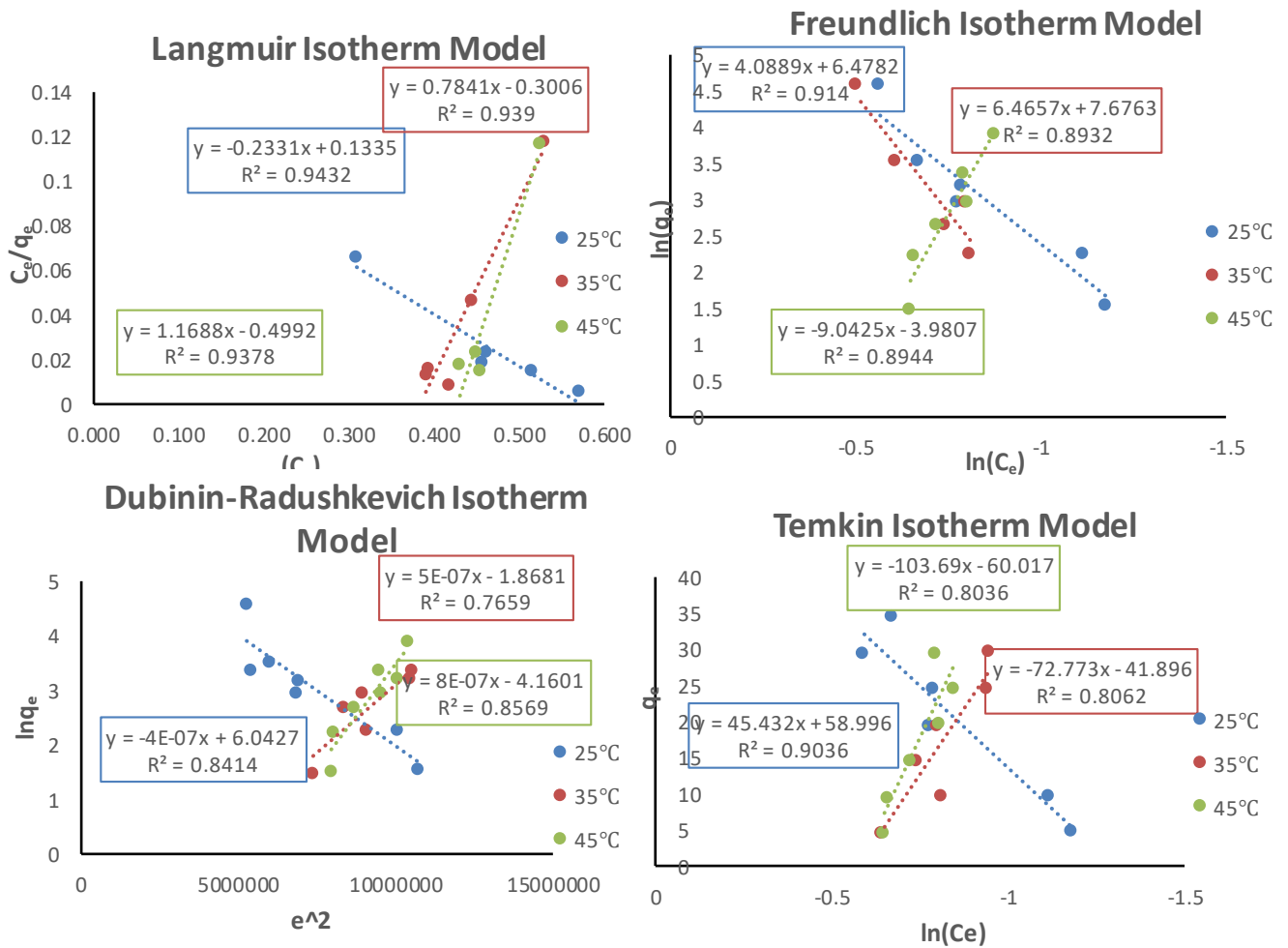


Figure 29. Adsorption isotherm models used in the current study of the adsorption of Mo^{6+} metal ions onto IL-CNC@DP.

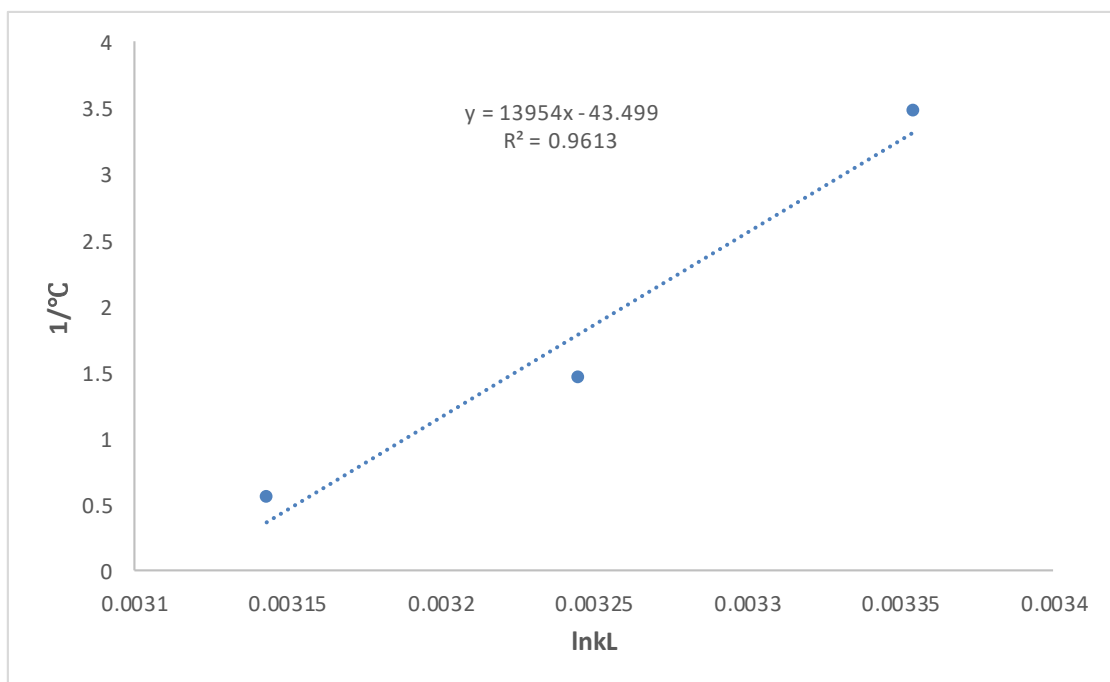


Figure 30. Plot for the calculation of the thermodynamic parameters ΔS° and ΔH° of Molybdenum adsorption onto IL-CNC@DP.

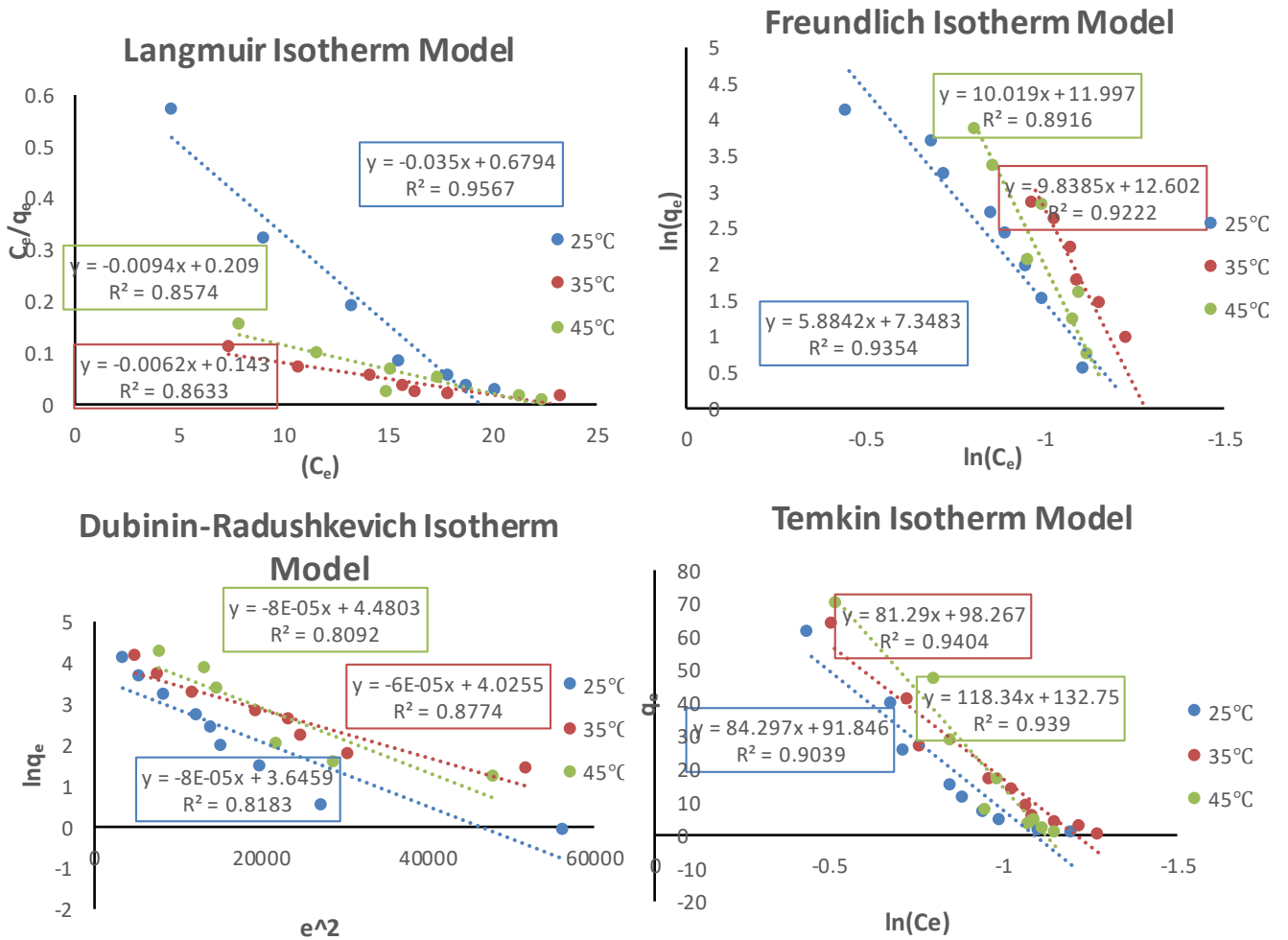


Figure 31. Adsorption isotherm models used in the current study of the adsorption of Mo^{6+} metal ions onto RDP.

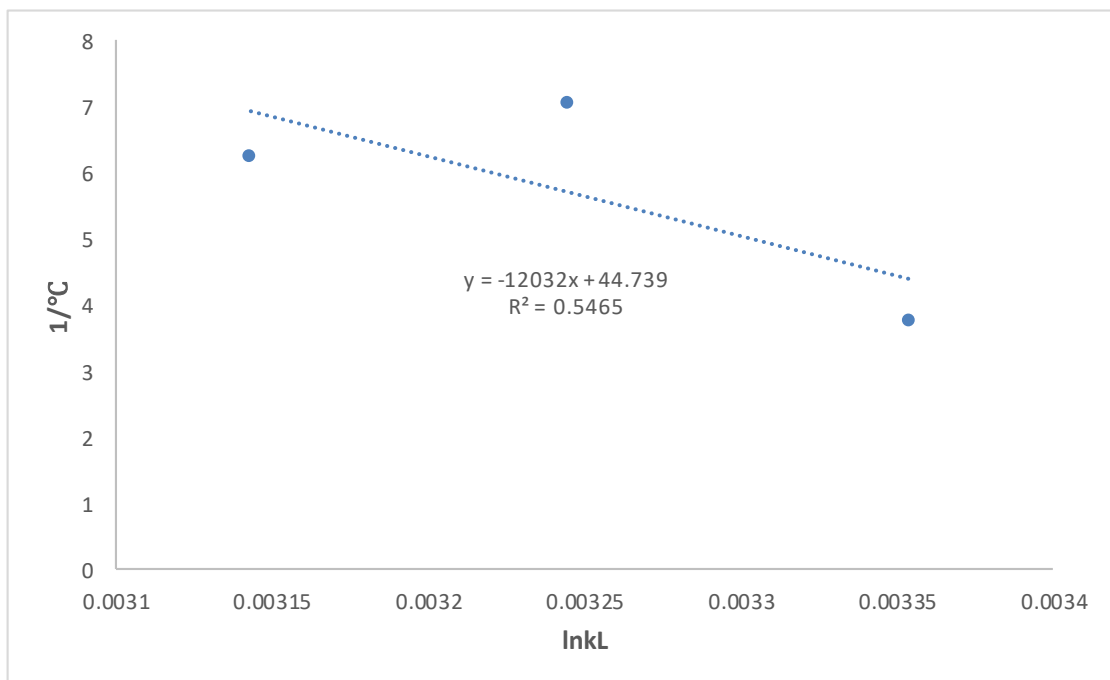


Figure 32. Plot for the calculation of the thermodynamic parameters ΔS° and ΔH° of Molybdenum adsorption onto RDP.

As for B^{3+} adsorption onto IL-CNC@RDP and RDP, they are demonstrated in Figures 33 and 35. Their parameters and constants are shown in Table 16 and their equations of the line are shown in Figures 34 and 36 for both adsorbents. By generally looking at the table, the models for the two adsorbents display a variety of R^2 values, where some are not as high as they are expected to be. This means that the adsorption of B^{3+} onto the modified and unmodified adsorbents might not follow all of the mentioned models. The IL-CNC@DP and RDP adsorbents have the highest R^2 values for the Dubinin–Radushkevich model at 25 °C.

On the other hand, the value of R^2 of the Langmuir model of the IL-CNC@DP is low (0.75), therefore we can conclude that they do not follow the model's theory. On the other hand, the R^2 value for RDP follows the model theory better. This proves that the B^{3+} molecules form a homogenous monolayer on the surface of RDP adsorbent better than IL-CNC@DP. Regardless of the R^2 value, the monolayer adsorption capacity (Q_0) of IL-CNC@DP is much higher than the RDP adsorbent with values of 588.2 mg/g and 4.72 mg/g, respectively at 25 °C. Furthermore, the b constant values indicate the adsorbent and adsorbate affinity offers the presence of strong binding of B^{3+} onto both of the adsorbents. Therefore, based on the Langmuir isotherm model the adsorption of B^{3+} onto IL-CNC@DP is followed to a certain degree but it is more favorable towards RDP according to the R^2 value. These results mean that the RDP adsorbent best fits the Langmuir model theory. The R_L values of both adsorbents at all the studied temperatures were between values 0 and 1, therefore this indicates an energetically favorable adsorption process. The second model is the Freundlich isotherm model and it presents high R^2 values for the RDP adsorbent, which could mean that the studied adsorbent forms non-uniform multilayers on its surface. As for the IL-CNC@DP adsorbent, the adsorption of B^{3+} is followed to a certain degree regarding its R^2 values.

As well, the value of n of the modified and the unmodified adsorbent corresponds to values that are less than 1. Therefore, both of the adsorption processes of B^{3+} are considered unfavorable and chemical processes. Another constant, which is $1/n$, is found to be greater than 1 for both adsorbents, therefore this specifies a cooperative adsorption process. Lastly, the Freundlich constant (K_f) at 25 °C has high adsorption capacity at 122 mg/g onto IL-CNC@DP and extremely high adsorption capacity at 102.4×10^5 mg/g onto RDP for B^{3+} . It can be concluded that both adsorbents fit this model. The third model is the Dubinin–Radushkevich isotherm. The B_D values obtained for both adsorbents demonstrate that the adsorption process of B^{3+} is an energy-free process, as shown in Table 16. Moreover, the adsorption capacity (q_s) values demonstrate that the IL-CNC@DP adsorbent can achieve higher adsorption of B^{3+} at 105.44 mg/g more than the RDP at 68.46 mg/g along with high R^2 values for both at 25 °C. Therefore, the Dubinin–Radushkevich isotherm model best fits the modified IL-CNC@DP adsorbent. However, it still can be considered a good fit for the unmodified RDP adsorbent. The last model, which is the Temkin adsorption isotherm model, shows high R^2 values for RDP more than IL-CNC@DP. Moreover, Temkin’s heat of sorption constant (B) offers a chemical exothermic adsorption process of B^{3+} with higher values for RDP adsorbent. Hence, it can be concluded that at 25 °C this model is a better fit for RDP in contrast to IL-CNC@DP.

As for 35 °C & 45 °C, Langmuir, Freundlich, Dubinin–Radushkevich, and Temkin isotherm models are also demonstrated in Table 16. The R^2 values show variations, which means that the adsorption of B^{3+} could follow any models. For example, IL-CNC@DP displayed low R^2 values for the Langmuir isotherm model at 35 °C & 45 °C, whereas high R^2 values for the Freundlich, Dubinin–Radushkevich, and Temkin isotherm model at 35 °C & 45 °C. On the other hand, the RDP adsorbent displayed the

highest R^2 value with the Langmuir, Temkin, and Freundlich isotherm model at 35 °C, whereas the highest R^2 is with Dubinin–Radushkevich at 45 °C. By looking at the trend regarding the R^2 values, generally as the temperature increases, the values tend to decrease for both adsorbents. As for the monolayer adsorption capacity (Q_0) of both adsorbents at 35 °C and 45 °C for the Langmuir isotherm model as the temperature increases, the adsorption capacity decreases. It can be concluded that the Langmuir isotherm is more favorable towards RDP at 35 °C. As for the Freundlich isotherm model, the high R^2 values at 35 °C and 45 °C for IL-CNC@DP and high R^2 values at 35 °C for RDP show the best fitting of the adsorption mechanism of B^{3+} . This means that B^{3+} forms reversible and non-uniform multilayers on the surface of the adsorbents at the mentioned temperatures. Additionally, the value of n of the modified adsorbent and the unmodified adsorbent corresponds to values that are greater than 1. Therefore, both of the adsorption processes of B^{3+} is considered an unfavorable and chemical process at 35 °C and 45 °C. Furthermore, the constant $1/n$ is greater than 1, which indicates a cooperative adsorption process. The Freundlich constant (K_f) for IL-CNC@DP and RDP adsorbent did significantly change when the temperature increased from 35 °C to 45 °C, meaning that they have dissimilar adsorption capacity towards B^{3+} . As for the Dubinin–Radushkevich isotherm model, the B_D results demonstrate that the adsorption process of B^{3+} is an energy-free process for both adsorbents at 35 °C and 45 °C. The adsorption capacity (q_s) values of the isotherm model show that the IL-CNC@DP adsorbent at 35 °C displayed a lower adsorption capacity at 37.50 mg/g than the RDP at 53.91 mg/g for the removal of B^{3+} . Similar results demonstrate that at 45 °C, the IL-CNC@DP adsorbent displayed a much lower adsorption capacity at 1.47 mg/g than the RDP at 87.29 mg/g. Lastly, the Temkin adsorption isotherm model R^2 values prove that the model gives great fitting to both types of adsorbents although with better

fitting for the IL-CNC@DP. Additionally, positive values of Temkin's heat of sorption constant (B) offer a chemical exothermic adsorption process of B^{3+} at both temperatures.

Comparing B^{3+} adsorption to Mo^{6+} & Li^{1+} adsorption in terms of isotherm models, the R^2 values are much less significant at 25 °C for both adsorbents. The unmodified (RDP) follows the Langmuir isotherm model better than the modified adsorbent (IL-CNC@DP) onto all temperatures for Li^{1+} and B^{3+} adsorption only. Moreover, the same conclusions offered towards Mo^{6+} and Li^{1+} for the Freundlich model can be seen towards B^{3+} , where based on their constants they are unfavorable, chemical, and cooperative adsorption processes. Moreover, the Dubinin–Radushkevich isotherm model best fits both adsorbents for B^{3+} , the same can be seen for Mo^{6+} & Li^{1+} . On the other hand, the Temkin isotherm model gives great fitting to Li^{1+} and B^{3+} adsorption for RDP.

Table 16. The parameters of the two isotherms models for boron adsorption onto IL-CNC@RDP and RDP at 25 °C, 35 °C, and 45 °C.

Adsorbent	T (°C)	Langmuir Q ₀ (mg/g)	b (L/mg)	R ²	Freundlich K _f (mg/g) (L/g) ⁿ	n	1/n	R ²	
IL-CNC@DP	25	588.2	980392	0.75	122	0.42	2.3	0.81	
	35	74.62	8200.75	0.57	160	0.37	2.6	0.90	
	45	30.58	364.06	0.34	8.03	0.26	3.7	0.89	
	T (°C)	Temkin A _T (L/mg)	B (J/mol)	R ²	Dubinin-Radushkevich q _s (mg/g)	B _D	R ²		
	25	2.10	56.77	0.80	105.44	-5x10 ⁻⁷	0.93		
	35	1.54	40.28	0.87	37.50	-2x10 ⁻⁷	0.89		
	45	1.39	27.76	0.97	1.47	-7x10 ⁻⁷	0.78		
	RDP	T (°C)	Langmuir Q ₀ (mg/g)	b (L/mg)	R ²	Freundlich K _f (mg/g) (L/g) ⁿ	n	1/n	R ²
		25	4.72	297.36	0.82	102.4x10 ⁵	0.16	6.1	0.90
35		6.30	759.18	0.90	8.1x10 ⁴	0.24	4.1	0.91	
45		1.67	57.73	0.79	2.067	0.10	9.7	0.49	
T (°C)		Temkin A _T (L/mg)	B (J/mol)	R ²	Dubinin-Radushkevich q _s (mg/g)	B _D	R ²		
25		2.51	120.93	0.91	68.46	-6x10 ⁻⁵	0.92		
35		2.63	165.78	0.80	53.91	-7x10 ⁻⁵	0.75		
45		0.09	45.14	0.70	87.29	-7x10 ⁻⁵	0.87		

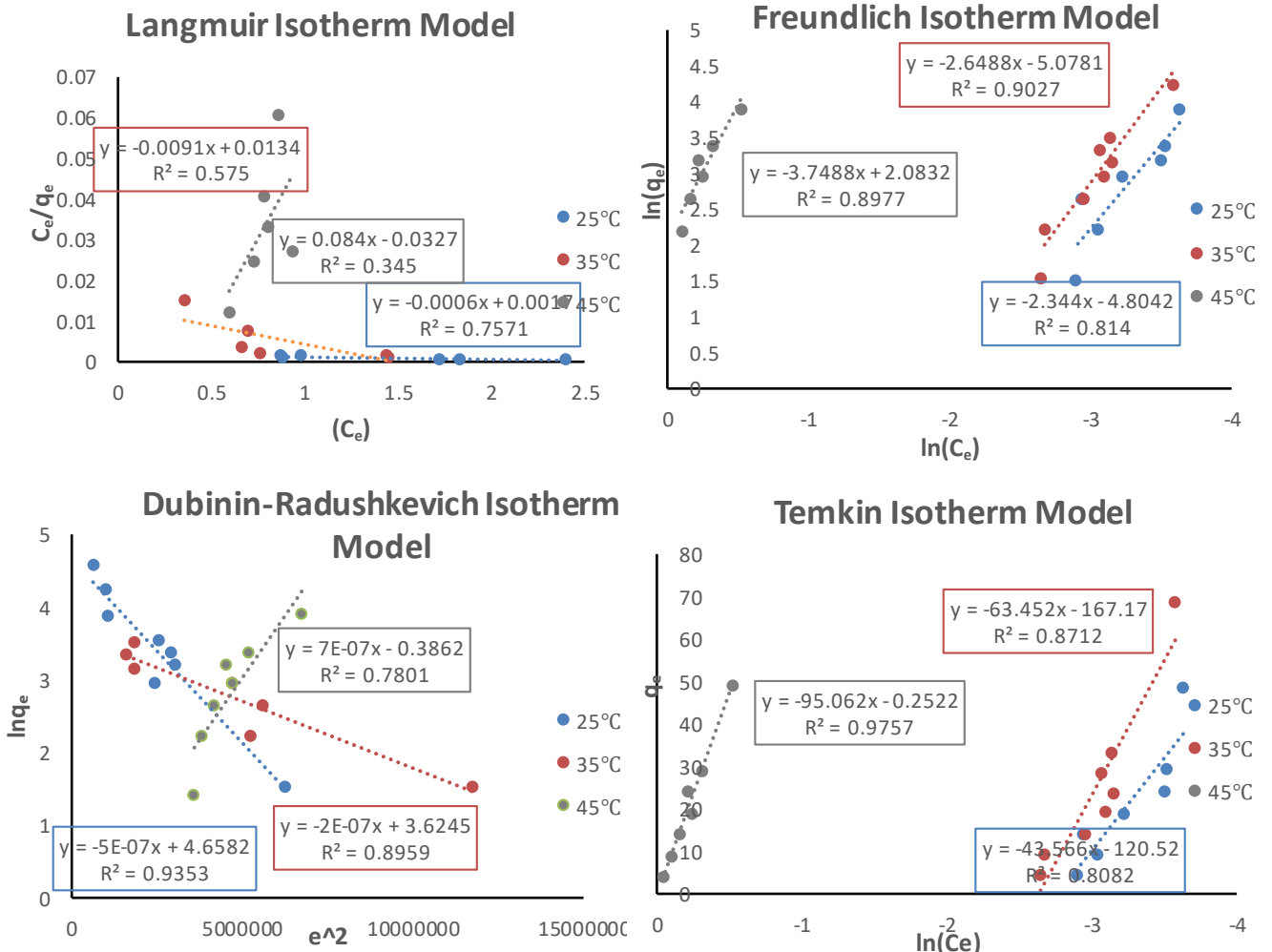


Figure 33. Adsorption isotherm models used in the current study of the adsorption of B^{3+} metal ions onto IL-CNC@DP.

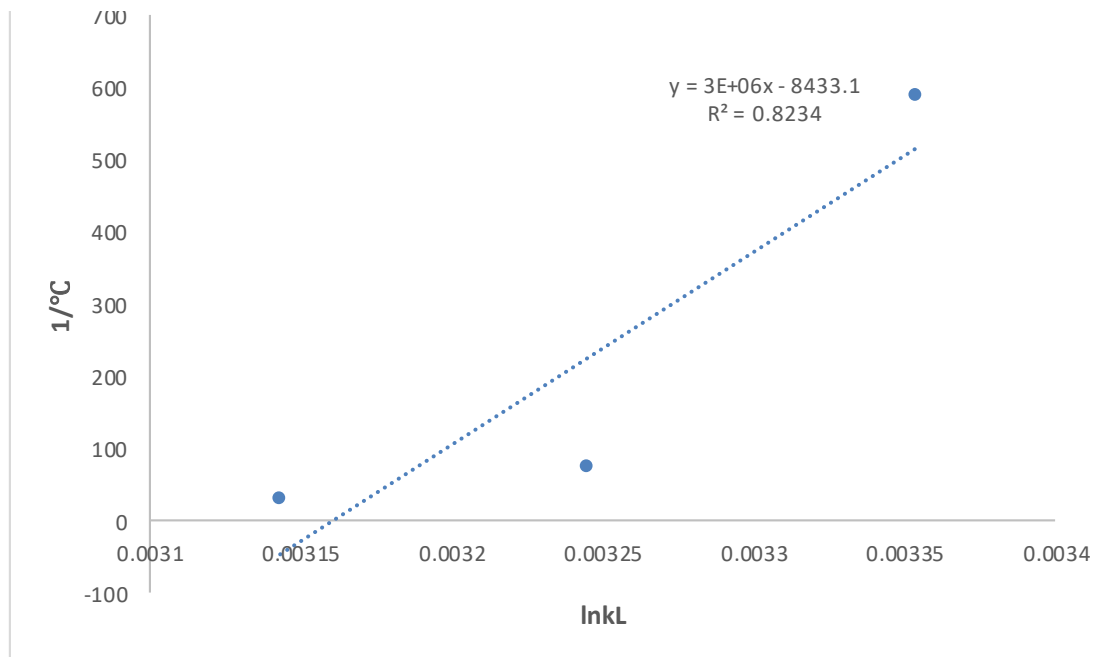


Figure 34. Plot for the calculation of the thermodynamic parameters ΔS° and ΔH° of Boron adsorption onto IL-CNC@DP.

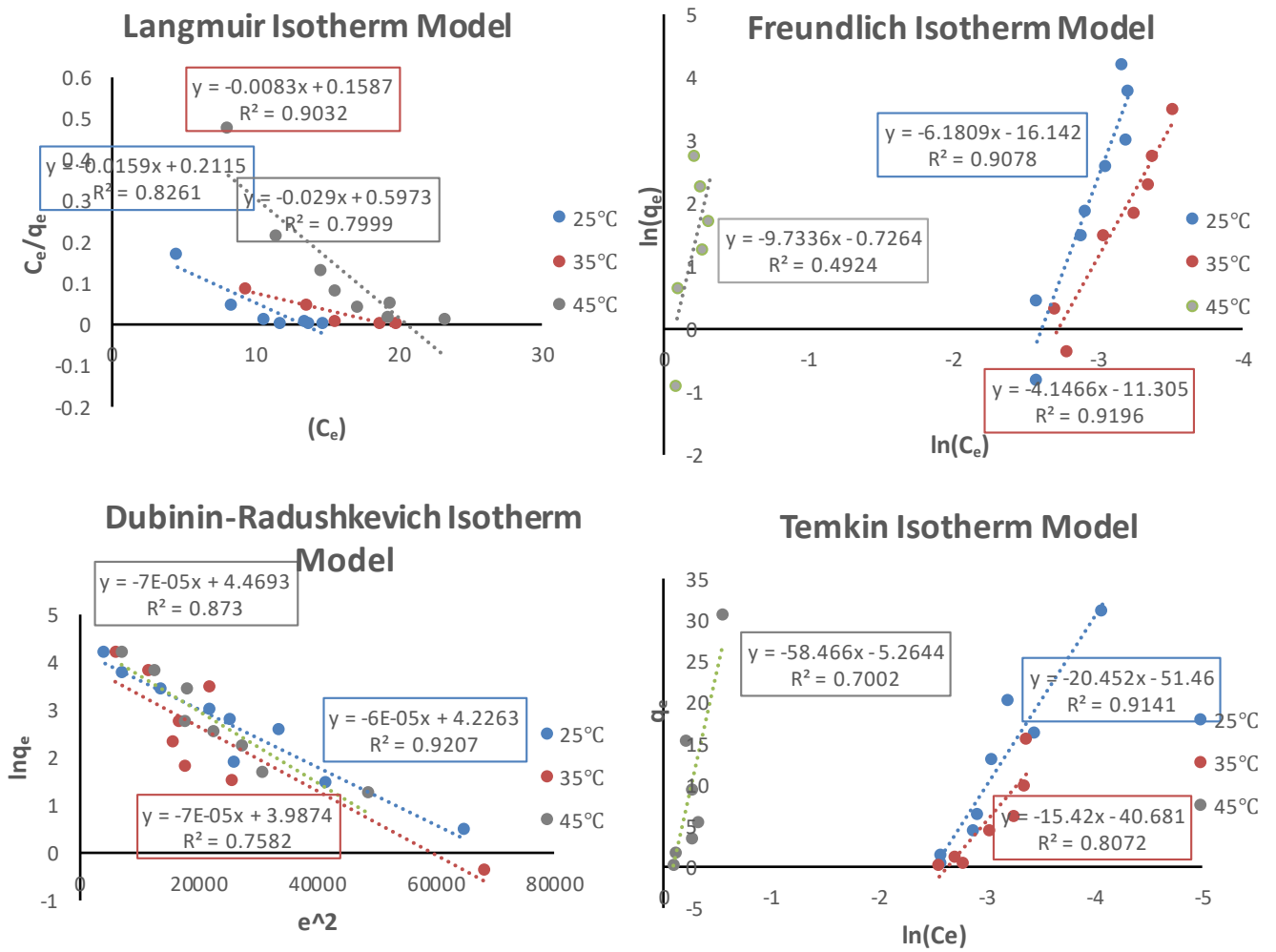


Figure 35. Adsorption isotherm models used in the current study of the adsorption of B^{3+} metal ions onto RDP.

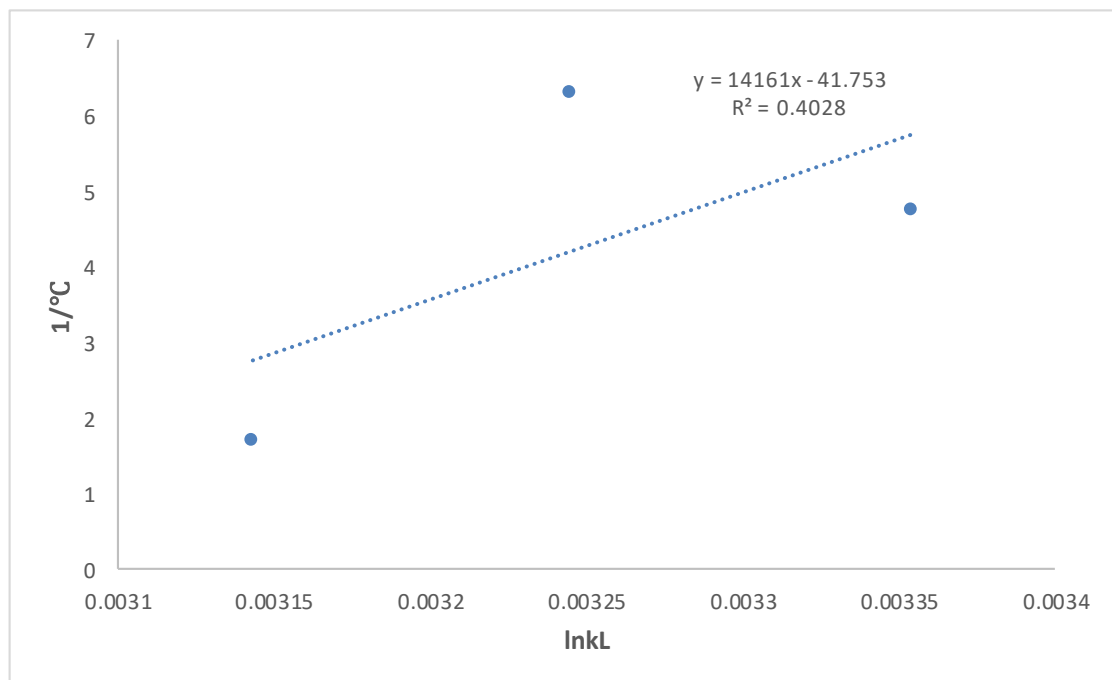


Figure 36. Plot for the calculation of the thermodynamic parameters ΔS° and ΔH° of Boron adsorption onto RDP.

4.7 Desorption studies of Li¹⁺, Mo⁶⁺, & B³⁺

An important feature for any adsorbent material is the reusability of it because it determines the cost of treatment. In other words, if the adsorbent can be reused multiple times, thus the cost of treatment per unit volume of treated water is lower (Khan and Lo, 2016). Moreover, reusability considers three critical parameters: desorption, recovery, and stability of the adsorbent. The process of desorption is the complete opposite of adsorption since it involves the release of the adsorbed substances from its surface. Therefore, providing adsorption sites, where the adsorbent can be regenerated and reused again (Badsha et al., 2020). In this study, the main objective is to investigate the desorption process by using 0.5M and 1M HCl as eluents since it has been used for the desorption of metals for Li¹⁺, Mo⁶⁺, & B³⁺ from spent IL-CNC@DP and RDP (Lin, & Lien, 2013). Tables 17, 18, and 19 demonstrates the percentage desorption for Li⁺, Mo⁶⁺, & B³⁺, respectively, using 0.5M and 1M HCl. The desorption calculation was performed as per equation (8).

From Table 17, it is evident that all the adsorbents achieved a desorption percentage of 99% and higher under both concentrations. This proves that the desorption process was not influenced by different HCl concentrations. It is further supported by the statistical findings that were used to assess the significance between the two concentrations. A single-factor test was conducted to study the effect of using 0.5M and 1M HCl for each adsorbent. The results show that no significant difference was found at a p-value of 0.16. Furthermore, the high desorption efficiency suggests that the mechanism adsorption of Li⁺ metals onto IL-CNC@DP and RDP was mainly a physical adsorption process and that the binding of the metals was weak (Badsha et al., 2020; Carvalho et al., 2020). In the end, both adsorbents can be regenerated and reused; making them economically feasible and environmentally friendly (Kyzas & Kostoglou,

2014). Furthermore, recovery of Li^{1+} metals for other applications can be employed. As for Mo^{6+} desorption in Table 18, the desorption efficiency under different concentrations for IL-CNC@DP and RDP demonstrated different results. The modified adsorbent, IL-CNC@DP, under both concentrations, achieved a desorption percentage of 98% and higher. On the other hand, the unmodified adsorbent, RDP, under 0.5M HCL achieved 97% and under 1M HCl achieved 96%. The differences between the concentrations are also not significant for both adsorbents since the p-value was found to be 0.71. Comparing the desorption efficiencies for Mo^{6+} , the highest was achieved by the modified adsorbent indicating that the adsorption bonding between Mo^{6+} and IL-CNC@RDP could be weaker than RDP. Nonetheless, both adsorbents demonstrated high desorption efficiencies. Lastly, the desorption efficiency of B^{3+} presented significant results. It is the only metal that did not desorb as can be seen in Table 19. The desorption efficiency is approximately zero implying that it was mainly a chemical adsorption process and that the binding of the B^{3+} metals was strong (Liang et al., 2021). This can also mean that the adsorbent will not be effectively reused again. Nonetheless, this can imply that the type of eluent used for the desorption was not effective towards B^{3+} . Other eluents that could be employed in the desorption experiment towards B^{3+} can include H_2SO_4 , HNO_3 , EDTA, and thiourea (Lin, & Lien, 2013). These eluents are reported to be noteworthy in the recovery of metals, hence future experiments can be performed using the mentioned eluents for the desorption of B^{3+} .

In conclusion, the findings of this study prove that Li^{1+} and Mo^{6+} had high desorption efficiencies from all the adsorbents at both concentrations, whereas B^{3+} did not show any desorption capabilities. Therefore, the spent adsorbent of Li^{1+} and Mo^{6+} metals can be reused for future adsorption processes and the recovery of these metals can occur. Bearing in mind that they also demonstrate exceptional adsorptive capacities as

mentioned previously in the study. However, using 0.5M and 1M HCl towards B³⁺ was not effective implying that different eluents should be tested in the future.

Table 17. Effect of different eluant concentrations on Li¹⁺ desorption efficiency (%) onto IL-CNC@DP and RDP.

Adsorbent	Eluent concentration	Average adsorbed concentration (mg/L)	% Desorption
IL-CNC@DP	0.5M HCl	35.27	99.920
	1M HCl		99.994
RDP	0.5M HCl	14.44	99.923
	1M HCl		99.993

Table 18. Effect of different eluant concentrations on Mo⁶⁺ desorption efficiency (%) onto IL-CNC@DP and RDP.

Adsorbent	Eluent concentration	Average adsorbed concentration (mg/L)	% Desorption
IL-CNC@DP	0.5M HCl	35.54	98.483
	1M HCl		98.278
RDP	0.5M HCl	32.86	97.194
	1M HCl		96.595

Table 19. Effect of different eluant concentrations on B³⁺ desorption efficiency (%) onto IL-CNC@DP and RDP.

Adsorbent	Eluent concentration	Average adsorbed concentration (mg/L)	% Desorption
IL-CNC@DP	0.5M HCl	34.78	≈ 0
	1M HCl		≈ 0
RDP	0.5M HCl	20.28	≈ 0
	1M HCl		≈ 0

4.8 Application of RDP and IL-CNC@RDP to a real groundwater sample

The adsorption of specific metals on an adsorbent is typically affected by the occurrence of other ions. This is due to the competition that might occur between the ions onto the adsorbents binding sites (Naeimi & Faghihian, 2017). In fact, most papers refer to it as the selectivity of targeted ions towards an adsorbent with the presence of other background ions. Moreover, high selectivity is necessary for any adsorptive treatment specifically towards heavy metals, whose remediation from the environment is a major concern (Badsha et al., 2020). Therefore, investigating the selectivity of metal adsorption is very critical since higher selectivity tends to make the most of the active sites of the adsorbent, while simultaneously recovering metals from the solution.

In this study, groundwater (GW) samples were obtained from the northern wells to evaluate Qatar's groundwater quality (Ahmad et al., 2020). Hence, multi-element analysis of the groundwater sample was performed, and the results are illustrated in Figure 37. It was important to investigate the adsorption selectivity of the modified IL-CNC@DP adsorbent and unmodified RDP adsorbent between those co-existed cations and Li^+ , Mo^{6+} , & B^{3+} . It can be seen that twelve elements were detected by the ICP-OES and that in general the modified adsorbent (IL-CNC@DP) and the unmodified adsorbent (RDP) is not selective only towards the three studied metals. For example, Sr, Mg, and Ga concentration after the addition of IL-CNC@DP decreased slightly in comparison to RDP. This suggests that IL-CNC@DP can be used to treat other cations better than RDP implying that the adsorbent is capable of working effectively even in a matrix of various ions. On the other hand, some cations in the groundwater are not properly adsorbed by the modified adsorbent and they remained unchanged once the unmodified adsorbent was added. For example, Ca was found to be 643 mg/L in the groundwater sample even after the addition of the unmodified adsorbent, whereas the

concentration slightly changed after the addition of the modified adsorbent to 641 mg/L. This implies that only the modified adsorbent can be effective towards Ca. Furthermore, K and In concentrations remained unchanged after the addition of the unmodified adsorbent, whereas the concentration slightly changed after the addition of the modified adsorbent. As for Na, it is the highest ion detected in the groundwater sample at 4526 mg/L. After the adsorption by IL-CNC@DP, the concentration of Na dropped to 4208 mg/L. This result is significant since the modified adsorbent is effective towards large quantities of Na ions. Furthermore, after the adsorption by RDP, the concentration also dropped to 4459, implying that the unmodified adsorbent can be employed towards Na. In addition, Al cation is slightly effective towards RDP than IL-CNC@DP in the presence of other ions, whereas Ba cation did not significantly change after the addition of both adsorbents. In the end, this depends upon the different mechanisms of adsorption of each metal according to their physicochemical properties.

A closer look at Figure 38 demonstrates the differences in their concentrations of the three metals towards IL-CNC@DP and RDP. The Mo concentration in the groundwater was 0.05 mg/L and after the addition of the modified adsorbent, the concentration decreased to 0.01 mg/L. While for the unmodified adsorbent, the concentration decreased to 0.02 mg/L. B concentration was 1.760 mg/L, after adsorption by the modified adsorbent, it drastically changed to 1.701 mg/L, where in comparison with the unmodified adsorbent it remained higher at 1.743 mg/L. As for Li the concentration, 0.255 mg/L after the adsorption by the modified adsorbent decreased slightly to 0.246 mg/L, where in comparison with the unmodified adsorbent it remained higher at 0.250 mg/L. It is clear that the presence of other ions in the groundwater samples is influenced by the addition of both adsorbents. Moreover, the differences between the concentrations of IL-CNC@DP and RDP in comparison to the groundwater sample are

not that significant. This means that the availability of other ions in the groundwater sample compete with Li^{1+} , Mo^{6+} , & B^{3+} for the active sites onto both adsorbents. This can also decrease the adsorption efficiency and capacity of the three metals if other ions are found in the solution.

In conclusion, the modified adsorbent is not only selective towards the three pollutants of interest (Li^{1+} , Mo^{6+} , & B^{3+}) but rather towards a wide range of cations. This implies that the modified adsorbent can be used to treat groundwater samples in Qatar that contain a variety of cations depending upon the targeted metals of interest. Furthermore, it is less time-consuming to treat multiple elements at a time. This is also practical since it demonstrates the real scenario of the groundwater systems in which the modified adsorbent has the capability to cope with other co-existing ions. Overall, according to the full elemental analysis obtained, IL-CNC@DP can be selective towards Sr, Mg, Ga, and slightly selective towards Ca, K, In, and greatly towards Na. As for RDP, it is also not only selective towards Li^{1+} , Mo^{6+} , & B^{3+} since it can be shown that all the other elements have slightly changed in their concentrations except for Ca, K, and In. This implies that RDP can still be used in groundwater treatments but IL-CNC@DP is more favorable towards other co-existing ions.

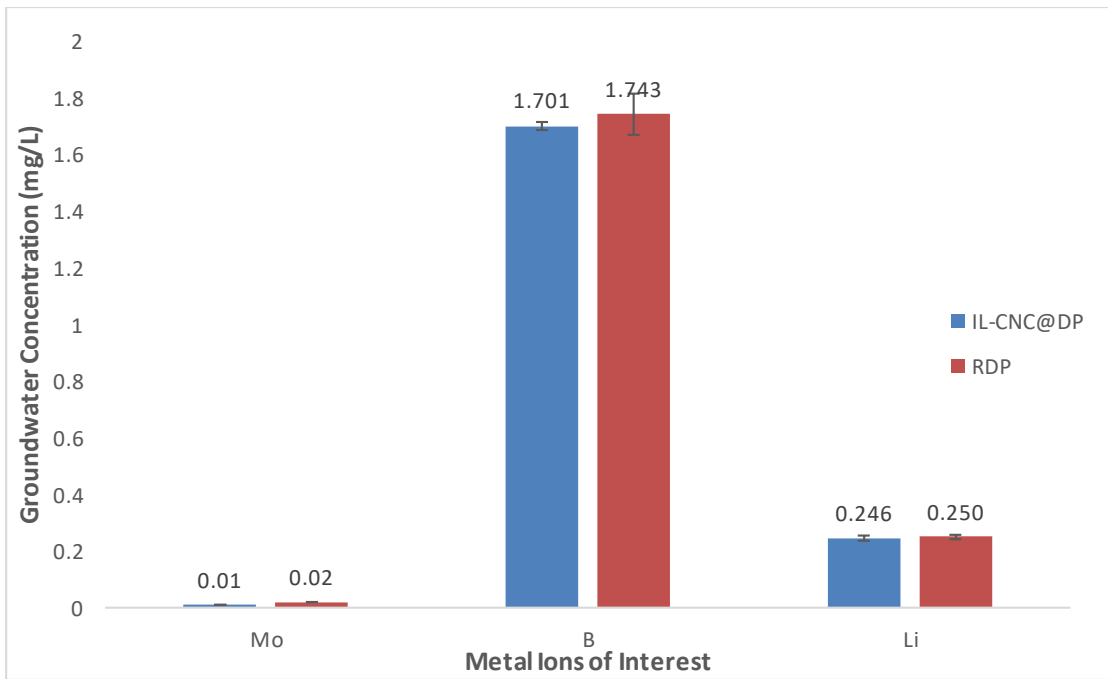


Figure 37. Groundwater concentration comparison for IL-CNC@DP and RDP for Li¹⁺, Mo⁶⁺, & B³⁺ in the presence of other available ions.

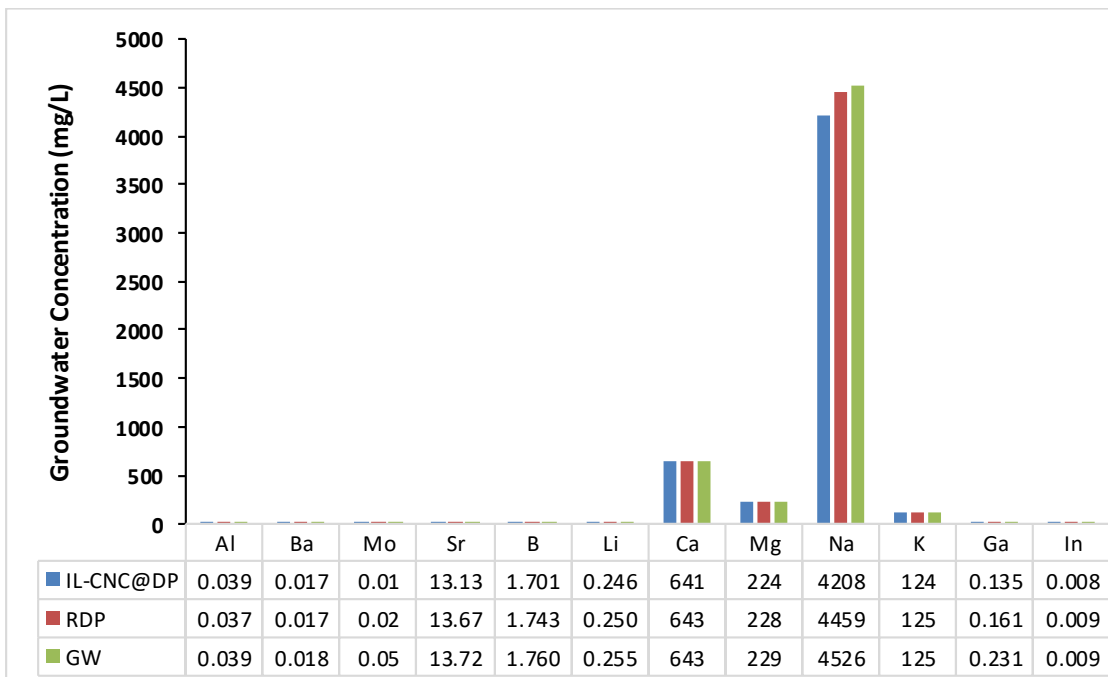


Figure 38. Multi-element analysis for groundwater sample before and after adsorption by IL-CNC@DP and RDP.

CHAPTER 5: CONCLUSION

This study is considered to be the first of its kind as it demonstrated a modified novel adsorbent (IL-CNC@DP). CNCs have been successfully isolated from RDP by sulfuric acid hydrolysis under methods 1 and 2. Furthermore, this adsorbent can be used to treat groundwater from heavy metal contamination by making use of agricultural wastes such as date pits. The preparation of the adsorbent is cost-effective and environmentally friendly. According to the results, Li^{1+} , Mo^{6+} , and B^{3+} ions from groundwater can be effectively remediated at high percentage removal by using the modified adsorbent in comparison to RDP. The effect of pH and initial concentration had an impact on the adsorption of the three metals, while the effect of temperature did not impact the adsorption significantly. Therefore at 25 °C at an initial concentration of 100 mg/L, Li^{1+} reached 99 mg/g, Mo^{6+} reached 89 mg/g, and B^{3+} 89 mg/g. Considering all parameters and temperatures, we can conclude that the highest adsorption capacity (q_e) was at 100 mg/L at pH 6 for IL-CNC@DP, where their uptake capacity order was: $\text{Li}^{1+} > \text{B}^{3+} > \text{Mo}^{6+}$. Furthermore, the thermodynamics constants for all metals of the modified adsorbent proved that the reaction is exothermic, does not favor a high level of disorder, and is spontaneous in nature. Langmuir, Freundlich, Dubinin–Radushkevich, and Temkin isotherm models were successfully used to find the best-fit model and the results varied according to each metal physiochemical characteristics. Moreover, desorption studies were carried for all the metals, where they proved that Li^{1+} and Mo^{6+} are capable of being desorbed but B^{3+} isn't. The last experiment investigated the selectivity of the modified adsorbent towards real groundwater sample isolated in Qatar and the results demonstrate that the adsorbent could be effective towards a wide range of cations. Finally, characterization by SEM, BET and FTIR proved that the modified adsorbent was improved due to the

enhanced of its surface morphology, an increase of surface area, and presence of functional groups. In this current study, IL-CNC@DP confirmed exceptional results proving that the modification enhanced the remediation of the metals from water and these results could play an important role in Qatar National Vision (2030) and Qatar National Development Strategy (2018-2022).

REFERENCES

- Abdel-Satar, A. M., Al-Khabbas, M. H., Alahmad, W. R., Yousef, W. M., Alsomadi, R. H., & Iqbal, T. (2017). Quality assessment of groundwater and agricultural soil in Hail region, Saudi Arabia. *The Egyptian Journal of Aquatic Research*, 43(1), 55-64.
- Abdolali, A., Ngo, H.H., Guo, W., Lu, S., Chen, S.S., Nguyen, N.C., Zhang, X., Wang, J., Wu, Y. (2016) A breakthrough biosorbents in removing heavy metals: equilibrium, kinetic, thermodynamic and mechanism analyses in a lab-scale study, *Sci. Total Environ.* 542, 603–611.
- Abdul Rahman, N. H., Chieng, B. W., Ibrahim, N. A., & Abdul Rahman, N. (2017). Extraction and characterization of cellulose nanocrystals from tea leaf waste fibers. *Polymers*, 9(11), 588.
- Abraham, E., Deepa, B., Pothan, L.A., Jacob, M., Thomas, S., Cvelbar, U., Anandjiwala, R. (2011). Extraction of nanocellulose fibrils from lignocellulosic fibres: a novel approach. *Carbohydrate Polymers*, 86, 1468–1475
- Abraham, E., Deepa, B., Pothan, L. A., Cintil, J., Thomas, S., John, M. J., ... & Narine, S. S. (2013). Environmental friendly method for the extraction of coir fibre and isolation of nanofibre. *Carbohydrate polymers*, 92(2), 1477-1483.
- Abu-Thabit, N. Y., Judeh, A. A., Hakeem, A. S., Ul-Hamid, A., Umar, Y., & Ahmad, A. (2020). Isolation and characterization of microcrystalline cellulose from date seeds (*Phoenix dactylifera* L.). *International Journal of Biological Macromolecules*.
- Adel, A. M., Abd El-Wahab, Z. H., Ibrahim, A. A., & Al-Shemy, M. T. (2011). Characterization of microcrystalline cellulose prepared from lignocellulosic materials. Part II: Physicochemical properties. *Carbohydrate Polymers*, 83(2), 676-687.
- Aguayo, M., Fernández Pérez, A., Reyes, G., Oviedo, C., Gacitúa, W., Gonzalez, R., & Uyarte, O. (2018). Isolation and Characterization of Cellulose Nanocrystals from Rejected

Fibers Originated in the Kraft Pulping Process. *Polymers*, 10(10), 1145.

Ahmad, A. Y., Al-Ghouthi, M. A., Khraisheh, M., & Zouari, N. (2020). Hydrogeochemical characterization and quality evaluation of groundwater suitability for domestic and agricultural uses in the state of Qatar. *Groundwater for Sustainable Development*, 11, 100467.

Ahmad, T., Danish, M., Rafatullah, M., Ghazali, A., Sulaiman, O., Hashim, R., & Ibrahim, M. N. (2011). The use of date palm as a potential adsorbent for wastewater treatment: A review. *Environmental Science and Pollution Research*, 19(5), 1464-1484. doi:10.1007/s11356-011-0709-8

Alavi, M. (2019). Modifications of microcrystalline cellulose (MCC), nanofibrillated cellulose (NFC), and nanocrystalline cellulose (NCC) for antimicrobial and wound healing applications. *e-Polymers*, 19(1), 103-119.

Aldawsari, A., Khan, M. A., Hameed, B. H., Alqadami, A. A., Siddiqui, M. R., Alothman, Z. A., & Ahmed, A. Y. B. H. (2017). Mercerized mesoporous date pit activated carbon—A novel adsorbent to sequester potentially toxic divalent heavy metals from water. *PLoS one*, 12(9).

Al-Ghouthi, M. A., & Al-Absi, R. S. (2020). Mechanistic understanding of the adsorption and thermodynamic aspects of cationic methylene blue dye onto cellulosic olive stones biomass from wastewater. *Scientific Reports*, 10(1), 1-18.

Al-Ghouthi, M. A., & Da'ana, D. A. (2020). Guidelines for the use and interpretation of adsorption isotherm models: A review. *Journal of hazardous materials*, 393, 122383.

Al-Ghouthi, M. A., Al Disi, Z. A., Al-Kaabi, N., & Khraisheh, M. (2017). Mechanistic insights into the remediation of bromide ions from desalinated water using roasted date pits. *Chemical Engineering Journal*, 308, 463-475.

Al-Ghouthi, M. A., Al-Degs, Y. S., Khraisheh, M. A., Ahmad, M. N., & Allen, S. J. (2009).

- Mechanisms and chemistry of dye adsorption on manganese oxides-modified diatomite. *Journal of environmental management*, 90(11), 3520-3527.
- Al-Ghouti, M. A., Da'ana, D., Abu-Dieyeh, M., & Khraisheh, M. (2019). Adsorptive removal of mercury from water by adsorbents derived from date pits. *Scientific reports*, 9(1), 1-15.
- Al-Ghouti, M., Li, J., Salamh, Y., Al-Laqtah, N., Walker, G., & Ahmad, M. (2010). Adsorption mechanisms of removing heavy metals and dyes from aqueous solution using date pits solid adsorbent. *Journal Of Hazardous Materials*, 176(1-3), 510-520. doi: 10.1016/j.jhazmat.2009.11.059.
- Al-Maadheed, S., Goktepe, I., Latiff, A. B. A., & Shomar, B. (2019). Antibiotics in hospital effluent and domestic wastewater treatment plants in Doha, Qatar. *Journal of Water Process Engineering*, 28, 60-68.
- Anantha, M. S., Olivera, S., Hu, C., Jayanna, B. K., Reddy, N., Venkatesh, K., ... & Naidu, R. (2020). Comparison of the photocatalytic, adsorption and electrochemical methods for the removal of cationic dyes from aqueous solutions. *Environmental Technology & Innovation*, 17, 100612.
- Araki, J., & Miyayama, M. (2020). Wet spinning of cellulose nanowhiskers; fiber yarns obtained only from colloidal cellulose crystals. *Polymer*, 188, 122116.
- Ardanuy Raso, M., Claramunt Blanes, J., Arévalo Peces, R., Parés Sabatés, F., Aracri, E., & Vidal Lluçia, T. (2012). Nanofibrillated cellulose (NFC) as a potential reinforcement for high performance cement mortar composites. *BioResources*, 7(3), 3883-3894.
- Asim, S., Wasim, M., Sabir, A., Shafiq, M., Andlib, H., Khuram, S., ... & Jamil, T. (2018). The effect of Nanocrystalline cellulose/Gum Arabic conjugates in crosslinked membrane for antibacterial, chlorine resistance and boron removal performance. *Journal of hazardous materials*, 343, 68-77.

- Ates, N., & Uzal, N. (2018). Removal of heavy metals from aluminum anodic oxidation wastewaters by membrane filtration. *Environmental Science and Pollution Research*, 25(22), 22259-22272.
- Ayotte, J. D., Gronberg, J. M., & Apodaca, L. E. (2011). *Trace elements and radon in groundwater across the United States, 1992-2003* (p. 115). US Department of the Interior, US Geological Survey.
- Baalousha, H. M. (2016). Groundwater vulnerability mapping of Qatar aquifers. *Journal of African Earth Sciences*, 124, 75-93.
- Baalousha, H. M., & Ouda, O. K. (2017). Domestic water demand challenges in Qatar. *Arabian Journal of Geosciences*, 10(24), 537.
- Badsha, M. A., Khan, M., Wu, B., Kumar, A., & Lo, I. M. (2020). Role of surface functional groups of hydrogels in metal adsorption: From performance to mechanism. *Journal of Hazardous Materials*, 124463.
- Bai L., Liu Y., Ding A., Ren N., Li G., Liang H. (2019). Surface coating of UF membranes to improve antifouling properties: A comparison study between cellulose nanocrystals (CNCs) and cellulose nanofibrils (CNFs). *Chemosphere* 217, 76-84.
- Beck-Candanedo, S., Roman, M., & Gray, D. G. (2005). Effect of reaction conditions on the properties and behavior of wood cellulose nanocrystal suspensions. *Biomacromolecules*, 6(2), 1048-1054.
- Bhatnagar, A., Hogland, W., Marques, M., & Sillanpää, M. (2013). An overview of the modification methods of activated carbon for its water treatment applications. *Chemical Engineering Journal*, 219, 499-511.
- Biswas, A. K., & Tortajada, C. (2019). Water crisis and water wars: Myths and realities.
- Blüml, V., Regier, M. D., Hlavin, G., Rockett, I. R., König, F., Vyssoki, B., ... & Kapusta, N. D. (2013). Lithium in the public water supply and suicide mortality in Texas. *Journal*

- of psychiatric research, 47(3), 407-411.
- Börjesson, M., & Westman, G. (2015). Crystalline nanocellulose—preparation, modification, and properties. *Cellulose-fundamental aspects and current trends*, 159-191.
- Brinchi, L., Cotana, F., Fortunati, E., & Kenny, J. M. (2013). Production of nanocrystalline cellulose from lignocellulosic biomass: technology and applications. *Carbohydrate polymers*, 94(1), 154-169.
- Brion-Roby, R., Gagnon, J., Nosrati, S., Deschenes, J. S., & Chabot, B. (2018). Adsorption and desorption of molybdenum (VI) in contaminated water using a chitosan sorbent. *Journal of Water Process Engineering*, 23, 13-19.
- Brito, B. S., Pereira, F. V., Putaux, J. L., & Jean, B. (2012). Preparation, morphology and structure of cellulose nanocrystals from bamboo fibers. *Cellulose*, 19(5), 1527-1536.
- Bushra, R., Ahmed, A., & Shahadat, M. (2016). Mechanism of adsorption on nanomaterials. In *Advanced Environmental Analysis* (pp. 90-111).
- Carpenter, A. W., de Lannoy, C. F., & Wiesner, M. R. (2015). Cellulose nanomaterials in water treatment technologies. *Environmental science & technology*, 49(9), 5277-5287.
- Carrillo, I., Mendonça, R. T., Ago, M. & Rojas, O. J. (2018). Comparative study of cellulosic components isolated from different Eucalyptus species. *Cellulose*, 25, 1011–1029.
- Carvalho, T., Pereira, A. D. S., Bonomo, R. C., Franco, M., Finotelli, P. V., & Amaral, P. F. (2020). Simple physical adsorption technique to immobilize *Yarrowia lipolytica* lipase purified by different methods on magnetic nanoparticles: Adsorption isotherms and thermodynamic approach. *International Journal of Biological Macromolecules*, 160, 889-902.
- Castro, L., Blázquez, M. L., González, F., Muñoz, J. A., & Ballester, A. (2018). Heavy metal adsorption using biogenic iron compounds. *Hydrometallurgy*, 179, 44-51.
- Cervin, N. T., Aulin, C., Larsson, P. T., & Wågberg, L. (2012). Ultra porous nanocellulose

- aerogels as separation medium for mixtures of oil/water liquids. *Cellulose*, 19(2), 401-410.
- Chandra, J., George, N., & Narayanankutty, S. K. (2016). Isolation and characterization of cellulose nanofibrils from arecanut husk fibre. *Carbohydrate polymers*, 142, 158-166.
- Chandra, M. R. G. S., & Madakka, M. (2019). Comparative Biochemistry and Kinetics of Microbial Lignocellulolytic Enzymes. In *Recent Developments in Applied Microbiology and Biochemistry* (pp. 147-159). Academic Press.
- Chao, L., Wang, Y., Cao, Y., & Li, Y. (2020). Adsorption of molybdenum (VI) in contaminated water using Fe₃O₄/CTS magnetic nanoparticles. In *E3S Web of Conferences* (Vol. 165, p. 05032). EDP Sciences.
- Chen, W., Yu, H., & Liu, Y. (2011). Preparation of millimeter-long cellulose I nanofibers with diameters of 30–80 nm from bamboo fibers. *Carbohydrate polymers*, 86(2), 453-461.
- Chong, M. F., Lee, K. P., Chieng, H. J., & Ramli, I. I. S. B. (2009). Removal of boron from ceramic industry wastewater by adsorption–flocculation mechanism using palm oil mill boiler (POMB) bottom ash and polymer. *Water research*, 43(13), 3326-3334.
- Coetsiers, M., & Walraevens, K. (2008). 12 The Neogene Aquifer, Flanders, Belgium. *Natural groundwater quality*, 263.
- Colburn, A. S., Meeks, N., Weinman, S. T., & Bhattacharyya, D. (2016). High total dissolved solids water treatment by charged nanofiltration membranes relating to power plant applications. *Industrial & engineering chemistry research*, 55(14), 4089-4097.
- Coll, M. T., Fortuny, A., & Sastre, A. M. (2014). Boron reduction by supported liquid membranes using ALiCY and ALiDEC ionic liquids as carriers. *Chemical Engineering Research and Design*, 92(4), 758-763.
- Collazo-Bigliardi, S., Ortega-Toro, R., & Chiralt Boix, A. (2018). Isolation and characterisation of microcrystalline cellulose and cellulose nanocrystals from coffee

- husk and comparative study with rice husk. *Carbohydrate Polymers*, 191, 205-215.
- Crini, G., Lichtfouse, E., Wilson, L. D., & Morin-Crini, N. (2019). Conventional and non-conventional adsorbents for wastewater treatment. *Environmental Chemistry Letters*, 17(1), 195-213.
- Crouter, A., & Briens, L. (2014). The effect of moisture on the flowability of pharmaceutical excipients. *Aaps Pharmscitech*, 15(1), 65-74.
- Daicho, K., Kobayashi, K., Fujisawa, S., & Saito, T. (2019). Crystallinity-Independent yet Modification-Dependent True Density of Nanocellulose. *Biomacromolecules*, 21(2), 939-945.
- Darwish, M. A., & Mohtar, R. (2013). Qatar water challenges. *Desalination and Water Treatment*, 51(1-3), 75-86.
- Das, S. (2014). Lithium in Groundwater of Rajasthan. *Journal of the Geological Society of India*, 83(1), 116-116.
- de Farias Silva, C. E., da Gama, B. M. V., da Silva Gonçalves, A. H., Medeiros, J. A., & de Souza Abud, A. K. (2020). Basic-dye adsorption in albedo residue: effect of pH, contact time, temperature, dye concentration, biomass dosage, rotation and ionic strength. *Journal of King Saud University-Engineering Sciences*, 32(6), 351-359.
- de Melo, M. C., & da Silva, M. M. (2008). 11 The Aveiro Quaternary and Cretaceous Aquifers, Portugal. *Natural groundwater quality*, 233.
- Deepa, B., Abraham, E., Cordeiro, N., Mozetic, M., Mathew, A. P., Oksman, K., ... & Pothan, L. A. (2015). Utilization of various lignocellulosic biomass for the production of nanocellulose: a comparative study. *Cellulose*, 22(2), 1075-1090.
- Deetlefs, M., & Seddon, K. R. (2010). Assessing the greenness of some typical laboratory ionic liquid preparations. *Green Chemistry*, 12(1), 17-30.
- Deshmukh, P.D., Khadse, G.K., Shinde, V.S., Labhasetwar, P. (2017) Cadmium removal from

- aqueous solutions using dried banana peels as an adsorbent: kinetics and equilibrium modelling, *J. Bioremediat. Biodegrad.* 8, 395.
- Dharmalingam, K., Padmavathi, G., Kunnumakkara, A. B., & Anandalakshmi, R. (2019). Microwave-assisted synthesis of cellulose/zinc-sulfate-calcium-phosphate (ZSCAP) nanocomposites for biomedical applications. *Materials Science and Engineering: C*, 100, 535-543.
- Díez, D., Urueña, A., Piñero, R., Barrio, A., & Tamminen, T. (2020). Determination of Hemicellulose, Cellulose, and Lignin Content in Different Types of Biomasses by Thermogravimetric Analysis and Pseudocomponent Kinetic Model (TGA-PKM Method). *Processes*, 8(9), 1048.
- Ditzel F.I, Prestes E., Carvalho B.M., Demiate I.M, Pinheiro L.A. (2017). Nanocrystalline cellulose extracted from pine wood and corncob, *Carbohydr. Polym.* 157, 1577–1585.
- Dong S., Bortner M.J., Roman M. (2016). Analysis of the sulfuric acid hydrolysis of wood pulp for cellulose nanocrystal production: a central composite design study, *Ind.Crop. Prod.* 93, 76–87.
- Dong, X. M., Revol, J. F., & Gray, D. G. (1998). Effect of microcrystallite preparation conditions on the formation of colloid crystals of cellulose. *Cellulose*, 5(1), 19-32.
- Dufresne, A. (2017). *Nanocellulose: from nature to high performance tailored materials*. Walter de Gruyter GmbH & Co KG.
- Dutta, A., Diao, Y., Jain, R., Rene, E.R., Dutta, S. (2016) Adsorption of cadmium from aqueous solutions onto coffee grounds and wheat straw: equilibrium and kinetic study, *J. Environ. Eng.* 142, 1–6.
- Eggermont, S. G., Prato, R., Dominguez-Benetton, X., & Fransaeer, J. (2020). Metal removal from aqueous solutions: insights from modeling precipitation titration curves. *Journal of Environmental Chemical Engineering*, 8(1), 103596.

- Ekka, B., Dhaka, R. S., Patel, R. K., & Dash, P. (2017). Fluoride removal in waters using ionic liquid-functionalized alumina as a novel adsorbent. *Journal of Cleaner Production*, *151*, 303-318.
- El Alfy, M., Lashin, A., Abdalla, F., & Al-Bassam, A. (2017). Assessing the hydrogeochemical processes affecting groundwater pollution in arid areas using an integration of geochemical equilibrium and multivariate statistical techniques. *Environmental Pollution*, *229*, 760-770.
- Eldos, H. I., Ashfaq, M. Y., & Al-Ghouti, M. A. (2020). Rapid assessment of the impact of microwave heating coupled with UV-C radiation on the degradation of PAHs from contaminated soil using FTIR and multivariate analysis. *Arabian Journal of Chemistry*, *13*(11), 7609-7625.
- Elsaid, K., Shamruk, M., Elkamel, A., Abdel-Wahab, A. (2017) Assessment of Groundwater quality in the State of Qatar for agriculture and domestic water supply applying membrane processes. Proceedings of the 12th Gulf Water Conference, Manama, Bahrain.
- Etale, A., Nhlane, D., Mosai, A. K., & Nuapia, Y. (2020). Cellulose-supported ferrihydrites for the removal of As (III), As (V) and Cr (VI) from mining-contaminated water.
- Evans, S., Wesley, O., Nathan, O., & Moloto, M. (2019). Chemically purified cellulose and its nanocrystals from sugarcane baggase: isolation and characterization. *Heliyon*, *5*(10), e02635.
- Fakhfakh, J., Ben-Youssef, S., Naushad, M., & Allouche, N. (2019). Different Extraction Methods, Physical Properties and Chemical Composition of Date Seed Oil. In *Sustainable Agriculture Reviews 34* (pp. 125-153). Springer, Cham.
- Fei, Z., Geldbach, T. J., Zhao, D., & Dyson, P. J. (2006). From dysfunction to bis-function: on the design and applications of functionalised ionic liquids. *Chemistry—A European*

Journal, 12(8), 2122-2130.

- Ferreira, F. V., Pinheiro, I. F., Gouveia, R. F., Thim, G. P., & Lona, L. M. F. (2018). Functionalized cellulose nanocrystals as reinforcement in biodegradable polymer nanocomposites. *Polymer Composites*, 39, E9-E29.
- Flauzino Neto, W., Silvério, H., Dantas, N., & Pasquini, D. (2013). Extraction and characterization of cellulose nanocrystals from agro-industrial residue – Soy hulls. *Industrial Crops And Products*, 42, 480-488.
- Freemantle, M. (2010). *An introduction to ionic liquids*. Royal Society of chemistry.
- Fritzmann, C., Löwenberg, J., Wintgens, T., & Melin, T. (2007). State-of-the-art of reverse osmosis desalination. *Desalination*, 216(1-3), 1-76.
- Fu, Q., Yan, M., Jungstedt, E., Yang, X., Li, Y., Berglund, L. (2018). Transparent plywood as a load-bearing and luminescent biocomposites. *Composites Science and Technology*, 164, 296-303.
- Galitskaya, I. V., Kostikova, I. A., Pozdnyakova, I. A., & Zhigalin, A. D. (2013). The role of rock in chemical and isotopic composition of groundwater in the vicinity of radioactive waste disposal site. *Procedia Earth and Planetary Science*, 7, 276-279.
- Gao, A., Chen, H., Tang, J., Xie, K., & Hou, A. (2020). Efficient extraction of cellulose nanocrystals from waste *Calotropis gigantea* fiber by SO₄²⁻/TiO₂ nano-solid superacid catalyst combined with ball milling exfoliation. *Industrial Crops And Products*, 152, 112524.
- García, A., Gandini, A., Labidi, J., Belgacem, N., & Bras, J. (2016). Industrial and crop wastes: A new source for nanocellulose biorefinery. *Industrial Crops and Products*, 93, 26-38.
- Gelvin, R., & Novak, D. (2001). Advanced Treatment for Groundwater: Treating Low-Quality Groundwater for Municipal Use. *Water Engineering & Management*, 148(11), 28-29.
- George, J., & Sabapathi, S. N. (2015). Cellulose nanocrystals: synthesis, functional properties,

and applications. *Nanotechnology, science and applications*, 8, 45.

- Gholami-Bonabi, L., Ziaefar, N., & Sheikhloie, H. (2020). Removal of phenol from aqueous solutions by magnetic oxide graphene nanoparticles modified with ionic liquids using the Taguchi optimization approach. *Water Science and Technology*, 81(2), 228-240.
- Girish, C. R., & Murty, V. R. (2016). Mass transfer studies on adsorption of phenol from wastewater using Lantana camara, forest waste. *International Journal of Chemical Engineering*, 2016.
- Guan, Z., Lv, J., Bai, P., & Guo, X. (2016). Boron removal from aqueous solutions by adsorption—A review. *Desalination*, 383, 29-37.
- Güler, C., Kurt, M. A., Alpaslan, M., & Akbulut, C. (2012). Assessment of the impact of anthropogenic activities on the groundwater hydrology and chemistry in Tarsus coastal plain (Mersin, SE Turkey) using fuzzy clustering, multivariate statistics and GIS techniques. *Journal of Hydrology*, 414, 435-451.
- Guo, Y., Zhang, Y., Zheng, D., Li, M., & Yue, J. (2020). Isolation and characterization of nanocellulose crystals via acid hydrolysis from agricultural waste-tea stalk. *International Journal of Biological Macromolecules*, 163, 927-933.
- Gurreri, L., Tamburini, A., Cipollina, A., & Micale, G. (2020). Electrodialysis applications in wastewater treatment for environmental protection and resources recovery: A systematic review on progress and perspectives. *Membranes*, 10(7), 146.
- Haafiz, M. M., Eichhorn, S. J., Hassan, A., & Jawaid, M. (2013). Isolation and characterization of microcrystalline cellulose from oil palm biomass residue. *Carbohydrate polymers*, 93(2), 628-634.
- Hamad, W. Y., & Hu, T. Q. (2010). Structure–process–yield interrelations in nanocrystalline cellulose extraction. *The Canadian Journal of Chemical Engineering*, 88(3), 392-402.
- Hassan, S. S., Al-Ghouti, M. A., Abu-Dieyeh, M., & McKay, G. (2020). Novel bioadsorbents

- based on date pits for organophosphorus pesticide remediation from water. *Journal of Environmental Chemical Engineering*, 8(1), 103593.
- Hawari, A., Khraisheh, M., & Al-Ghouti, M. A. (2014). Characteristics of olive mill solid residue and its application in remediation of Pb²⁺, Cu²⁺ and Ni²⁺ from aqueous solution: Mechanistic study. *Chemical Engineering Journal*, 251, 329-336.
- He, X., Male, K. B., Nesterenko, P. N., Brabazon, D., Paull, B., & Luong, J. H. (2013). Adsorption and desorption of methylene blue on porous carbon monoliths and nanocrystalline cellulose. *ACS Applied Materials & Interfaces*, 5(17), 8796-8804.
- He, Z. L., Yang, X. E., & Stoffella, P. J. (2005). Trace elements in agroecosystems and impacts on the environment. *Journal of Trace elements in Medicine and Biology*, 19(2-3), 125-140.
- Heibati, B., Rodriguez-Couto, S., Al-Ghouti, M. A., Asif, M., Tyagi, I., Agarwal, S., & Gupta, V. K. (2015). Kinetics and thermodynamics of enhanced adsorption of the dye AR 18 using activated carbons prepared from walnut and poplar woods. *Journal of Molecular Liquids*, 208, 99-105.
- Heibati, B., Rodriguez-Couto, S., Amrane, A., Rafatullah, M., Hawari, A., & Al-Ghouti, M. A. (2014). Uptake of Reactive Black 5 by pumice and walnut activated carbon: chemistry and adsorption mechanisms. *Journal of Industrial and Engineering Chemistry*, 20(5), 2939-2947.
- Helbich, M., Leitner, M., & Kapusta, N. D. (2012). Geospatial examination of lithium in drinking water and suicide mortality. *International journal of health geographics*, 11(1), 19-23.
- Helbich, M., Leitner, M., & Kapusta, N. D. (2015). Lithium in drinking water and suicide mortality: interplay with lithium prescriptions. *The British Journal of Psychiatry*, 207(1), 64-71.

- Herrera, M.A., Mathew, A.P., Oksman, K. (2012). Comparison of cellulose nanowhiskers extracted from industrial bio-residue and commercial microcrystalline cellulose. *Materials Letters*, 71, 28–31
- Hilal, N. M., Ahmed, I. A., & El-Sayed, R. E. (2012). Activated and Nonactivated Date Pits Adsorbents for the Removal of Copper (II) and Cadmium (II) from Aqueous Solutions. *ISRN Physical Chemistry*, 2012.
- Holbrey, J. D., Reichert, W. M., Reddy, R. G., & Rogers, R. D. (2003). Ionic liquids as green solvents: progress and prospects. In ACS symposium series (Vol. 856, pp. 121-133). American Chemical Society Washington, DC.
- Hu, L., Zheng, G., Yao, J., Liu, N., Weil, B., Eskilsson, M., ... & McGehee, M. D. (2013). Transparent and conductive paper from nanocellulose fibers. *Energy & Environmental Science*, 6(2), 513-518.
- Hu, Y., Tang, L., Lu, Q., Wang, S., Chen, X., & Huang, B. (2014). Preparation of cellulose nanocrystals and carboxylated cellulose nanocrystals from borer powder of bamboo. *Cellulose*, 21(3), 1611-1618.
- Hussein, H., & Lambert, L. A. (2020). A Rentier State under Blockade: Qatar's Water-Energy-Food Predicament from Energy Abundance and Food Insecurity to a Silent Water Crisis. *Water*, 12(4), 1051.
- Igwe, J., & Abia, A. (2007). Adsorption isotherm studies of Cd (II), Pb (II) and Zn (II) ions bioremediation from aqueous solution using unmodified and EDTA-modified maize cob. *Eclética Química*, 32(1), 33-42. <http://dx.doi.org/10.1590/s0100-46702007000100005>
- Igwegbe, W.E., Okoro, B.C., Osuagwu, J.C. (2015) Use of Carica papaya as a biosorbents for removal of heavy metals in wastewater, *Int. J. Environ. Ecol. Eng.* 9, 1410–1414.
- Imran Din, M., Mirza, M. L., Ata, S., Athar, M., & Mohsin, I. U. (2013). Thermodynamics of

- biosorption for removal of Co (II) ions by an efficient and ecofriendly biosorbent (*Saccharum bengalense*): kinetics and isotherm modeling. *Journal of Chemistry*, 2013.
- Isik, M., Sardon, H., & Mecerreyes, D. (2014). Ionic liquids and cellulose: dissolution, chemical modification and preparation of new cellulosic materials. *International journal of molecular sciences*, 15(7), 11922-11940.
- Ismail, H. (2015). Food and Water Security in Qatar: Part 2–Water Resources. *Future Directions International Pty Ltd, Dalkeith WA, Australia*.
- Isogai, A., Saito, T., & Fukuzumi, H. (2011). TEMPO-oxidized cellulose nanofibers. *nanoscale*, 3(1), 71-85.
- Jafari, H., Shahrousvand, M., & Kaffashi, B. (2020). Preparation and characterization of reinforced poly (ϵ -caprolactone) nanocomposites by cellulose nanowhiskers. *Polymer Composites*, 41(2), 624-632.
- Jarup, L. (2003). Hazards of heavy metal contamination. *British Medical Bulletin*, 68(1), 167-182. <http://dx.doi.org/10.1093/bmb/ldg032>
- Jawaid, M., & Mohammad, F. (Eds.). (2017). *Nanocellulose and Nanohydrogel Matrices: Biotechnological and Biomedical Applications*. John Wiley & Sons.
- Jeirani, Z., Niu, C. H., & Soltan, J. (2017). Adsorption of emerging pollutants on activated carbon. *Reviews in Chemical Engineering*, 33(5), 491-522.
- Jiang, N., Shang, R., Heijman, S. G., & Rietveld, L. C. (2020). Adsorption of triclosan, trichlorophenol and phenol by high-silica zeolites: Adsorption efficiencies and mechanisms. *Separation and Purification Technology*, 235, 116152.
- Johar, N., Ahmad, I., Dufresne, A. (2012). Extraction, preparation and characterization of cellulose fibres and nanocrystals from rice husk. *Industrial Crops and Products*, 37, 93–99
- Jonoobi, M., Oladi, R., Davoudpour, Y. et al. (2015). Different preparation methods and

- properties of nanostructured cellulose from various natural resources and residues: a review. *Cellulose*, 22, 935–969.
- Joshi, M. D., Chalumot, G., Kim, Y. W., & Anderson, J. L. (2012). Synthesis of glucaminiu m-based ionic liquids and their application in the removal of boron from water. *Chemical Communications*, 48(10), 1410-1412.
- Jung, S. J., Kim, S. H., & Chung, I. M. (2015). Comparison of lignin, cellulose, and hemicellulose contents for biofuels utilization among 4 types of lignocellulosic crops. *Biomass and bioenergy*, 83, 322-327.
- Kabay, N., Güler, E., & Bryjak, M. (2010). Boron in seawater and methods for its separation— a review. *Desalination*, 261(3), 212-217.
- Kambli, N. D., Mageshwaran, V., Patil, P. G., Saxena, S., & Deshmukh, R. R. (2017). Synthesis and characterization of microcrystalline cellulose powder from corn husk fibres using bio-chemical route. *Cellulose*, 24(12), 5355-5369.
- Kandasamy, J., Vigneswaran, S., Hoang, T., & Chaudhary, D. (2006). Adsorption and Biological Filtration in Wastewater Treatment. In *Encyclopedia of Life Support Systems*. Sydney.
- Kapusta, N. D., Mossaheb, N., Etzersdorfer, E., Hlavin, G., Thau, K., Willeit, M., ... & Leithner-Dziubas, K. (2011). Lithium in drinking water and suicide mortality. *The British Journal of Psychiatry*, 198(5), 346-350.
- Khalil, H. A., Tye, Y. Y., Leh, C. P., Saurabh, C. K., Ariffin, F., Fizree, H. M., ... & Suriani, A. B. (2018). Cellulose reinforced biodegradable polymer composite film for packaging applications. In *Bionanocomposites for packaging applications* (pp. 49-69). Springer, Cham.
- Khan, M. N., Rehman, N., Sharif, A., Ahmed, E., Farooqi, Z. H., & Din, M. I. (2020). Environmentally benign extraction of cellulose from dunchi fiber for nanocellulose

- fabrication. *International Journal of Biological Macromolecules*.
- Khan, M., & Lo, I. M. (2016). A holistic review of hydrogel applications in the adsorptive removal of aqueous pollutants: recent progress, challenges, and perspectives. *Water research*, *106*, 259-271.
- Khattab, T. A., Fouda, M. M., Rehan, M., Okla, M. K., Alamri, S. A., Alaraidh, I. A., ... & Allam, A. A. (2020). Novel halochromic cellulose nanowhiskers from rice straw: Visual detection of urea. *Carbohydrate Polymers*, *231*, 115740.
- Kian, L. K., Jawaid, M., Ariffin, H., & Karim, Z. (2018). Isolation and characterization of nanocrystalline cellulose from roselle-derived microcrystalline cellulose. *International journal of biological macromolecules*, *114*, 54-63.
- Kian, L. K., Saba, N., Jawaid, M., & Sultan, M. T. H. (2019). A review on processing techniques of bast fibers nanocellulose and its polylactic acid (PLA) nanocomposites. *International journal of biological macromolecules*, *121*, 1314-1328.
- Kim, T., Kim, T. K., & Zoh, K. D. (2020). Removal mechanism of heavy metal (Cu, Ni, Zn, and Cr) in the presence of cyanide during electrocoagulation using Fe and Al electrodes. *Journal of Water Process Engineering*, *33*, 101109.
- Kontturi, E., Laaksonen, P., Linder, M. B., Gröschel, A. H., Rojas, O. J., & Ikkala, O. (2018). Advanced materials through assembly of nanocelluloses. *Advanced Materials*, *30*(24), 1703779.
- Kopp, J. F., & Kroner, R. C. (1969). *Trace metals in waters of the United States: A five-year summary of trace metals in rivers and lakes of the United States (October 1, 1962-September 30, 1967)*. Federal Water Pollution Control Administration, Division of Pollution Surveillance.
- Köse, T. E., Demiral, H., & Öztürk, N. (2011). Adsorption of boron from aqueous solutions using activated carbon prepared from olive bagasse. *Desalination and Water*

Treatment, 29(1-3), 110-118.

- Kubovský, I., Kačíková, D., & Kačík, F. (2020). Structural changes of oak wood main components caused by thermal modification. *Polymers*, 12(2), 485.
- Kuiper, N., Rowell, C., & Shomar, B. (2015). High levels of molybdenum in Qatar's groundwater and potential impacts. *Journal of Geochemical Exploration*, 150, 16-24.
- Kuiper, N., Rowell, C., Nriagu, J., & Shomar, B. (2014). What do the trace metal contents of urine and toenail samples from Qatar' s farm workers bioindicate?. *Environmental research*, 131, 86-94.
- Kyzas, G. Z., & Kostoglou, M. (2014). Green adsorbents for wastewaters: a critical review. *Materials*, 7(1), 333-364.
- Lamaming, J., Hashim, R., Sulaiman, O., Leh, C., Sugimoto, T., & Nordin, N. (2015). Cellulose nanocrystals isolated from oil palm trunk. *Carbohydrate Polymers*, 127, 202-208.
- Lani, N., Ngadi, N., Johari, A., and Jusoh, M. (2014) Isolation, Characterization, and Application of Nanocellulose from Oil Palm Empty Fruit Bunch Fiber as Nanocomposites. *J. Nanomater.*, 1-9.
- Leybourne, M. I., & Cameron, E. M. (2008). Source, transport, and fate of rhenium, selenium, molybdenum, arsenic, and copper in groundwater associated with porphyry–Cu deposits, Atacama Desert, Chile. *Chemical Geology*, 247(1-2), 208-228.
- Li, J., Wei, X., Wang, Q., Chen, J., Chang, G., Kong, L., ... & Liu, Y. (2012). Homogeneous isolation of nanocellulose from sugarcane bagasse by high pressure homogenization. *Carbohydrate polymers*, 90(4), 1609-1613.
- Li, X., Liu, R., Wu, S., Liu, J., Cai, S., & Chen, D. (2011). Efficient removal of boron acid by N-methyl-D-glucamine functionalized silica–polyallylamine composites and its adsorption mechanism. *Journal of colloid and interface science*, 361(1), 232-237.

- Li, Y., Xiao, H., Pan, Y., & Wang, L. (2018). Novel composite adsorbent consisting of dissolved cellulose fiber/microfibrillated cellulose for dye removal from aqueous solution. *ACS Sustainable Chemistry & Engineering*, *6*(5), 6994-7002.
- Li, Z., & Taubert, A. (2009). Cellulose/gold nanocrystal hybrids via an ionic liquid/aqueous precipitation route. *Molecules*, *14*(11), 4682-4688.
- Liang, S., Cao, S., Liu, C., Zeb, S., Cui, Y., & Sun, G. (2020). Heavy metal adsorption using structurally preorganized adsorbent. *RSC Advances*, *10*(12), 7259-7264.
- Liang, Y., Kang, W., Zhong, C., Deng, N., & Cheng, B. (2021). Multifunctional LaF₃ doped pomegranate-like porous carbon nanofibers with high-speed transfer channel and strong polar interface for high stability lithium sulfur battery. *Chemical Engineering Journal*, *403*, 126449.
- Lin, T. L., & Lien, H. L. (2013). Effective and selective recovery of precious metals by thiourea modified magnetic nanoparticles. *International journal of molecular sciences*, *14*(5), 9834-9847.
- Lindsey, B. D., Belitz, K., Cravotta III, C. A., Toccalino, P. L., & Dubrovsky, N. M. (2021). Lithium in groundwater used for drinking-water supply in the United States. *Science of The Total Environment*, *767*, 144691.
- Liu, F., Zheng, J., Huang, C. H., Tang, C. H., & Ou, S. Y. (2018). Pickering high internal phase emulsions stabilized by protein-covered cellulose nanocrystals. *Food Hydrocolloids*, *82*, 96-105.
- Liu, L., Zhang, H., Zhang, Y., Cao, D., & Zhao, X. (2015). Lithium extraction from seawater by manganese oxide ion sieve MnO₂·0.5 H₂O. *Colloids and Surfaces A: Physicochemical and Engineering Aspects*, *468*, 280-284.
- Loucks, D. P., & van Beek, E. (2017). Water resources planning and management: An overview. In *Water Resource Systems Planning and Management* (pp. 1-49). Springer,

Cham.

- Lu, H., Gui, Y., Zheng, L., & Liu, X. (2013). Morphological, crystalline, thermal and physicochemical properties of cellulose nanocrystals obtained from sweet potato residue. *Food Research International*, 50(1), 121-128.
- Lu, Y., Lu, Y. C., Hu, H. Q., Xie, F. J., Wei, X. Y., & Fan, X. (2017). Structural characterization of lignin and its degradation products with spectroscopic methods. *Journal of spectroscopy*, 2017.
- Lu, Z., Fan, L., Zheng, H., Lu, Q., Liao, Y., and Huang, B. (2013) Preparation, characterization and optimization of nanocellulose whiskers by simultaneously ultrasonic wave and microwave assisted. *Bioresource Technology*, 146, 82–88.
- Luzi, F., Fortunati, E., Jiménez, A., Puglia, D., Chiralt, A., & Torre, L. (2017). PLA nanocomposites reinforced with cellulose nanocrystals from *Posidonia oceanica* and ZnO nanoparticles for packaging application. *Journal of Renewable Materials*, 5(2), 103-115.
- Lyne, B. (2013). Market prospects for nanocellulose. *The Royal Institute of Technology, Alberta Biomaterials Development Centre, Edmonton, AB, Canada*.
- Magdy, Y. M., Altaher, H., & ElQada, E. (2018). Removal of three nitrophenols from aqueous solutions by adsorption onto char ash: equilibrium and kinetic modeling. *Applied water science*, 8(1), 1-15.
- Mahdi, Z., Qiming, J. Y., & El Hanandeh, A. (2018). Removal of lead (II) from aqueous solution using date seed-derived biochar: batch and column studies. *Applied Water Science*, 8(6), 1-13.
- Maheswari, C.U., Reddy, K.O., Muzenda, E., Guduri, B.R., Rajulu, A. V. (2012) Extraction and characterization of cellulose microfibrils from agricultural residue – *Cocos nucifera* L. *Biomass Bioenerg.*, 46, 555.

- Mahfoudhi, N., & Boufi, S. (2017). Nanocellulose as a novel nanostructured adsorbent for environmental remediation: a review. *Cellulose*, *24*(3), 1171-1197.
- Mallick, J., Singh, C. K., AlMesfer, M. K., Kumar, A., Khan, R. A., Islam, S., & Rahman, A. (2018). Hydro-geochemical assessment of groundwater quality in Aseer Region, Saudi Arabia. *Water*, *10*(12), 1847.
- Mandal, A., & Chakrabarty, D. (2011). Isolation of nanocellulose from waste sugarcane bagasse (SCB) and its characterization. *Carbohydrate Polymers*, *86*(3), 1291-1299.
- Manirethan, V., Gupta, N., Balakrishnan, R. M., & Raval, K. (2019). Batch and continuous studies on the removal of heavy metals from aqueous solution using biosynthesised melanin-coated PVDF membranes. *Environmental Science and Pollution Research*, 1-15.
- Marett J., Aning A., Foster E.J. (2017) The isolation of cellulose nanocrystals from pistachio shells via acid hydrolysis, *Ind. Crop. Prod.* *109*, 869–874.
- Mathew, B. T., Raji, S., Dagher, S., Hilal-Alnaqbi, A., Mourad, A. H. I., Al-Zuhair, S., ... & Amin, A. (2018). Bilirubin detoxification using different phytomaterials: characterization and in vitro studies. *International journal of nanomedicine*, *13*, 2997.
- Medina, L., Nishiyama, Y., Daicho, K., Saito, T., Yan, M., & Berglund, L. A. (2019). Nanostructure and Properties of Nacre-Inspired Clay/Cellulose Nanocomposites—Synchrotron X-ray Scattering Analysis. *Macromolecules*, *52*(8), 3131-3140.
- Merkel, B. J., Planer-Friedrich, B., & Nordstrom, D. K. (2005). Groundwater geochemistry. *A practical guide to modeling of natural and contaminated aquatic systems*, *2*.
- Miessler, G. L., Fischer, P. J., & Tarr, D. A. (2014). *Inorganic chemistry*.
- Minceva, M., Fajgar, R., Markovska, L., & Meshko, V. (2008). Comparative Study of Zn²⁺, Cd²⁺, and Pb²⁺ Removal From Water Solution Using Natural Clinoptilolitic Zeolite and Commercial Granulated Activated Carbon. Equilibrium of Adsorption. Separation

- Science and Technology, 43(8), 2117-2143. doi:10.1080/01496390801941174
- Ministry of Development Planning and Statistics (2015) Water statistics in the state of Qatar.
- Mohammed, N., Grishkewich, N., Waeijen, H. A., Berry, R. M., & Tam, K. C. (2016). Continuous flow adsorption of methylene blue by cellulose nanocrystal-alginate hydrogel beads in fixed bed columns. *Carbohydrate polymers*, 136, 1194-1202.
- Moore, J. A., & Expert Scientific Committee. (1997). An assessment of boric acid and borax using the IEHR evaluative process for assessing human developmental and reproductive toxicity of agents. *Reproductive Toxicology*, 11(1), 123-160.
- Morais, J.P., Rosa, M.D.F., Moreira de Souza, M.D.S., Nascimento, L.D., Nascimento, D.M., and Cassales, A.R. (2013) Extraction and characterization of nanocellulose structures from raw cotton linter. *Carbohydrate Polymers*, 91, 229–235.
- Morán, J. I., Alvarez, V. A., Cyras, V. P., & Vázquez, A. (2008). Extraction of cellulose and preparation of nanocellulose from sisal fibers. *Cellulose*, 15(1), 149-159.
- Mueller, S., Weder, C., & Foster, E. J. (2014). Isolation of cellulose nanocrystals from pseudostems of banana plants. *RSC advances*, 4(2), 907-915.
- Mullen, K. (2021). Information on Earth's water. Retrieved from <https://www.ngwa.org/what-is-groundwater/About-groundwater/information-on-earth's-water#:~:text=Ninety%2Deight%20percent%20of%20Earth's,and%20weathered%20areas%20of%20bedrock>.
- Murodjon, S., Yu, X., Li, M., Duo, J., & Deng, T. (2020). Lithium Recovery from Brines Including Seawater, Salt Lake Brine, Underground Water and Geothermal Water. In *Thermodynamics and Energy Engineering*. IntechOpen
- Naeimi, S., & Faghihian, H. (2017). Performance of novel adsorbent prepared by magnetic metal-organic framework (MOF) modified by potassium nickel hexacyanoferrate for removal of Cs⁺ from aqueous solution. *Separation and Purification Technology*, 175,

255-265.

- Nagul, E. A., McKelvie, I. D., Worsfold, P., & Kolev, S. D. (2015). The molybdenum blue reaction for the determination of orthophosphate revisited: opening the black box. *Analytica chimica acta*, *890*, 60-82.
- Ogungbenro, A.E., Quang, D.V., Al-Ali, K.A., Vega, L.F., Abu-Zahra, M.R.M. (2018) Physical synthesis and characterization of activated carbon from date seeds for CO₂ capture. *Journal of Environmental Chemical Engineering* *6*; 4245–4252.
- Oliveira, J. P., Bruni, G. P., Halal, S. L. M., Zavareze, E. R. (2019) Cellulose nanocrystals from rice and oat husks and their application in aerogels for food packaging. *International Journal of Biological Macromolecules* *124*, 175–184.
- Ouyang, D., Zhuo, Y., Hu, L., Zeng, Q., Hu, Y., & He, Z. (2019). Research on the adsorption behavior of heavy metal ions by porous material prepared with silicate tailings. *Minerals*, *9*(5), 291.
- Palomar, J., Lemus, J., Gilarranz, M. A., & Rodriguez, J. J. (2009). Adsorption of ionic liquids from aqueous effluents by activated carbon. *Carbon*, *47*(7), 1846-1856.
- Park, H., Singhal, N., & Jho, E. H. (2015). Lithium sorption properties of HMnO in seawater and wastewater. *Water research*, *87*, 320-327.
- Peng, H., & Guo, J. (2020). Removal of chromium from wastewater by membrane filtration, chemical precipitation, ion exchange, adsorption electrocoagulation, electrochemical reduction, electrodialysis, electrodeionization, photocatalysis and nanotechnology: a review. *Environmental Chemistry Letters*, 1-14.
- Pennisi, M., Bianchini, G., Muti, A., Kloppmann, W., & Gonfiantini, R. (2006). Behaviour of boron and strontium isotopes in groundwater–aquifer interactions in the Cornia Plain (Tuscany, Italy). *Applied Geochemistry*, *21*(7), 1169-1183.
- Peretz, R., Sterenzon, E., Gerchman, Y., Vadivel, V. K., Luxbacher, T., & Mamane, H. (2019).

- Nanocellulose production from recycled paper mill sludge using ozonation pretreatment followed by recyclable maleic acid hydrolysis. *Carbohydrate polymers*, 216, 343-351.
- Phanthong, P., Reubroycharoen, P., Hao, X., Xu, G., Abudula, A., & Guan, G. (2018). Nanocellulose: Extraction and application. *Carbon Resources Conversion*, 1(1), 32-43.
- Pillai, P., Dharaskar, S., Sasikumar, S., & Khalid, M. (2019). Zeolitic imidazolate framework-8 nanoparticle: a promising adsorbent for effective fluoride removal from aqueous solution. *Applied Water Science*, 9(7), 1-12.
- Pillai, P., Dharaskar, S., Sinha, M. K., Sillanpää, M., & Khalid, M. (2020). Iron oxide nanoparticles modified with ionic liquid as an efficient adsorbent for fluoride removal from groundwater. *Environmental Technology & Innovation*, 19, 100842.
- POURSABERI, T. (2014). APPLICATION OF MAGNETIC GRAPHENE-BASED NANOCOMPOSITE FUNCTIONALIZED WITH IONIC LIQUID FOR THE SULFUR REMOVAL FROM GASOLINE.
- Pyrzynska K. (2019) Removal of cadmium from wastewaters with low-cost adsorbents. *Journal of Environmental Chemical Engineering* 7, 102795
- Quijada-Maldonado, E., Sánchez, F., Pérez, B., Tapia, R., & Romero, J. (2018). Task-specific ionic liquids as extractants for the solvent extraction of molybdenum (VI) from aqueous solution using different commercial ionic liquids as diluents. *Industrial & Engineering Chemistry Research*, 57(5), 1621-1629.
- Quijada-Maldonado, E., Torres, M. J., & Romero, J. (2017). Solvent extraction of molybdenum (VI) from aqueous solution using ionic liquids as diluents. *Separation and Purification Technology*, 177, 200-206.
- Raiguel, S., Dehaen, W., & Binnemans, K. (2019). Isolation of molybdenum (vi) from simulated leachates of irradiated uranium-aluminum targets using diluted and undiluted

- sulfate ionic liquids. *Green Chemistry*, 21(14), 3948-3960.
- Rajinipriya, M., Nagalakshmaiah, M., Robert, M., & Elkoun, S. (2018). Importance of agricultural and industrial waste in the field of nanocellulose and recent industrial developments of wood based nanocellulose: a review. *ACS Sustainable Chemistry & Engineering*, 6(3), 2807-2828.
- Rajmohan, N., Niazi, B. A., & Masoud, M. H. (2019). Evaluation of a brackish groundwater resource in the Wadi Al-Lusub basin, Western Saudi Arabia. *Environmental Earth Sciences*, 78(15), 1-17.
- Ravenscroft, P., & McArthur, J. M. (2004). Mechanism of regional enrichment of groundwater by boron: the examples of Bangladesh and Michigan, USA. *Applied Geochemistry*, 19(9), 1413-1430.
- Razi, M. A. M., Hishammudin, M. N. A. M., & Hamdan, R. (2017). Factor affecting textile dye removal using adsorbent from activated carbon: A review. In *MATEC Web of Conferences* (Vol. 103, p. 06015). EDP Sciences.
- Reedijk, J., & Poepelmeier, K. (2013). Comprehensive inorganic chemistry II: from elements to applications V2 *Transition Elem., Lanthanides and Actinides* (pp. 187-221). Elsevier Ltd..
- Repo, E., Warchoń, J. K., Bhatnagar, A., & Sillanpää, M. (2011). Heavy metals adsorption by novel EDTA-modified chitosan–silica hybrid materials. *Journal of colloid and interface science*, 358(1), 261-267.
- Ribeiro, R. S. A., Bojorge, N., & Pereira Jr, N. (2020). Statistical analysis of the crystallinity index of nanocellulose produced from Kraft pulp via controlled enzymatic hydrolysis. *Biotechnology and Applied Biochemistry*.
- Ribeiro, R. S., Pohlmann, B. C., Calado, V., Bojorge, N., & Pereira Jr, N. (2019). Production of nanocellulose by enzymatic hydrolysis: Trends and challenges. *Engineering in Life*

Sciences, 19(4), 279-291.

Ritchie, H., & Roser, M. (2020). Water Use and Stress. Retrieved from <https://ourworldindata.org/water-use-stress>

Rogers, R. D., & Seddon, K. R. (2003). Ionic liquids--solvents of the future?. *Science*, 302(5646), 792-793.

Rowland, H. A., Omoregie, E. O., Millot, R., Jimenez, C., Mertens, J., Baciuc, C., ... & Berg, M. (2011). Geochemistry and arsenic behaviour in groundwater resources of the Pannonian Basin (Hungary and Romania). *Applied Geochemistry*, 26(1), 1-17.

Sacui, I. A., Nieuwendaal, R. C., Burnett, D. J., Stranick, S. J., Jorfi, M., Weder, C., ... & Gilman, J. W. (2014). Comparison of the properties of cellulose nanocrystals and cellulose nanofibrils isolated from bacteria, tunicate, and wood processed using acid, enzymatic, mechanical, and oxidative methods. *ACS applied materials & interfaces*, 6(9), 6127-6138.

Saleem, J., Shahid, U. B., Hijab, M., Mackey, H., & McKay, G. (2019). Production and applications of activated carbons as adsorbents from olive stones. *Biomass Conversion and Biorefinery*, 9(4), 775-802.

Samra, S. E., Jeragh, B., EL-Nokrashy, A. M., & El-Asmy, A. A. (2014). Biosorption of Pb²⁺ from natural water using date pits: a green chemistry approach. *Modern Chemistry & Applications*.

Sankar, K. S., Bhargava, J. S., & Karmakar, S. (2017). Boron content in shallow ground water of Andhra Pradesh and Telangana states, India. *IOSR J. Environ. Sci. Toxicol. Food Technol*, 11, 56-60.

Sarsenov, A., Bishimbaev, V. K., Kapsalamov, B. A., Lepesov, K. K., Gapparova, K. M., & Grzesiak, P. (2018). Chemical modification of cellulose for boron sorption from water solutions. *Polish Journal of Chemical Technology*, 20(4), 123-128.

- Seyedmohammadi, J., Esmaeelnejad, L., & Shabanpour, M. (2016). Spatial variation modelling of groundwater electrical conductivity using geostatistics and GIS. *Modeling earth systems and environment*, 2(4), 1-10.
- Shafiq, M., Alazba A., A., & Amin, M.t., (2018). Removal of Heavy Metals from Wastewater using Date Palm as a Biosorbent: A Comparative Review. *Sains Malaysiana*, 47(1), 35-49. doi:10.17576/jsm-2018-4701-05
- Shafizah, S., Izwan, A. S., Fatirah, F., & Hasraf, M. N. (2018, October). Review on cellulose nanocrystals (CNCs) as reinforced agent on electrospun nanofibers: mechanical and thermal properties. In *IOP Conference Series: Materials Science and Engineering*. IOP Publishing (p. 012011).
- Shanmugarajah, B., Kiew, P. L., Chew, I. M. L., Choong, T. S. Y., & Tan, K. W. (2015). Isolation of nanocrystalline cellulose (NCC) from palm oil empty fruit bunch (EFB): Preliminary result on FTIR and DLS analysis. *Chemical Engineering Transactions*, 45, 1705-1710.
- Shannon, R. D. (1976). Revised effective ionic radii and systematic studies of interatomic distances in halides and chalcogenides. *Acta crystallographica section A: crystal physics, diffraction, theoretical and general crystallography*, 32(5), 751-767.
- Sharma, P., Kaur, H., Sharma, M., & Sahore, V. (2011). A review on applicability of naturally available adsorbents for the removal of hazardous dyes from aqueous waste. *Environmental monitoring and assessment*, 183(1-4), 151-195
- Sheltami, R. M., Abdullah, I., Ahmad, I., Dufresne, A., & Kargarzadeh, H. (2012). Extraction of cellulose nanocrystals from mengkuang leaves (*Pandanus tectorius*). *Carbohydrate Polymers*, 88(2), 772-779.
- Shi T., Ma J., Wu X., Wu F. (2018) Inventories of heavy metal inputs and outputs to and from agricultural soils: A review *Ecotoxicology and Environmental Safety* 164, 118–124.

- Shomar, B. (2015). Geochemistry of soil and groundwater in arid regions: Qatar as a case study. *Groundwater for Sustainable Development*, 1(1-2), 33-40.
- Shomar, B., & Hawari, J. (2017). Desalinated drinking water in the GCC countries—The need to address consumer perceptions. *Environmental research*, 158, 203-211.
- Silva, L. E., dos Santos, A. D. A., Torres, L., McCaffrey, Z., Klamczynski, A., Glenn, G., ... & Damásio, R. A. P. (2020). REDISPERSION AND STRUCTURAL CHANGE EVALUATION OF DRIED MICROFIBRILLATED CELLULOSE. *Carbohydrate Polymers*, 117165.
- Singh, K., Lataye, D. H., Wasewar, K. L., & Yoo, C. K. (2013). Removal of fluoride from aqueous solution: status and techniques. *Desalination and Water Treatment*, 51(16-18), 3233-3247.
- Smedley, P. L., Cooper, D. M., Ander, E. L., Milne, C. J., & Lapworth, D. J. (2014). Occurrence of molybdenum in British surface water and groundwater: Distributions, controls and implications for water supply. *Applied Geochemistry*, 40, 144-154.
- Soliman, N., & Moustafa, A. (2020). Industrial solid waste for heavy metals adsorption features and challenges; a review. *Journal Of Materials Research And Technology*, 9(5), 10235-10253. doi: 10.1016/j.jmrt.2020.07.045.
- Song, K., Zhu, X., Zhu, W., & Li, X. (2019). Preparation and characterization of cellulose nanocrystal extracted from *Calotropis procera* biomass. *Bioresources And Bioprocessing*, 6(1).
- Song, Q., Winter, W. T., Bujanovic, B. M., & Amidon, T. E. (2014). Nanofibrillated cellulose (NFC): A high-value co-product that improves the economics of cellulosic ethanol production. *Energies*, 7(2), 607-618.
- Sorlini, S., Rondi, L., Pollmann Gomez, A., & Collivignarelli, C. (2015). APPROPRIATE TECHNOLOGIES FOR DRINKING WATER TREATMENT IN

MEDITERRANEAN COUNTRIES. *Environmental Engineering & Management Journal (EEMJ)*, 14(7).

Soud, F., Agoubi, B., Telahigue, F., Chahlaoui, A., & Kharroubi, A. (2018). Groundwater salinization and seawater intrusion tracing based on Lithium concentration in the shallow aquifer of Jerba Island, southeastern Tunisia. *Journal of African Earth Sciences*, 138, 233-246.

Srivastava, S., Agrawal, S. B., & Mondal, M. K. (2016). Characterization, isotherm and kinetic study of Phaseolus vulgaris husk as an innovative adsorbent for Cr (VI) removal. *Korean Journal of Chemical Engineering*, 33(2), 567-575.

Sundqvist-Andberg, H. (2013). *Research highlights in industrial biomaterials 2009-2012*. VTT Technical Research Centre of Finland.

Suursoo, S., Hill, L., Raidla, V., Kiisk, M., Jantsikene, A., Nilb, N., ... & Isakar, K. (2017). Temporal changes in radiological and chemical composition of Cambrian-Vendian groundwater in conditions of intensive water consumption. *Science of The Total Environment*, 601, 679-690.

Syafri, E., Kasim, A., Abrial, H., Sulungbudi, G. T., Sanjay, M. R., & Sari, N. H. (2018). Synthesis and characterization of cellulose nanofibers (CNF) ramie reinforced cassava starch hybrid composites. *International journal of biological macromolecules*, 120, 578-586.

Tang, Y., Shen, X., Zhang, J., Guo, D., Kong, F., & Zhang, N. (2015). Extraction of cellulose nano-crystals from old corrugated container fiber using phosphoric acid and enzymatic hydrolysis followed by sonication. *Carbohydrate Polymers*, 125, 360-366.

Tao, J., Yang, J., Ma, C., Li, J., Du, K., Wei, Z., ... & Deng, X. (2020). Cellulose nanocrystals/graphene oxide composite for the adsorption and removal of levofloxacin hydrochloride antibiotic from aqueous solution. *Royal Society Open Science*, 7(10),

200857.

- Tarchoun, A. F., Trache, D., Klapötke, T. M., Derradji, M., & Bessa, W. (2019). Ecofriendly isolation and characterization of microcrystalline cellulose from giant reed using various acidic media. *Cellulose*, *26*(13), 7635-7651.
- Tesoriero, A. J., Spruill, T. B., & Eimers, J. L. (2004). Geochemistry of shallow ground water in coastal plain environments in the southeastern United States: implications for aquifer susceptibility. *Applied Geochemistry*, *19*(9), 1471-1482.
- Trache, D., Hussin, M. H., Chuin, C. T. H., Sabar, S., Fazita, M. N., Taiwo, O. F., ... & Haafiz, M. M. (2016). Microcrystalline cellulose: Isolation, characterization and bio-composites application—A review. *International Journal of Biological Macromolecules*, *93*, 789-804.
- Trache, D., Hussin, M. H., Haafiz, M. M., & Thakur, V. K. (2017). Recent progress in cellulose nanocrystals: sources and production. *Nanoscale*, *9*(5), 1763-1786.
- Turek, M., Dydo, P., Trojanowska, J., & Bandura, B. (2007). Electrodialytic treatment of boron-containing wastewater. *Desalination*, *205*(1-3), 185-191.
- Uddin, M. T., Rahman, M. A., Rukanuzzaman, M., & Islam, M. A. (2017). A potential low cost adsorbent for the removal of cationic dyes from aqueous solutions. *Applied Water Science*, *7*(6), 2831-2842.
- Veldkamp, T. I., Wada, Y., de Moel, H., Kummu, M., Eisner, S., Aerts, J. C., & Ward, P. J. (2015). Changing mechanism of global water scarcity events: Impacts of socioeconomic changes and inter-annual hydro-climatic variability. *Global Environmental Change*, *32*, 18-29.
- Verma, C., Mishra, A., Chauhan, S., Verma, P., Srivastava, V., Quraishi, M. A., & Ebenso, E. E. (2019). Dissolution of cellulose in ionic liquids and their mixed cosolvents: A review. *Sustainable Chemistry and Pharmacy*, *13*, 100162.

- Vijayakumar, G., Tamilarasan, R., & Dharmendirakumar, M. (2012). Adsorption, Kinetic, Equilibrium and Thermodynamic studies on the removal of basic dye Rhodamine-B from aqueous solution by the use of natural adsorbent perlite. *J. Mater. Environ. Sci*, 3(1), 157-170.
- Visanko, M., Liimatainen, H., Sirviö, J. A., Heiskanen, J. P., Niinimäki, J., and Hormi, O. (2014). Amphiphilic cellulose nanocrystals from acid-free oxidative treatment: physicochemical characteristics and use as an oil–water stabilizer. *Biomacromolecules*, 15, 2769–2775.
- Wajima, T., Munakata, K., & Uda, T. (2012). Adsorption behavior of lithium from seawater using manganese oxide adsorbent. *Plasma and Fusion Research*, 7, 24050212405021.
- Wallace, D. R., & Djordjevic, A. B. (2020). Heavy metal and pesticide exposure: A mixture of potential toxicity and carcinogenicity. *Current Opinion in Toxicology*, 19, 72-79.
- Wang, J., Liu, X., Jin, T., He, H., & Liu, L. (2019). Preparation of nanocellulose and its potential in reinforced composites: a review. *Journal of Biomaterials Science, Polymer Edition*, 30(11), 919-946.
- Wang, X., Jing, S., Hou, Z., Liu, Y., Qiu, X., Liu, Y., & Tan, Y. (2018). Permeable, robust and magnetic hydrogel beads: water droplet templating synthesis and utilization for heavy metal ions removal. *Journal of Materials Science*, 53(21), 15009-15024.
- Wen, Q., Wang, Y., Xu, K., Li, N., Zhang, H., Yang, Q., & Zhou, Y. (2016). Magnetic solid-phase extraction of protein by ionic liquid-coated Fe@ graphene oxide. *Talanta*, 160, 481-488.
- WHO, (2017) Guidelines for drinking-water quality: fourth edition incorporating the first addendum. Geneva: World Health Organization; 2017. Licence: CC BY-NC-SA 3.0 IGO. Retrieved from https://www.who.int/water_sanitation_health/publications/drinking-water-quality-

guidelines-4-including-1st-addendum/en/.

- World Health Organization. (2003). *Molybdenum in drinking-water: background document for development of WHO guidelines for drinking-water quality* (No. WHO/SDE/WSH/03.04/11). World Health Organization.
- Wu, J., & Sun, Z. (2016). Evaluation of shallow groundwater contamination and associated human health risk in an alluvial plain impacted by agricultural and industrial activities, mid-west China. *Exposure and Health*, 8(3), 311-329.
- Wulandari, W., Rochliadi, A., and Arcana, I. (2016). Nanocellulose prepared by acid hydrolysis of isolated cellulose from sugarcane bagasse. *IOP Conference Series: Materials Science and Engineering*, 107, 012045.
- Wulfsberg, G. (1987). *Principles of Descriptive Inorganic Chemistry*. Monterey, CA: Brooks/Cole Publishing Company.
- Wulfsberg, G. (1991). *Principles of descriptive inorganic chemistry*. University Science Books.
- Xiao, J., Nie, X., Sun, S., Song, X., Li, P., & Yu, J. (2015). Lithium ion adsorption–desorption properties on spinel $\text{Li}_4\text{Mn}_5\text{O}_{12}$ and pH-dependent ion-exchange model. *Advanced Powder Technology*, 26(2), 589-594.
- Xu, C., Yu, T., Peng, J., Zhao, L., Li, J., & Zhai, M. (2020). Efficient Adsorption Performance of Lithium Ion onto Cellulose Microspheres with Sulfonic Acid Groups. *Quantum Beam Science*, 4(1), 6.
- Yagub, M., Sen, T., Afroze, S., & Ang, H. (2014). Dye and its removal from aqueous solution by adsorption: A review. *Advances In Colloid And Interface Science*, 209, 172-184.
- Yan, X. F., Fan, X. R., Wang, Q., & Shen, Y. (2017). An adsorption isotherm model for adsorption performance of silver-loaded activated carbon. *Thermal Science*, 21(4), 1645-1649.

- Yang, X., & Cranston, E. D. (2014). Chemically cross-linked cellulose nanocrystal aerogels with shape recovery and superabsorbent properties. *Chemistry of Materials*, 26(20), 6016-6025.
- Yang, X., Wang, X., Liu, H., Zhao, Y., Jiang, S., and Liu, L. (2017). Impact of dimethyl sulfoxide treatment on morphology and characteristics of nanofibrillated cellulose isolated from corn husks. *Bioresource Technology*, 12, 95–106.
- Yılmaz, A. E., Boncukcuoglu, R., Yılmaz, M. T., & Kocakerim, M. M. (2005). Adsorption of boron from boron-containing wastewaters by ion exchange in a continuous reactor. *Journal of hazardous materials*, 117(2-3), 221-226.
- Yin, Q., Liu, M., & Ren, H. (2019). Biochar produced from the co-pyrolysis of sewage sludge and walnut shell for ammonium and phosphate adsorption from water. *Journal of environmental management*, 249, 109410.
- Yongvanich, N. (2015) Isolation of nanocellulose from pomelo fruit fibers by chemical treatments. *J. Nat. Fibers*. 12, 323–331.
- Zango, Z. U., Bakar, N. H. H. A., Sambudi, N. S., Jumbri, K., Abdullah, N. A. F., Kadir, E. A., & Saad, B. (2020). Adsorption of chrysene in aqueous solution onto MIL-88 (Fe) and NH₂-MIL-88 (Fe) metal-organic frameworks: Kinetics, isotherms, thermodynamics and docking simulation studies. *Journal of Environmental Chemical Engineering*, 8(2), 103544.
- Zante, G., Boltoeva, M., Masmoudi, A., Barillon, R., Trébouet, D. (2019). Lithium extraction from complex aqueous solutions using supported ionic liquid membranes. *Journal of Membrane Science* 580 (2019) 62– 76.
- Zhang, H., Khanal, S. K., Jia, Y., Song, S., & Lu, H. (2019). Fundamental insights into ciprofloxacin adsorption by sulfate-reducing bacteria sludge: Mechanisms and thermodynamics. *Chemical Engineering Journal*, 378, 122103.

- Zheng, D., Zhang, Y., Guo, Y., & Yue, J. (2019). Isolation and characterization of nanocellulose with a novel shape from walnut (*Juglans Regia* L.) shell agricultural waste. *Polymers*, *11*(7), 1130.
- Zhou, L., Xiong, W., & Liu, S. (2015). Preparation of a gold electrode modified with Au–TiO₂ nanoparticles as an electrochemical sensor for the detection of mercury (II) ions. *Journal of Materials Science*, *50*(2), 769-776.
- Zhuang, J., Li, M., Pu, Y., Ragauskas, A. J., & Yoo, C. G. (2020). Observation of Potential Contaminants in Processed Biomass Using Fourier Transform Infrared Spectroscopy. *Applied Sciences*, *10*(12), 4345.
- Zou, Y., Zhang, C., Wang, P., Zhang, Y., & Zhang, H. (2020). Electrospun chitosan/polycaprolactone nanofibers containing chlorogenic acid-loaded halloysite nanotube for active food packaging. *Carbohydrate Polymers*, *247*, 116711.